基于离子阱系统的量子化学模拟

（申请清华大学理学博士学位论文）

培 养 单 位 ： 交 叉 信 息 研 究 院
学　　　　科 ： 物 理 学
研 究 生 ： 沈 杨 超
指 导 教 师 ： 金 奇 奂 副 教 授

二〇一八年五月

Quantum chemistry simulation with trapped ion device

Dissertation Submitted to

Tsinghua University

in partial fulfillment of the requirement

for the degree of

Doctor of Philosophy

in

Physics

by

Shen Yangchao

Dissertation Supervisor :   Professor Kihwan Kim

May, 2018

关于学位论文使用授权的说明

本人完全了解清华大学有关保留、使用学位论文的规定，即：

清华大学拥有在著作权法规定范围内学位论文的使用权，其中包括：（1）已获学位的研究生必须按学校规定提交学位论文，学校可以采用影印、缩印或其他复制手段保存研究生上交的学位论文；（2）为教学和科研目的，学校可以将公开的学位论文作为资料在图书馆、资料室等场所供校内师生阅读，或在校园网上供校内师生浏览部分内容；（3）根据《中华人民共和国学位条例暂行实施办法》，向国家图书馆报送可以公开的学位论文。

本人保证遵守上述规定。

（保密的论文在解密后应遵守此规定）

作者签名：_____   导师签名：_____

日　　期：_____   日　　期：_____

摘　要

作为未来量子计算机的主要候选系统之一，在过去的几十年里，离子阱系统的潜力被极大的挖掘出来。本论文展示了一个完全受控的单个镱离子系统，实现了具有高保真度的量子态初始化、操控、测量。其中，微波操控离子超精细能级结构、脉冲激光操控离子振动模式以及利用相机扩展量子态测量对接下来搭建多离子系统必不可少。

利用单个囚禁离子中四能级系统的量子操控，实现了解决分子电子结构问题的酉耦合簇（UCC）算法。在经典计算机的辅助下，我们的量子计算机成功模拟出氦合氢离子的基态能量，并使用UCC方法模拟了激发态能量和键解离能。

通过对单个囚禁离子中两种振动模式的量子操控，实现了具有两个玻色子振动模的高斯玻色子采样算法，同时模拟了二氧化硫的分子振动能谱。我们掌握了在单次实验中保持相位相干性的操控，包括多个振动模的位移、压缩以及旋转。此外，我们设计出了两个振动模整体投影测量的试验方法。

我们现阶段所做的量子化学算法在离子阱系统中的应用，将为大规模分子模拟问题打下基础。在经典计算机上难以实现的量子模拟，可以在量子系统中高效的运行，这可能使量子霸权成为现实。

关键词：离子阱系统；量子模拟；量子化学模拟；单离子操控

Abstract

The trapped ion system, as one of the leading candidates for the future quantum computer, has shown its potential power in the past decades. In this thesis, a fully controlled single trapped $^{171}\text{Yb}^+$ ion system is exhibited, where we realize the state initialization, manipulation and detection with high fidelity. We manipulate the hyperfine energy levels with the microwave and the motional modes with a pulsed laser. I extend the quantum state detection with a camera, which is essential for the following multi-ion setup.

With the quantum control of the four-level system in a single trapped ion, I implement the Unitary Coupled Cluster (UCC) algorithm for the molecular electronic structure problem. With the assistance of a classical computer, our quantum computer simulates the ground state energy surface of HeH^+, and the excited-state energy and bond-dissociation is simulated non-perturbatively.

With the quantum control of the two motional modes in a single trapped ion, I implement the Gaussian boson sampling algorithm with two bosonic modes and emulate the molecular vibronic spectroscopy of SO_2. We realize the phase-coherent manipulation of displacement, squeezing, and rotation operations with multiple modes in a single realization. Besides, we demonstrate the collective projection measurements for two-phonon-mode.

Our experimental demonstration of the quantum chemistry algorithm would pave the way to large-scale molecular quantum simulations, which are classically intractable but can be efficiently implemented in a quantum system, and bring the quantum supremacy to reality.

Key words: Trapped ion system; Quantum simulation; Quantum chemistry simulation; Single ion control

目　录

第1章 Introduction

1.1 Quantum computing and Quantum chemistry simulation

The simulating of quantum mechanics was proposed as a hard problem in the early 1980s, and Richard Feynman suggested solving this problem by using a quantum computer[1]. Without using an exponentially large amount of physical resources, the quantum computer can outperform the classical computer for a certain problem of large system size. Later, it was shown that quantum computer could also act as a universal quantum simulator, which is constructed by many well-defined qubits that can be initialized, measured, and perform universal quantum gates[2,3]. Quantum simulator provides a practical application before the realization of full-fledged quantum computers. There has been increasingly greater interest in the quantum simulation during the past decades, and a large number of potential applications in physics, chemistry, and biology were proposed. Above that, many proof-of-principle experiments have been carried out on different platforms[4–6], and recent experimental works pushed the number of qubits over 50[7,8].

People believe in near term, a quantum computer capable of handling more than 100 qubits is expected to be developed, which may show the quantum supremacy. Although the simulation of quantum dynamics of physical systems is in general efficient with a quantum computer, the quantum computer in the near term may not be sufficient to perform the full quantum error correction. Therefore, it is an impending question at this stage to find some meaningful tasks with the current level of quantum computers; quantum chemistry simulation turned out to be one of the focus areas for the practical application without a universal quantum computer.

Quantum chemistry aims to develop theoretical methods for calculating molecular properties and evolutions from quantum mechanics. Over the last century, quantum chemistry has achieved great success in exploring the electronic configurations of atoms and molecules[9]. However, the Hilbert space of quantum systems scales exponentially with the system size, making computational costs unfeasible within current conventional computer architectures. Therefore the quantum computer becomes an alternative approach for quantum chemistry simulation[10,11], with many having been proposed algorithms to implement quantum chemistry problems in quantum computers[12–14]. There are two possible directions for long-term quantum chemistry simulation: (a) simulations of static

molecular energies for larger molecules and (b) simulations of more complicated chemical reactions. These simulation processes can be summarized in three steps: (a) preparing the quantum system into an initial state, (b) evolving the initial state with a controlled Hamiltonian, and (c) measuring the desired properties from the final state.

1.2 Trapped ion Quantum computer

Many quantum systems have been established in the past 30 years, e.g., superconducting qubits, trapped ions, cold atoms, nuclear magnetic resonance, nitrogen-vacancy center and quantum optics. To construct a quantum computer, it is necessary to obey the DiVincenzo's criteria, which states the following conditions for a quantum system[15]:

- A scalable physical system with well-characterized qubits
- The ability to initialize the state of the qubits
- Long relevant decoherence times
- A "universal" set of quantum gates
- A qubit-specific measurement capability

Since the invention of the first ion trap by Wolfgang Paul in 1950s[16], there has been a rapid development in the theory and technology of trapped ion system. Until now, the trapped ion system satisfies all the aforementioned DiVincenzo's characteristics other than the scalability, where the long storage time of a large ion crystal is hard to achieve. The qubits in a trapped ion system are defined by the energy levels of the ion, which guarantees the identity between qubits. We control the qubits via lasers or microwave, where the qubits initialization can be achieved with high fidelity. The ions are well isolated from the external environment due to the ultra-high vacuum, and we can reach a relatively long coherence time compared to the gate time. The single qubit gate and two-qubit gate have been demonstrated in the trapped ion system with the fidelity over 99.99%. Through the camera or multi-channel PMT, we can detect the state of qubits with a reasonable time.

There remain several technical problems in the trapped ion system. One is the non-uniform spacing of the ions in the vacuum chamber, which raises the difficulty of single ion addressing. Besides, when the number of ions is large, the frequency separation between motional modes becomes small, which limits the multi-qubit gates through the motional bus. Lastly, I want to mention that the gate time in the trapped ion system (now about μs) may be a limitation for operation with a large number of quantum gates, where quantum speedup happens, but still with a painful time.

1.3　Thesis organization

In chapter 2, I will give the general architecture for our trapped ion system, and describe the motion of an ion in our trap. Then, I will explain how to capture the ion, which includes the ionization, cooling and repumping processes.

In chapter 3, I will present the quantum control of the ion, where the introduction of the Hilbert space for a single ion is our starting point. Then, I will present the mechanism of initializing, manipulating, and detecting of the qubit, except the theoretical description, I will also show our experimental performance data.

In chapter 4, I would like to mention several techniques involved in our system, which are essential for building up a working experimental platform.

Chapter 5 and 6 are the two experimental works that I have accomplished during my Ph.D. career, where the molecular electronic structure problem and molecular vibronic spectroscopy problem in quantum chemistry field are simulated with our trapped ion system.

Chapter 7 is the conclusion and outlook.

第2章　Trapped ^{171}Yb$^+$ ion system

There are several existing types of ion traps used by different groups around the world. During my Ph.D. research career, I have been using the four-rod trap and the segmented blade trap, both of which belong to the type called the Paul trap, shown in Figure 2.1. The Paul trap generates the trapping potential via the combination of static electric field and oscillating electric field[16]. Although there are many groups considering the fabricated traps with more electrodes (e.g., Sandia National Laboratories High Optical Access Trap), for ion-shuttling or uniform spacing of multi-ions. The work introduced in this thesis, our homemade primary trap, showed excellent performance with a single ion.

2.1 Dynamics in the Paul trap

2.1.1 The overview of our trapped ion system.

The general components of our trapped ion system are illustrated in Figure 2.2 (a), where the ion trap sits inside an ultra-high vacuum (UHV) chamber. We apply a designed electric field to the electrodes of the trap to form the potential that confines the ions in space. With the assistance of the Field-Programmable Gate Array (FPGA), a conventional computer is used to control the experiment instruments and experiment running sequence. We use the microwave and lasers to realize state initialization and quantum control of the qubits. With a fluorescence detection system, we obtain the measurement data of the qubits and finally send the data back to the conventional computer.

The two essential properties that make trapped ion systems serve as the current leading quantum computer candidate are: (a) trapped ion system uses the qubits from nature, which guarantees the identity of qubits throughout the world and (b) the qubits are well isolated from the environment noise due to the using of the ultra-high vacuum system[17]. In our experimental setup, we can maintain the vacuum at the level of 10^{-11} Torr with a Ti-sublimation pump and the ion-pump. In such a vacuum condition, the background collisions from the background particles are close to negligible.

The traps I am mentioning in my thesis are the four-rod trap and the segmented blade trap, where we apply a static electric field and oscillating electric field together to generate the 3-dimension confinement field for the ions; this principle will be discussed in section
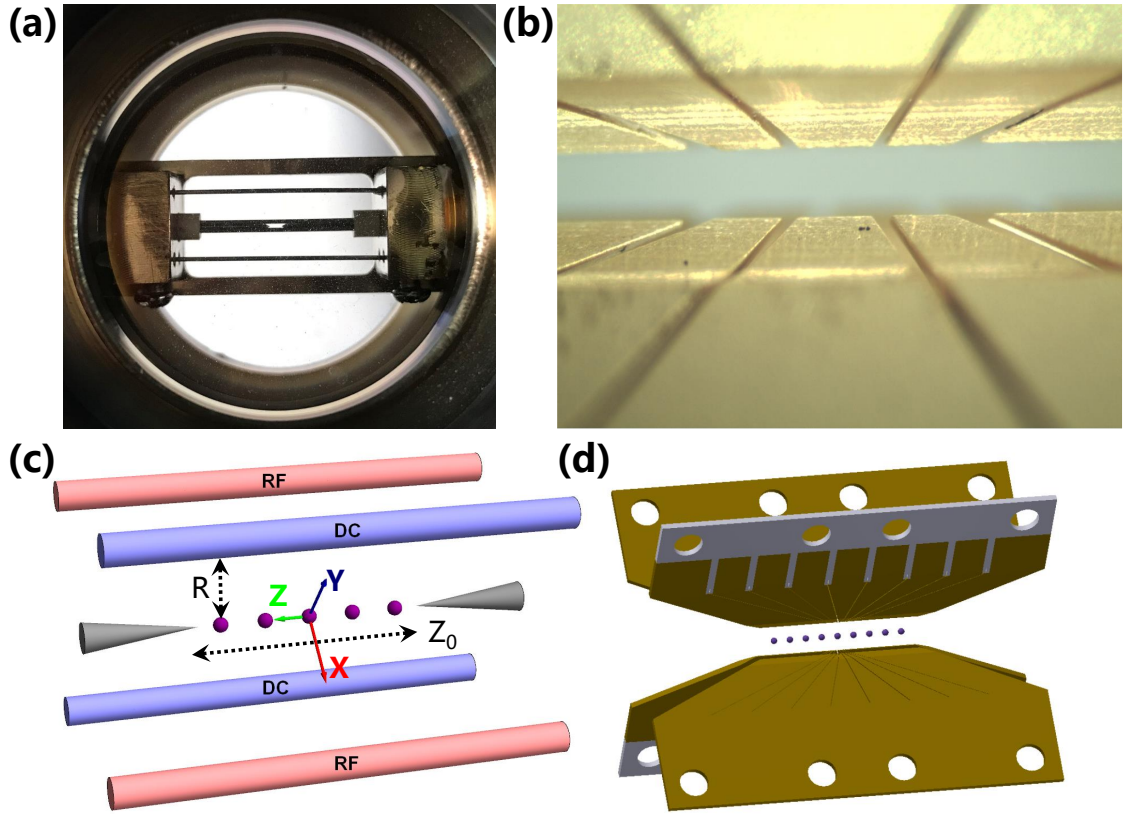
图 2.1　The four-rod trap and the segmented blade trap. (a) and (b) The four-rod trap and five-segment blade trap used in our laboratory. (c) and (d) The sketch-up diagram of the four-rod trap and segmented blade trap, the purple balls are illustrated as ions. In the four-rod trap, we apply a static electric field on the rods labeled with DC and apply a radio frequency field on the rods labeled with RF. Beyond that, we apply a DC field on the gray electrodes to form the confinement in the Z direction. This electric fields configuration generates the potential null in space, where ions can be held stably. For the segmented blade trap, we use the blades to replace the four-rod, and each blade contains several electrodes. With segmented blade trap, we get more freedoms of control for generating the trap potential that we are interested in.

(a)

(b)
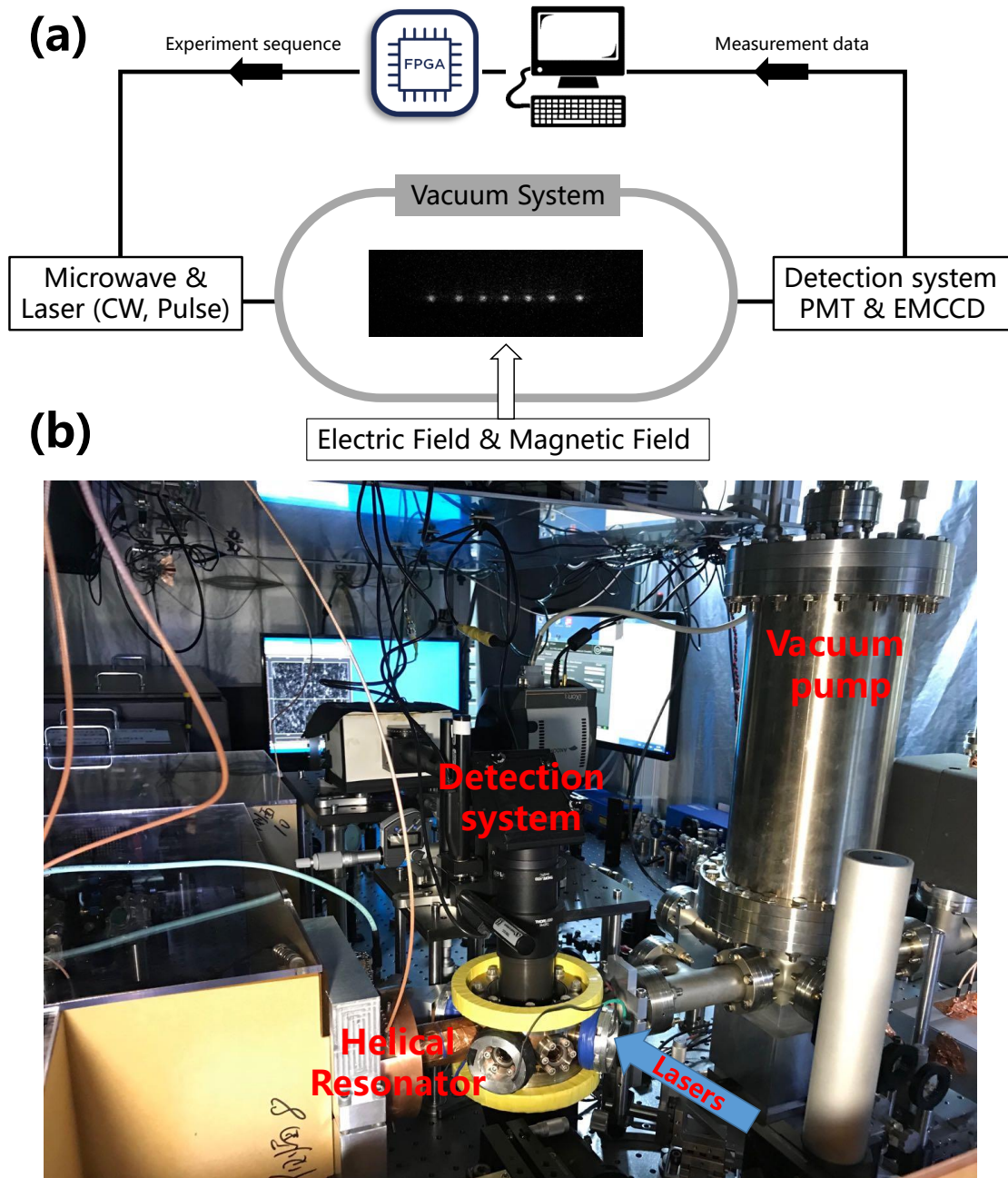
图 2.2　The overview of our trapped ion system. (a) The general components involved in our trapped ion setup. With the assist of FPGA, the software in the conventional computer controls the experiment instruments and experiment sequence in high precision and synchronization. We use microwave and lasers (continuous-wave lasers and pulsed laser) to realize the quantum control of qubits. The detection system of fluorescence count provides the quantum measurement result of the qubits. (b) A photo of our trapped ion experimental setup in the laboratory.

2.1.2. The static magnetic field is generated by the Helmholtz coil, which is essential to define the quantization axis and separate the Zeeman states.

The LabView software program is running on our conventional computer to control the experiment instruments through the connection of USB, network et al. We synchronize and control instruments with FPGA in high precision; the minimum time resolution of our FPGA board is 5 ns, which is precise enough for our typical experiment sequence (the length of one single sequence in our experiment is about a few microseconds to milliseconds).

The qubit used in our trapped ion system is based on the atomic energy levels. We use the continuous-wave lasers to realize the generation of ion, initialization of the qubits and the readout of the qubits. For the Hilbert space manipulation, at the early stage of developing our system, we used the microwave (12 GHz) to manipulate the hyperfine levels of the ion. Recently, we are using the controlled picosecond pulsed laser to manipulate the hyperfine levels and motional degree of freedom.

The qubits readout is based on the fluorescence detection scheme. An imaging system collects the fluorescence photons and delivers them to the photon counting device: Photomultiplier detector (PMT) or Electron-Multiplying charge coupled device (EMCCD). The EMCCD is essential for the state detection of multi-ions, where the spacial information of the ion chain is needed. The details are in section 3.4.

2.1.2 The motion of a trapped ion

In this section, I would like to describe the motion of an ion in the Paul trap with the applied electric fields on electrodes. Here, we take the four-rod trap as an example, and the segmented blade trap can be understood similarly. The details of math derivation can be found in Ref. [18].

We define R as the distance from the ion chain to the electric rods (colored in blue and red), and the principal axis is labeled as X, Y and Z shown in Figure 2.1 (c). The RF electric field on the red rods is $V_0 \cos \Omega_T t + V_{off}$, where V_0 is the amplitude of oscillating electric field, Ω_T is the frequency of oscillating electric field, and V_{off} is the offset voltage that typically used for the splitting of two radial motional modes. The DC electrodes are connected to electrical ground. Then the potential near the center of the trap in (x, y)

plane can be written as[19]

$$\phi(X, Y) = \frac{V_0 \cos \Omega_T t + V_{off}}{2} \left(1 + \frac{X^2 - Y^2}{R^2}\right) \tag{2-1}$$

The potential generated by the static electric field on the needle electrodes (gray color electrodes in Figure 2.1 (c)),

$$\phi(Z) = \frac{V_{needle}}{Z_0^2} \left[Z^2 - \frac{1}{2}(X^2 + Y^2)\right] = \frac{m}{2e} \omega_Z^2 \left[Z^2 - \frac{1}{2}(X^2 + Y^2)\right] \tag{2-2}$$

where V_{needle} is voltage on the needle electrodes, m is the mass of ion, e is the charge of the ion, and Z_0 is the half of the distance between two needles. Then, our axial trap frequency (along Z direction) is $\omega_Z = \sqrt{2eV_{needle}/(mZ_0^2)}$.

To obtain the motion of an ion in the (X,Y) plane, we need to combine Eq. (2-1) and Eq. (2-2), and rewrite them in the form of Mathieu Equations:

$$\frac{d^2X}{d\tau^2} + [a_X + 2q_X \cos(2\tau)] X = 0 \ , \ \frac{d^2Y}{d\tau^2} + [a_Y + 2q_Y \cos(2\tau)] Y = 0 \tag{2-3}$$

where $\tau = \Omega_T t/2$, $a_X = (4e/(m\Omega_T^2))(V_{needle}/Z_0^2 - V_{off}/R^2)$, $a_Y = (4e/(m\Omega_T^2))(V_{off}/R^2 + V_{needle}/Z_0^2)$, $q_X = 2eV_0/(\Omega_T^2 mR^2)$ and $q_Y = -q_X$. The value of q_X is a very important parameter for checking the stability of the trap. Typically, $q_X^2 \ll 1$ is required for the design of a good trap.

The exact solution for Mathieu Equations can be found in Ref. [19]. Here, in the approximation $|a_X| \approx 0, q_X^2 \ll 1$, we have the following conclusion:

$$X(t) \approx x_0 \left(\cos(\omega_X t)\left[1 + \frac{q_X}{2}\cos(\Omega_T t)\right] + \sqrt{a_X + q_X^2/2}\frac{q_X}{2}\sin(\omega_X t)\sin(\Omega_T t)\right) \tag{2-4}$$

where $\omega_X = \sqrt{a_X + q_X^2/2}\frac{\Omega_T}{2}$, is the trap frequency in X direction. We can derive the motion in Y direction Similarly and $\omega_Y = \sqrt{a_Y + q_Y^2/2}\frac{\Omega_T}{2}$.

We use our experimental setup parameters to simulate the motion of ion in the trap: $e = 1.6 \times 10^{-19}$ C, $m = 171 \times 1.66 \times 10^{-27}$ kg, $V_0 = 300$ V, $V_{off} = 5$ V, $V_{needle} = 10$ V, $R = 0.46$ mm, $Z_0 = 1.3/2$ mm, and $\Omega_T = (2\pi)12.5$ MHz.

In Figure 2.3, we show the numerical simulation result for the motion of the ion in the X direction ($\omega_X = (2\pi)1.16$ MHz, $\omega_Y = (2\pi)1.42$ MHz), as we can notice, the ion not
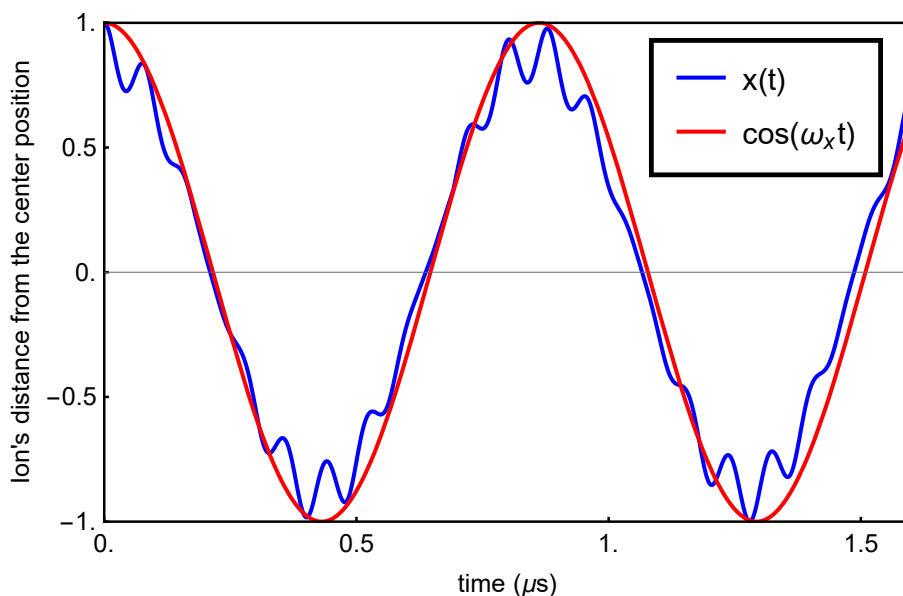
图 2.3　The numerical simulation result for the motion of an ion in the four-rod trap. Here, we only plot the motion of the ion in the x-direction of radial modes. The blue curve is the direct numerical calculation, and the red curve is the plot of oscillation with the trap frequency ω_x. The difference comes from the oscillating with trap frequency Ω_T, known as micro-motion.

only moves with the slow motion as the trap frequency, but also feels the micro-motion at the frequency Ω_T. In the four-rod trap design, we also add the micro-motion competition electric rods to reduce the effect of micro-motion. In the axial direction Z, the ion moves in the harmonic oscillator, with frequency $\omega_Z = (2\pi)\,0.83$ MHz. The above configuration of trap frequencies is the typical situation (with small RF power) for the ion-loading stage.

2.1.3　Helical Resonator

　　To provide a reasonable strength of trapping electric field, we need to apply a large amplitude of RF field, with V_0 typically ranging from 100 V to 1000V. Since the electrodes in the trap are open in space, this means only a small current flows through electrodes, and we only need a big amplitude of voltage. However, we cannot directly apply high voltage from the commercial signal generator to the trap, which is due to the miss of impedance matching, and will cause a big reflection back to the signal generator.

　　As proposed about 60 years ago by Macalpine, WW and Schildknecht, RO in Ref. [20], the use of RF quarter-wave helical coil resonator (we also call it as Helical Resonator) can entirely solve this problem. The Helical Resonator amplifies the RF signal from our standard source and delivers the high voltage to trap electrode through vacuum feed-through connection.

The Helical Resonator consists of three parts: (a) A helical cylinder tube that is connected to electrical ground. (b) A small coil inside one end-cap that takes the signal from the RF generator. We also call this the antenna. (c) A big inner coil (inside the helical cylinder tube) that is coupled with the antenna and connected to the vacuum feed-through. The quality factor Q is introduced to characterize the performance of a Helical Resonator, which can be experimentally measured as $Q = \Omega_T / \delta\Omega_T$, where $\delta\Omega_T$ is the frequency bandwidth of the Helical Resonator. This relation gives us an idea: for the same frequency of RF field Ω_T, the higher Q we achieve, the narrower band-pass filter we have. Therefore, the Helical Resonator not only plays the role of a voltage amplifier but also act as a proper frequency band-pass filter, which is very important for isolating the ions from other unwanted electric field noise.

To achieve a higher Q of the resonator, except for the careful design of geometric dimensions, when we assemble the resonator experimentally, the antenna is an essential part to adjust, where the number of turns and the length of the coil affect Q a lot. In the experiment, we need to iterate the adjustment to make an optimal antenna.

The output voltage of the Helical Resonator takes the following form

$$V_0 = A\sqrt{PQ} \tag{2-5}$$

where the constant A depends on the exact geometries of the Helical Resonator. P is the power that Helical Resonator takes. From experimental experience, we can increase Q by cleaning the Helical Resonator tube and coil through chemical reagent, and in this way essentially reduce the power loss. For our four-rod trap, we use the Helical Resonator with resonant frequency $\Omega_T = 12.5$ MHz and achieve $Q \approx 200$. Note here, that the resonant frequency of Helical Resonator with the trap attached is almost half of the case without any load; this is due to the mechanism of two capacitors parallel connection, where the trap can be treated as a similar magnitude of capacitor with the Helical Resonator.

2.2 Trapping of ^{171}Yb$^+$ ion

2.2.1 Ionization of the atom

The ion species we are using in the laboratory is Yb$^+$. It is a hydrogen-like ion with relatively large mass; thus we can understand it more easily than a more complex molecule. Another benefit of choosing the Yb$^+$ is the electronic structure that provides us

with a good qubit (it was recently reported the 10 minutes coherence time of the qubit in Ref. [21]), and the qubit can be optically initialized, manipulated and detected with high fidelity. Furthermore, the laser requirement for Yb$^+$ ion is in a reasonable wavelength range, and all of our daily using lasers (370 nm, 399 nm, 935 nm, 638 nm) can be obtained directly from a commercial company.
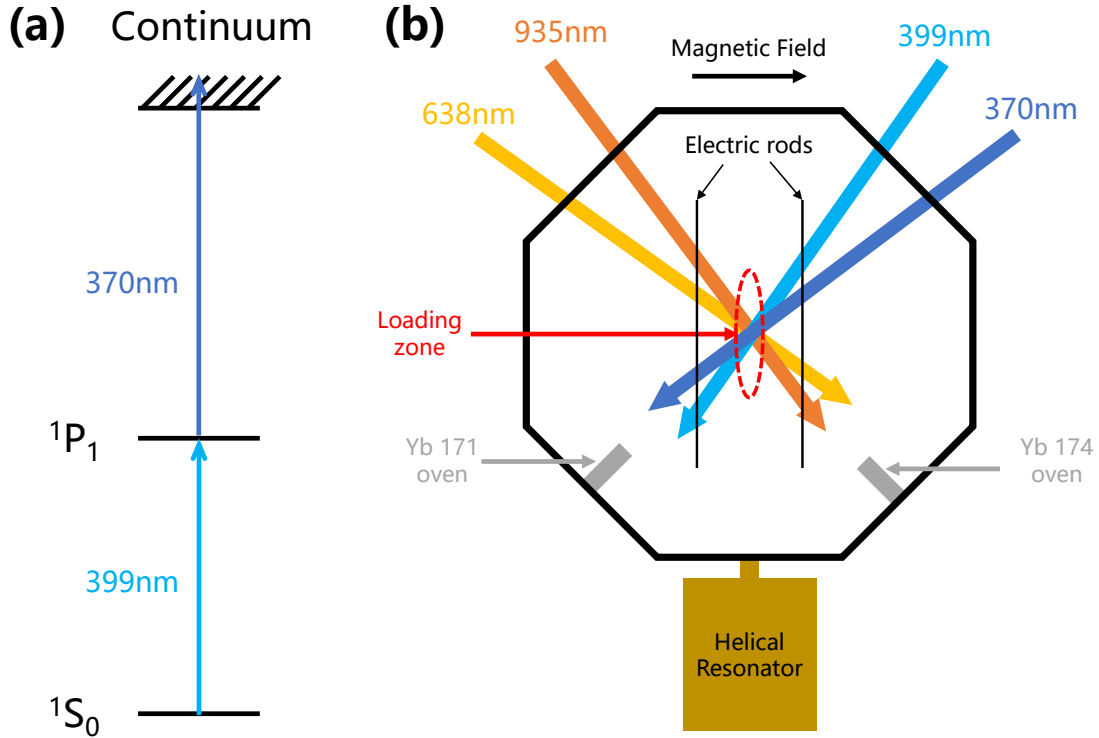
图 2.4　Loading of the Yb$^+$ ion. (a) The two-photon process to generate the ion. The wavelength of the 399 nm laser is dependent on the species of atom isotope, and the wavelength of the second excitation can be 370 nm or any other that is less than 394 nm. (b) Top-down view of our experimental loading setup. The ionization lasers and repumping lasers are overlapped in the vacuum chamber, where the loading zone forms. Two isotopes of Yb ovens are installed in the chamber. We can selectively turn on the oven and load the corresponding ions.

The ionization of Yb atom method we are using is based on the two-photon transition process[22]: The 399 nm continuous-wave laser makes the neutral atom transit from the $^1S_0$ state to the $^1P_1$ state, and another laser excites the atom from the $^1P_1$ state to the continuum with a wavelength less than 394 nm, as shown in Figure 2.4 (a).

We installed ^{174}Yb and ^{171}Yb atom ovens inside the chamber. The reason for using the ^{174}Yb atom is the zero spin of nuclei that make the ion with less dark state and better

cooling efficiency. The loading of ^{174}Yb$^+$ is always our first step to be implemented when we set up the system. Based on the trapped ^{174}Yb$^+$ ion, we can optimize the optical beam path, compensate the micro-motion, and fix other abnormal situations. Although the ^{174}Yb atom oven contains both ^{174}Yb and ^{171}Yb, we cannot use a single ^{174}Yb oven for the loading of ^{174}Yb and ^{171}Yb together, this is due to the Doppler broadening of the 399 nm laser, which causes the loading of many isotopes and generates dark ions, the situation becomes even severe when we need to load a string of ions. Thus we installed another ^{171}Yb atom oven, which contains around 95% of ^{171}Yb atom.

The experimental configuration for the loading of ions is shown in Figure 2.4 (b). The loading process starts with the turn-on of the electric current in the oven. Typically around 2 A to 3 A, and then after a few minutes, the atoms are heated up. Then the atomic beam is shot to the center of the trap, where the ionization laser beams focus. In this loading zone, the ions are generated, and by the confinement of the electric field (see section 2.1.2), the ions are trapped in the space. We lower our trapping electric potential when we load the ions. Thus atoms with relatively small velocities can be stopped and ionized. Before the ionization laser beam enters the chamber, we combine 399 nm and 370 nm lasers through a dichroic mirror (see section 4.1.1), so the overlap in the loading zone can be well guaranteed. We use about 1 mW of the 399 nm and 1 mW of the 370 nm for ion loading, and the beam size focusing on the loading region is about 80 μm in diameter.

Once we monitor the appearance signal of the ions, e.g., the signal of fluorescence photons observed by the PMT or camera, we stop the electric current that heats up the atomic oven. Depending on the number of ions, we will have a different count number of collected photons. Thus we can realize an automatized software program to control the process of ion loading, which is vital for the future trapped ion quantum computer.

Here, I want to mention the benefit of using a pulsed-laser for ion loading. Since the frequency requirement in the second excitation in the two-photon ionization process is less than 394 nm, our Raman pulsed-laser is working at the wavelength of 375 nm, so that we can use this Raman laser for ion loading. The advantage of using the Raman laser beam is that a significant power can accelerate the loading process.

2.2.2 Doppler cooling of the ion

After the atom is ionized in the loading zone, the ion still contains pretty big kinetic energy due to the initial high velocity of the atomic beam, so an additional step of cooling down the ion is needed. Here, I am going to introduce the standard operation in the laboratory: Doppler cooling.

In the experiment, we apply a laser beam that is red detuned from the main cycling transition between ^{2}S$_{1/2}$ and ^{2}P$_{1/2}$ as shown in Figure 2.5 (a). The Doppler cooling beam is part of the 370 nm laser beam, and the optical path can be found in section 4.1.1. This Doppler cooling beam is not perpendicular to any principal axis of the trap. As shown in Figure 2.4 (b), the 370 nm laser takes angles with two radial axes (X and Y) and the axial axes (Z). Thus, by this single laser beam, we can cool the three motional modes.

Except the optical transition between ^{2}S$_{1/2}$ |F = 1⟩ and ^{2}P$_{1/2}$ |F = 0⟩, we need an additional frequency component that is 14.74 GHz added to the original laser beam to realize the transition between ^{2}S$_{1/2}$ |F = 0⟩ and ^{2}P$_{1/2}$ |F = 1⟩, which is done by using an Electro-optic Modulator (EOM). In the experiment, we use the EOM that takes the input modulation frequency of 7.37 GHz (New Focus company, model: 4855), the 14.74 GHz frequency component is generated by the second-order sideband, and the intensity is about 1% of the original laser beam. In short, our Doppler cooling beam can cover the transitions shown in Figure 2.5 (a).

When the ion moves toward the Doppler cooling laser beam, due to the Doppler effect, the ion feels a blue-detuned laser frequency, which is larger than the laser beam frequency, resulting in a closer to the resonant transition between ^{2}S$_{1/2}$ and ^{2}P$_{1/2}$. So the ion absorbs more photons, which is equivalent to saying that the ion absorbs more kinetic energy when moving toward to the laser beam; thus the velocity of the ion would be reduced. For the other case, when the ion moves in the same direction as the laser beam propagates, the ion will see red-detuned frequency compared to the original frequency of the Doppler laser beam, which is more off-resonant to the main transition, the ion absorbs a small number of photons. On average, the ion can be slowed down in this scheme.

We note here, the confinement of the ion in space is guaranteed by the electric field, and the Doppler cooling beam can only cool down the motional modes. This is different from the trapping of atoms in a magneto-optical trap.

The Doppler cooled ion scatters out photons in a random direction, and these photons can in opposite heat up the ion. The minimum temperature of the ion with the Doppler
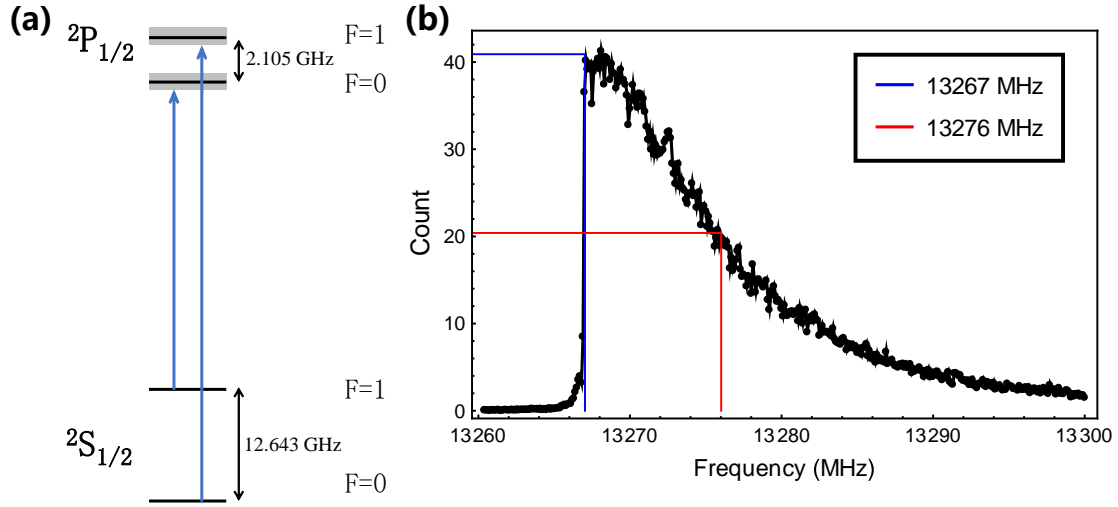
图 2.5 The Doppler cooling of an ion. (a) The Doppler cooling laser beam transition is between ^{2}S$_{1/2}$ and ^{2}P$_{1/2}$ with frequency red detuned. Here, the details of Zeeman levels are not shown. (b) The measured spectroscopy of Doppler cooling fluorescence counts with different frequency. The blue line points at 13267 MHz is the resonance frequency of the optical transition, and the red line at 13276 MHz corresponds to the value we are setting in a normal experiment.

cooling laser beam is achieved by setting the amount of the red detuning as $\gamma/2$[23], where γ is the line width of the excited state ^{2}P$_{1/2}$ and $\gamma = (2\pi)19.7$ MHz for ^{171}Yb$^+$.

Figure 2.5 (b) shows the spectroscopy of Doppler cooling count while we scan the 740 nm laser frequency. The 740 nm laser is the source of generating the 370 nm laser through second-harmonic-generator (SHG) crystal. We can notice the just resonance point is at frequency 13267 MHz, with collected count 41. Typically, we set the half count point, 20.5, which corresponds to 13276 MHz, as our Doppler cooling transition frequency. To make the meaning of numbers mentioned here clear, the frequency we are scanning is the EOM frequency for the iodine lock. For details, please refer to the section 4.2.1. Our detuning is $(2\pi)\, 2 \times 9$ MHz, which is more red-detuned from the best cooling case $\gamma/2 = (2\pi)\, 9.85$ MHz.

2.2.3 Repumping of the ion

Our main optical cycling transition is between ^{2}S$_{1/2}$ and ^{2}P$_{1/2}$. However, as we can see in Figure 2.6, there is a 0.5% probability of decaying out from the cycling transition to ^{2}D$_{3/2}$. In this case, we shine a laser beam at wavelength 935.1882 nm, about 15 mW with focal diameter 150 μm at ion position, exciting the dark state ^{2}D$_{3/2}$ to ^{3}D[3/2]$_{1/2}$. This laser should carry a sideband of 3.1 GHz to cover all the transitions. The state ^{3}D[3/2]$_{1/2}$

is a metastable state and will take a chance of 98.2% back to the cycling transition.

For the 935 nm laser, we need to add a sideband with 3.1 GHz on the original beam to cover all the energy levels in the transition from $^2D_{3/2}$ to $^3D[3/2]_{1/2}$. Besides, for the laser polarization direction, we need to cover π, σ^+ and σ^- polarizations. In the experiment, we use half-wave-plate and quarter-wave-plate to optimize the polarization of the laser beam; the actual polarization can be measured by the polarization meter (from Thorlabs company, model: PAN5710IR).
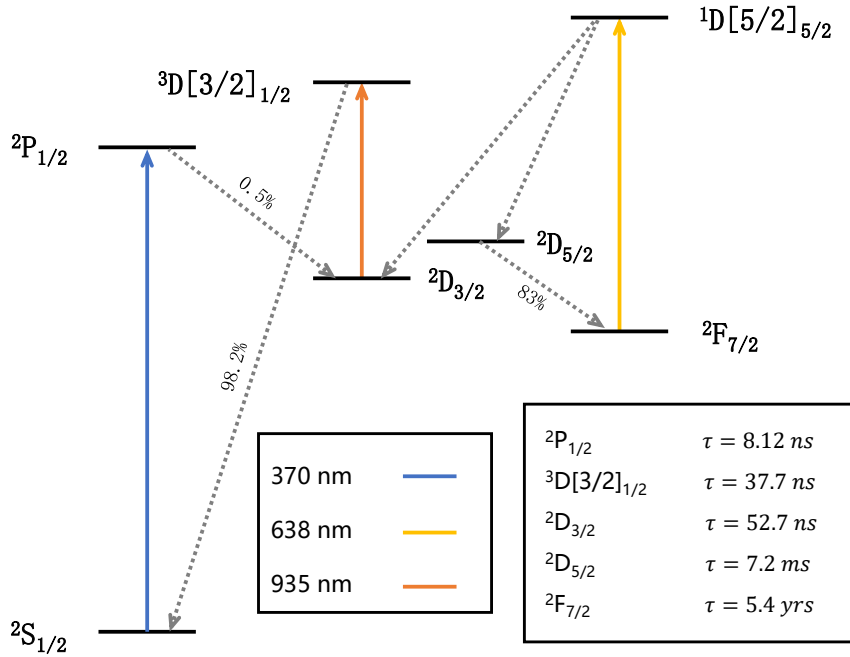
图 2.6　Energy level diagram with transitions and decays for ^{171}Yb$^+$. There is a probability for our ion to decay out from the main optical cycling transition ($^2S_{1/2}$ to $^2P_{1/2}$); we need additional repumping lasers (935 nm and 638 nm) to bring the ion back to main transition.

There is another long-lived dark state, $^2F_{7/2}$, and this state could be generated by the background collision from other particles in the vacuum. We can shine a laser beam at wavelength 638.6 nm to bring it back to the main transition. In the experiment, we seldom observe the event of using a 638.6 nm laser to bring a dark ion back to the main transition, and this could be explained as the low-event-rate of the ion becoming state $^2F_{7/2}$. But we do observe with the Raman laser, picosecond pulsed laser at wavelength 375 nm can bring the dark ion back with pretty high efficiency. This is probably the reason that the ion becomes YbH$^+$, and the pulsed-laser deforms this molecule.

The sidebands we are using in the Doppler cooling and the 935 nm laser beam are generated by the Electro-optic Modulator (EOM). The EOM takes the input radio

frequency $\beta \sin(\omega_{\mathrm{EOM}}t)$ to modulate the laser beam $Ae^{i\omega_{\mathrm{laser}}t}$. Here, β is the modulation amplitude of the RF signal, A is the amplitude of the laser, ω_{EOM} is the frequency of the modulation signal, and ω_{laser} is the frequency of the original laser beam. The phase modulation effect can be written in the Jacobi-Anger expansion

$$Ae^{i\omega_{\mathrm{laser}}t+i\beta\sin(\omega_{\mathrm{EOM}}t)} = Ae^{i\omega_{\mathrm{laser}}t}\left(J_0(\beta) + \sum_{k=1}^{\infty} J_k(\beta)e^{ik\omega_{\mathrm{laser}}t} + \sum_{k=1}^{\infty}(-1)^k J_k(\beta)e^{-ik\omega_{\mathrm{laser}}t}\right)$$
(2-6)

where J_α is the first kind of Bessel function.

From Eq. (2-6), we can see that the strength of the sidebands is controlled via the modulation amplitude β, proportional to $|J_\alpha(\beta)|^2$. As shown in Figure 2.7 (a), to maximize the strength of the second-order sideband, we need to set the modulation amplitude to $\beta \approx 3.054$, and this is considered as the best situation for Doppler cooling beam with high cooling efficiency. However, huge power of the modulation signal may damage the crystal in EOM. Thus we cannot set arbitrary large β in a real experiment. In Figure 2.7, we show the oscilloscope capture of the modulated 935 nm laser signal in an optical cavity, and the laser carries a 3.1 GHz sidebands after passing through a fiber-EOM (from EO Space company). The laser is sent to an optical cavity (Thorlabs company, model SA200-8B); the Free Spectral Range of the cavity is 1.5 GHz, and the Finesse is about 250. Then we scan the length of the optical cavity to observe the resonance peak. From the signal, we read that the strength ratio between the first order and zero order is about 70%.

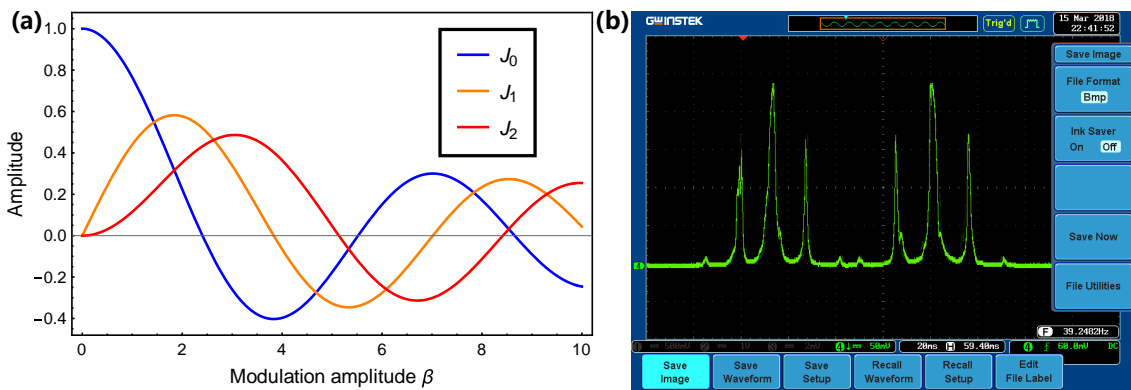图 2.7　The generation of laser frequency sidebands via Electro-optic Modulator. (a) The numerical plot of Bessel function $J_0(\beta)$, $J_1(\beta)$ and $J_2(\beta)$ as the various of modulation amplitude β. (b) The 935 nm laser carries a 3.1 GHz sideband and we send this laser beam into an optical cavity, the signal shown on the oscilloscope is obtained via scanning the length of the optical cavity.

第3章 Quantum control of ^{171}Yb$^+$ ion

3.1 The Hilbert space of single ^{171}Yb$^+$ ion

3.1.1 The four-level system

The ^{171}Yb$^+$ ion has a spin-1/2 nucleus ($I = 1/2$), resulting in a hyperfine structure in the electronic ground state ^{2}S$_{1/2}$, as shown in Figure 3.1 (a). The total angular momentum of the ion is $\hbar\sqrt{F(F + 1)}$, and the total angular momentum quantum number F = J + I = L + s + I, where $\hbar = h/2\pi$, h is the Planck's constant, L is the anular momentum of the electron, s is the spin of the electron, and m$_F$ is the projection along the quantization axis. For the manifold ^{2}S$_{1/2}$, F = J + I = J + 1/2 = L + s + 1/2 = 0 + 1/2 + 1/2 = 1, thus we have the hyperfine splitting of F=0 and F=1. In the F=1 level, due to the Zeeman effect introduced by the magnetic field, three sub-levels are generated $|F = 1, m_F = 0\rangle = |\uparrow\rangle$, $|F = 1, m_F = -1\rangle = |-\rangle$ and $|F = 1, m_F = 1\rangle = |+\rangle$.

The two hyperfine states ^{2}S$_{1/2}$ $|F = 0, m_F = 0\rangle$ and ^{2}S$_{1/2}$ $|F = 1, m_F = 0\rangle$ form a spin-1/2 system, noted as $|\downarrow\rangle$ and $|\uparrow\rangle$, respectively. We also call it the "clock qubit", which is magnetic field insensitive, and this qubit contains a long enough coherence time.
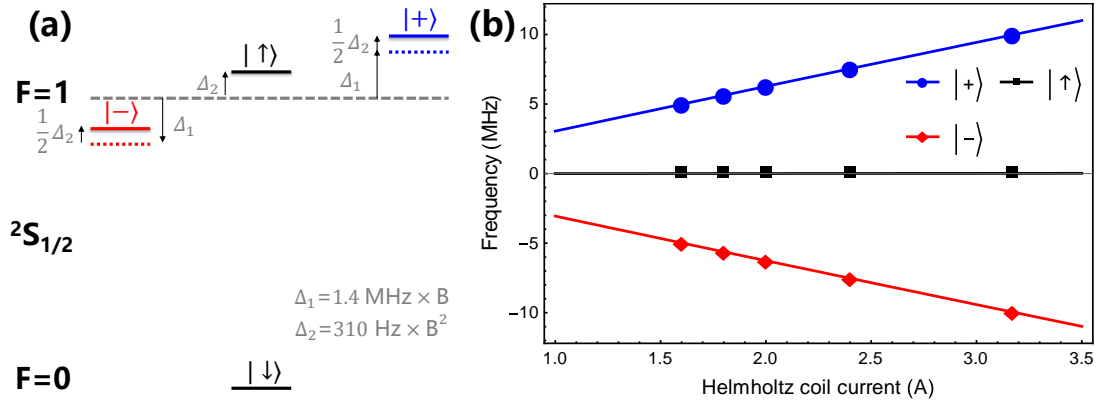
图 3.1 The four-level system in our trapped ion and the Zeeman splitting. (a) The four energy levels stored in the ^{2}S$_{1/2}$ manifold construct our four-level system, where the states in F = 1 is generated by the Zeeman splitting. (b) The Zeeman splitting gaps vary as the magnitude of the static magnetic field, and our magnetic field is generated by the Helmholtz coil. The black curve with dots is the state $|\uparrow\rangle$, and the blue and red curves imply the state $|+\rangle$ and $|-\rangle$. The state $|\uparrow\rangle$ takes a tiny second-order Zeeman shift as the strength of magnetic field increase, the state $|+\rangle$ and $|-\rangle$ mainly take a first-order shift, which is a linear change.

The four-level system refers to the four energy levels labeled $|\downarrow\rangle$, $|\uparrow\rangle$, $|+\rangle$ and $|-\rangle$ in ^{2}S$_{1/2}$ manifold, shown in Figure 3.1 (a). A static magnetic field is essential for our trapped ion quantum computer, and the Zeeman splitting of the energy levels in the state F = 1 is introduced by the magnetic field B. In Figure 3.1 (b), we show the experimentally measured result of Zeeman splitting as the change of magnetic field strength. We use the Helmholtz coil to generate the static magnetic field, where the direction of the magnetic field is perpendicular to our optical-table in the lab. In the experiment, we observed that the ion scatters almost no photons when we do not apply any magnetic field (only the magnetic field provided by the earth exits). As we increase the electric current in the Helmholtz coil, the Zeeman splitting increases. For our typical experiment, we set a Zeeman splitting around 10 MHz.

The Zeeman splitting we are considering contains two parts: the first-order splitting (1.4 MHz × B) and the second-order splitting (310 Hz × B^2). As we can see in Figure 3.1 (a), the state $|\uparrow\rangle$ only contains the second-order splitting, which is described as magnetic field insensitive and forms an excellent qubit with $|\downarrow\rangle$ state. The state $|+\rangle$ and $|-\rangle$ contain the first-order and second-order splitting, which is very sensitive to the fluctuation of the magnetic field. We experimentally measured that the coherence time of $|+\rangle$ and $|-\rangle$ state is around 400 μs without the magnetic field shielding technique in our system.

3.1.2 The motional modes of a trapped ion

Our ions are trapped via the combination of static electric field and oscillating electric field, as discussed in section 2.1.2, and we assume the motion of the ion along the principal axis follows the harmonic oscillator. In the experiment, for our typical operation with a linear chain of ions, the trap frequency in axial modes ω_Z is much smaller than the radial modes ω_X and ω_Y. The balance between the Coulomb repulsion (between the ions) and the confinement from the Z direction (ω_Z) provides the ions an equilibrium distance between them. We do not want to make ω_Z too large, as that leads the ions to move out of the potential null in the (X, Y) plane, which results in the large micro-motion region.

For an N-ion system, there are N modes along each of the three directions, and typically $\omega_X \approx \omega_Y \gg \omega_Z$. Since we are dealing with only one ion across my thesis, there are three vibrational modes (or we call motional modes) in the trap, noted with trap frequency ω_Z, ω_X and ω_Y. If we do not apply any offset voltage in Eq. (2-1), then the mode frequency of ω_X and ω_Y are the same. Therefore, in the experiment, we apply a DC

offset voltage to separate ω_X and ω_Y.
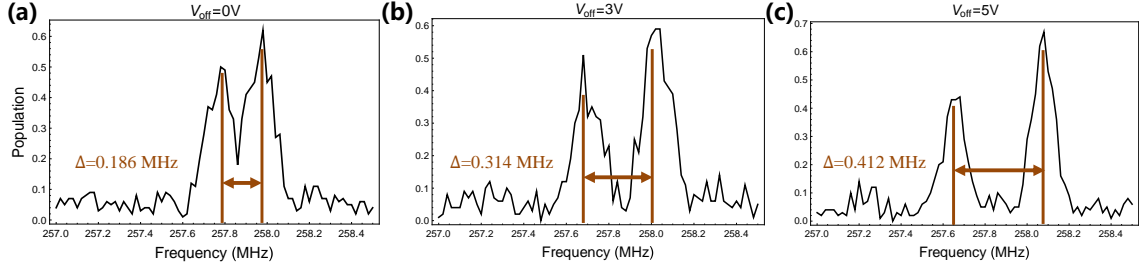
图 3.2 The frequency separation of two radial motional modes. We experimentally change the offset voltage V_{off} in the oscillating electric field of two RF electric rods and measure the red sideband excitation via scanning the frequency of Raman laser. (a), (b) and (c) correspond to the amplitude of V_{off} as 0 V, 3 V and 5 V, respectively.

In the experiment that involves the motional degree of freedom, we need to add a suitable voltage to separate X and Y motional modes, to achieve a successful sideband cooling and operations on both modes. Here, we apply two counter-propagating Raman laser beams to excite the red sidebands of radial motional modes X and Y. The Raman laser beams are perpendicular to the axis of ion chain (Z direction), thus the axial mode will not be excited. In the Raman laser configuration (see section 3.3.3), we scan the frequency of AOM1 to excite different motional modes, which is a resonant frequency measurement of the motional modes without cooling down the motional modes to the ground state.

In Figure 3.2, we show our measured experimental result with the change of offset voltage on the RF electrodes, which breaks the symmetry of the electric potential inside the trap. As we can notice, when there is no external offset voltage applied on the RF rods, we can observe a small separation between two motional modes, which is possibly due to the non-perfect geometric symmetry of the rods during the trap assembly stage or the laser propagation direction misaligns with the principal axis. As we keep increasing the voltage V_{off}, we can better distinguish between X and Y modes, and we usually set the frequency separation to about 0.4 MHz in the experiment.

3.2 Quantum state initialization

3.2.1 Optical pumping to the Ground state of hyperfine levels

The optical pumping laser beam initializes the state of the ^{171}Yb$^+$ ion to the hyperfine ground state ^{2}S$_{1/2}$ $|F = 0, m_F = 0\rangle$. The electronic transition of optical pumping is shown

in Figure 3.3. The optical pumping beam is part of the 370 nm laser beam, and the optical path of generating optical pumping beam can be found in section 4.1.1. An additional frequency sideband (2.105 GHz) is needed to cover the transition from ^{2}S$_{1/2}$ $|$F = 1$\rangle$ to ^{2}P$_{1/2}$ $|$F = 1$\rangle$. We use the EOM from New Focus company (model: 4431 Visible Phase Modulator) to generate the sideband. As described in section 2.2.3, the ion could decay out the main transition to the ^{2}D$_{3/2}$ state. In the experiment, we always shine the 935.18 nm laser to bring the ion back to the main cycling transition from the dark state.

In the experiment, after applying the Doppler cooling beam for 1 ms, we apply 5 μs of the optical pumping beam, then detect the ion's fluorescence photons with the detection beam. Typically, we achieve an initialization fidelity to the $|\downarrow\rangle$ state with 99.5 %, which we believe the main limitation comes from the state detecting fidelity of the qubit.

3.2.2　Sideband cooling to the Ground state of motional modes

After the optical pumping process, the state of the ion becomes hyperfine ground state $|\downarrow\rangle = {}^2S_{1/2}$ $|$F = 0, m$_F$ = 0$\rangle$, and the ion reaches the temperature limit T by Doppler cooling, staying as a thermal state in the motional modes. We assume the average phonon number for the thermal state is $\bar{n}$, and the phonon distribution of the motional states follows the Maxwell-Boltzmann distribution:

$$P_n = \frac{1}{1+\bar{n}} \left(\frac{\bar{n}}{1+\bar{n}} \right)^n e^{-n\hbar\omega/K_B T} \tag{3-1}$$

where K_B is the Boltzmann constant, and ω is the frequency of the harmonic oscillator. To obtain the average phonon number $\bar{n}$, one traditional way is comparing the oscillation heights of the red sideband and blue sideband transitions, which has a relation $\bar{n}/(\bar{n}+1)$[19]. However, this method requires the laser beam power to be equal in the blue sideband and red sideband, which is not guaranteed in our system. The reason comes from the different frequency applied on the AOM, which results in the different shifting angle of the laser beam from the AOM; thus, the laser focus point at the ion's position is not exactly same. For details on the Raman laser-induced transition, please refer to section 3.3.3.

Here, we use the Carrier Rabi-oscillation signal to fit the average phonon number distribution in the motional modes. The advantage is the longer coherence time of the carrier transition via Raman laser compared to the blue (red) sideband. We experimentally measure the so-called Debye-Waller factors, which states that the carrier Rabi frequency is dependent on the phonon number n with the factor $L_n^0(\eta^2)$, where $L_n^\alpha(x)$ is the generalized
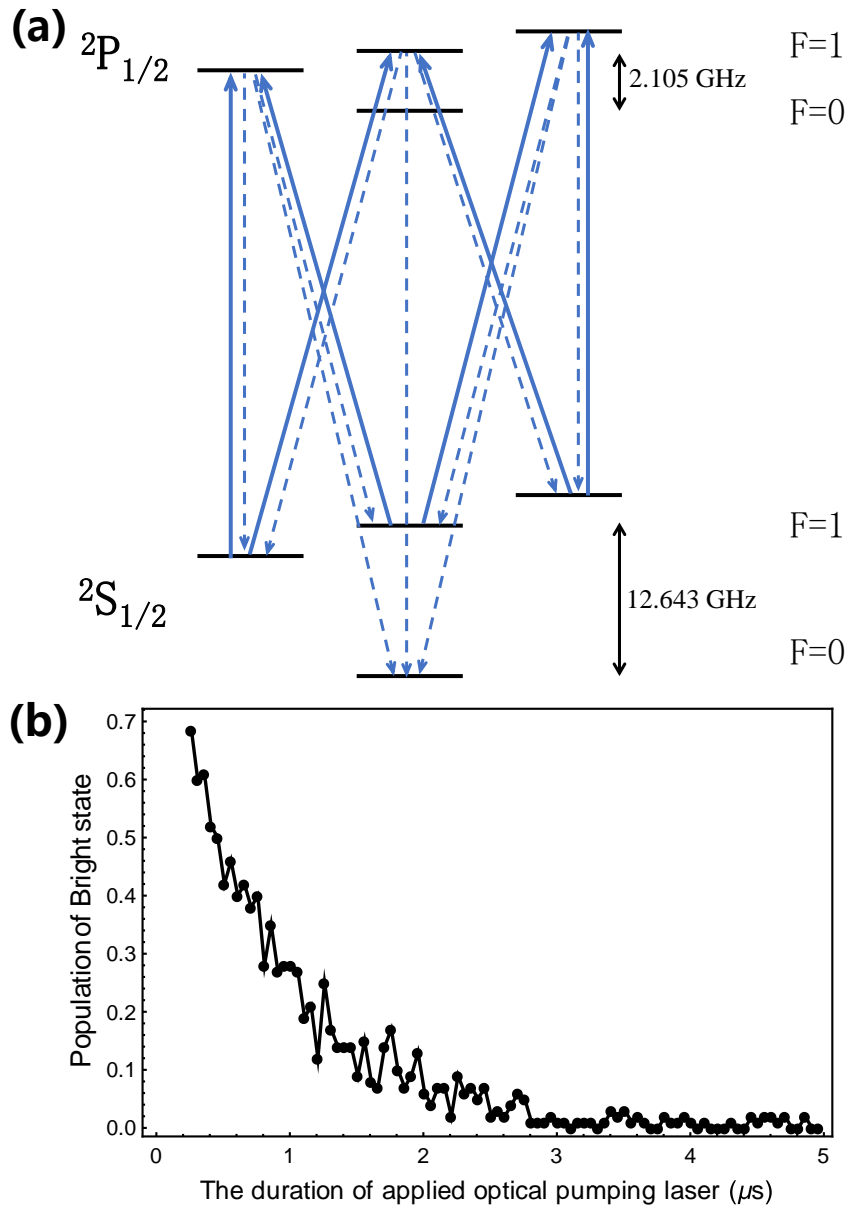
图 3.3 The optical pumping transition and the hyperfine ground state initialization. (a) For the optical pumping electronic transition, the laser is phase modulated with a 2.105 GHz RF signal to generate the frequency sideband, which couples the transitions from ^{2}S$_{1/2}$ $|F = 1\rangle$ to ^{2}P$_{1/2}$ $|F = 1\rangle$. The solid lines are the laser-induced optical transitions, and the dashed lines are the spontaneous decay. (b) The brightness of the ion as the change of optical pumping duration, where the ion is Doppler cooled 1 ms and then followed by the optical pumping laser beam with different duration. Finally, we detect the photons scattered from ^{2}S$_{1/2}$ $|F = 1\rangle$ state with a detection beam. Typically, we use the duration of 5 μs for the optical pumping process in the experiment, which corresponds to an initialization fidelity 99.5% of the $|\downarrow\rangle$ state.

Laguerre polynomial, and η is the Lamb-Dicke parameter.

When we experimentally apply a Carrier Raman laser to the ion after optical pumping, the collected photon flourresence is

$$P(t) = \sum_{n=0}^{\infty} \frac{1}{1+\bar{n}} \left(\frac{\bar{n}}{1+\bar{n}} \right)^n \sin^2(\pi e^{-\eta^2/2} L_n^0(\eta^2)\Omega_{car}t) \qquad (3\text{-}2)$$

where ω_{car} is the Rabi frequency of the carrier transition when the ion is at the motional ground state.
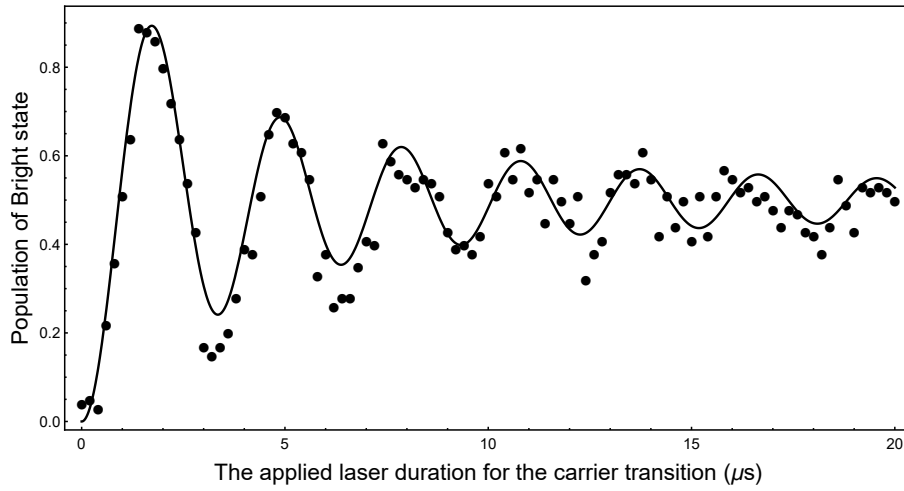
图 3.4 Experimental measurement of the average phonon number of an ion after Doppler cooling. We use the Rabi oscillation signal of the carrier transition to fit the average phonon number. The ion is Doppler cooled and optically pumped to the hyperfine Ground state, and is followed by a Raman carrier laser to resolve the average phonon number. In the figure, dots are experimental data, and the solid curve is the fitting result. We assume the ion is in a thermal state with average phonon number $\bar{n}$, and we fit the experimental data with Eq. (3-2). The fitting result shows the average phonon number is 19.

In Figure 3.4, we show our experimentally measured the Rabi oscillation of the carrier transition after Doppler cooling, where we vary the duration of the applied Raman laser to obtain the oscillation. The fitting parameter η used here is 0.11, and we truncate the maximum phonon number at 200, which is big enough for the thermal state fitting.

In the experiment, we need additional sideband cooling, to cool down the ion to the ground state of the motional modes. Figure 3.5 illustrates the sideband cooling process for the motional modes, which cools down the ion from the thermal state to the ground state in the harmonic motion. We use the red sideband to reduce the phonon number, and the optical pumping laser beam can bring the state to $|\downarrow\rangle$. After repeating this procedure

several times, we can cool down the ion to the motional ground state. Here, we only take one mode as an example; for more motional modes, we can cool each mode alternatively.
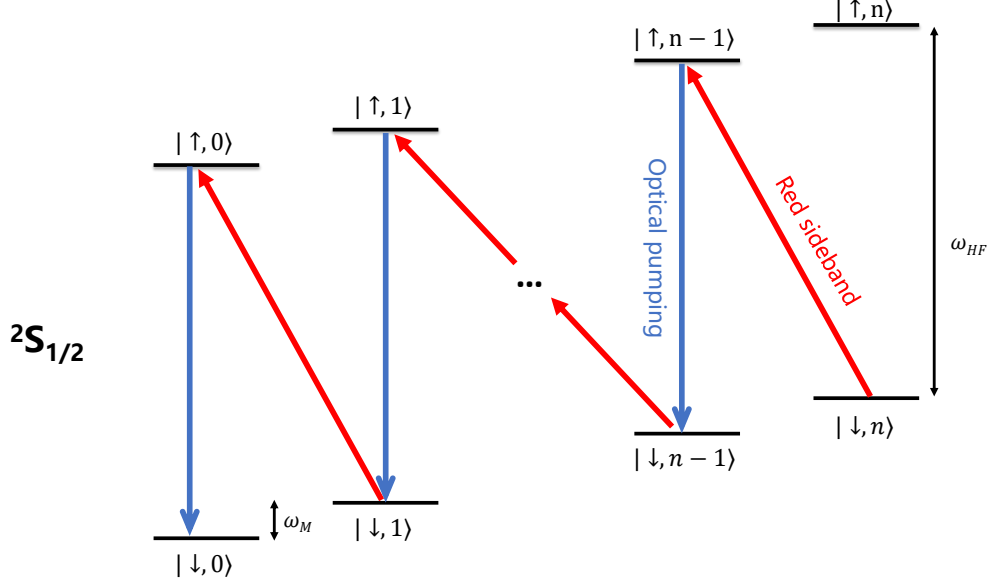
图 3.5　Schematic diagram for the sideband cooling of motional modes. The ion is first optically pumped to the hyperfine ground state $|\downarrow, \bar{n}\rangle$ after Doppler cooling, with a thermal distribution in the motional harmonic oscillator. We apply a red sideband laser to bring the state from $|\downarrow, n\rangle$ to $|\uparrow, n-1\rangle$, then follow it with an optical pumping transition, and the state becomes $|\downarrow, n-1\rangle$. In the experiment, we repeat this sequence for both X and Y modes in the radial direction for 100 times, and the ion is finally cooled to the motional ground state $|\downarrow, 0\rangle$. In the figure, ω_{HF} is the hyperfine splitting, and ω_M is the trap frequency of the motional mode.

For the implementation of sideband cooling procedure, we first guess a Rabi frequency of the red sideband transition, and then we implement the sideband cooling. After that, we scan the Rabi oscillation of the red sideband transition and get the Rabi frequency of the red sideband by fitting the experimental data. Typically, we need to iterate these steps 2 to 3 times to find the best parameter set for the experiment. Our sideband cooling cools the ion to an average phonon number $\bar{n} = 0.012$, with 98.8% phonon occupied on the ground state $|\downarrow, n = 0\rangle$.

The electrical noise and other radiation noise on the electrodes can heat up the ion, which is not good for quantum computing. In the experiment, we use filters for the applied DC voltage and RF voltage, and we also use the copper plate to shield the cable exposed in space (reducing the noise coupled by the cable). We observed the reduction of the heating rate by these improvements. The heating rate of our four-rod trap is 4 phonon/second, and 50 phonon/second for our segmented blade trap with $\omega_M = (2\pi)2\mathrm{MHz}$.

3.3　Quantum state manipulation

3.3.1　Light-ion interaction

Till now, one single ^{171}Yb$^+$ ion provides us a good qubit with long coherence time $|\uparrow\rangle$ and $|\downarrow\rangle$, and a multi-level quantum system $|\uparrow\rangle$, $|\downarrow\rangle$, $|+\rangle$ and $|+\rangle$. Besides, the ion provides us a three dimensional harmonic oscillator with frequencies ω_X, ω_Y and ω_Z.

Here, we will mainly introduce the external field (microwave and laser) to interact with the internal state and motional state of the ion. The magnetic field (microwave) can realize the hyperfine ststes transition, and the electric field (laser) can realize the transition between ^{2}S$_{1/2}$ and ^{2}P$_{1/2}$. Our clock qubit, $|\uparrow\rangle$ and $|\downarrow\rangle$, is a two level system, and the Hamiltonian of this two level system can be written as

$$H^{(e)} \equiv \hbar \frac{\omega_{HF}}{2}\sigma_z \qquad (3\text{-}3)$$

where σ_Z is the Pauli spin matrix.

In the quantum mechanical treatment for the motion of the harmonic oscillator, the Hamiltonian of motional modes can be written as

$$H^{(m)} \equiv \hbar\omega_X(a^\dagger a + \frac{1}{2}) \qquad (3\text{-}4)$$

where we take the motional mode X as an example, other motional modes can be described similarly. $a^\dagger$ and a are the creation and annihilation operators for the phonons in the harmonic oscillator.

When the external magnetic field or electric field is applied, the interaction Hamiltonian can be written as

$$H^{(i)} = \frac{\hbar}{2}\Omega(|\downarrow\rangle\langle\uparrow| + |\uparrow\rangle\langle\downarrow|) \times \left[e^{i(kx-\omega t+\phi)} + e^{-i(kx-\omega t+\phi)}\right] \qquad (3\text{-}5)$$

where ω is the frequency of the applied external field, k is the wave vector, ϕ is the phase of the external field, the Rabi frequency Ω is $-\mu_m B_X/2\hbar$ for the microwave and $-\mu_d E_X/2\hbar$ for the laser, $|\uparrow\rangle\langle\downarrow| \mapsto \sigma_+ = 1/2(\sigma_x + i\sigma_y)$ and $|\downarrow\rangle\langle\uparrow| \mapsto \sigma_- = 1/2(\sigma_x - i\sigma_y)$.

The total Hamiltonian of our system is $\hat{H} = H^{(m)} + H^{(e)} + H^{(i)}$. The unperturbed Hamiltonian $H_0 = H^{(e)} + H^{(m)}$, and the evolution Hamiltonian is $U_0 = exp\{-(i/\hbar)H_0 t\}$.

Then the interaction picture Hamiltonian is

$$
\begin{aligned}
H_I &= U_0^\dagger H^{(i)} U_0 \\
&= e^{(i/\hbar)H_0 t} \frac{\hbar}{2} \Omega(|\downarrow\rangle\langle\uparrow| + |\uparrow\rangle\langle\downarrow|) \times \left[e^{i(kx-\omega t+\phi)} + e^{-i(kx-\omega t+\phi)} \right] e^{-(i/\hbar)H_0 t} \\
&= \frac{\hbar}{2} \Omega\, e^{(i/\hbar)H^{(e)}t} (\sigma_+ + \sigma_-) e^{-(i/\hbar)H^{(e)}t} \times e^{(i/\hbar)H^{(m)}t} \left[e^{i(kx-\omega t+\phi)} + e^{-i(kx-\omega t+\phi)} \right] e^{-(i/\hbar)H^{(m)}t} \\
&= \frac{\hbar}{2} \Omega\, e^{i\omega_{\mathrm{HF}}\sigma_z t/2} (\sigma_+ + \sigma_-) e^{-i\omega_{\mathrm{HF}}\sigma_z t/2} \times e^{i\omega_X a^\dagger a t} \left[e^{i(kx-\omega t+\phi)} + e^{-i(kx-\omega t+\phi)} \right] e^{-i\omega_X a^\dagger a t} \\
&= \frac{\hbar}{2} \Omega\, (\sigma_+ e^{i\omega_{\mathrm{HF}}t} + \sigma_- e^{-i\omega_{\mathrm{HF}}t}) \times e^{i\omega_X a^\dagger a t} \left[e^{i(kx-\omega t+\phi)} + e^{-i(kx-\omega t+\phi)} \right] e^{-i\omega_X a^\dagger a t} \\
&= \frac{\hbar}{2} \Omega\, (\sigma_+ e^{i\omega_{\mathrm{HF}}t} + \sigma_- e^{-i\omega_{\mathrm{HF}}t}) \times \left(e^{i[\eta(a^\dagger e^{i\omega_X t}+ae^{-i\omega_X t})-\omega t+\phi]} + e^{-i[\eta(a^\dagger e^{i\omega_X t}+ae^{-i\omega_X t})-\omega t+\phi]} \right) \\
&= \frac{\hbar\Omega}{2} (\sigma_+ e^{i[(\omega_{\mathrm{HF}}-\omega)t+\phi]} e^{i\eta(a^\dagger e^{i\omega_X t}+ae^{-i\omega_X t})} + \sigma_- e^{-i[(\omega_{\mathrm{HF}}-\omega)t+\phi]} e^{-i\eta(a^\dagger e^{i\omega_X t}+ae^{-i\omega_X t})})
\end{aligned}
$$

$$(3\text{-}6)$$

where $\eta = kx_0$ is the Lamb-Dicke parameter.

When we only consider the transition between $|\downarrow, n_1\rangle$ and $|\uparrow, n_2\rangle$, the Rabi frequency has a relation with the Debye-Waller factor[24]

$$
\Omega_{n_1,n_2} = \Omega |\langle n_1| e^{i\eta(a+a^\dagger)} |n_2\rangle| = \Omega e^{-\eta^2/2} \sqrt{\frac{n_<!}{n_>!}} \eta^{|n_1-n_2|} L_{n_<}^{|n_1-n_2|}(\eta^2) = D_{n_1,n_2}\Omega \qquad (3\text{-}7)
$$

where $L_n^\alpha(x)$ is the generalized Laguerre polynomial, $n_<$ ($n_>$) is the smaller (bigger) one of n_1 and n_2.

In the Lamb-Dicke region, where the position spread of the ion is much smaller than the wavelength of the external field, i.e., $\eta n^2 \ll 1$, we have $\Omega_{n,n} = \Omega$, $\Omega_{n,n-1} = \sqrt{n}\eta\Omega$ and $\Omega_{n,n+1} = \sqrt{n+1}\eta\Omega$. However, if η is too small, close to zero, the transition strength of $\Omega_{n,n+1}$ and $\Omega_{n,n-1}$ are negligible.

3.3.2　Microwave operations

For the situation of microwave induced transitions, the Lamb-Dicke parameter $\eta = kx_0 = \frac{2\pi}{\lambda}\sqrt{\frac{\hbar}{2m_{\mathrm{Yb}}\omega_M}}$, and we assume the motional trap frequency is $\omega_M = (2\pi)2$ MHz, $\lambda = 3\times10^8/(12.64\times10^9)$ m, $\hbar = 1.054\times10^{-34}$ m^{2}kg/s and $m_{\mathrm{Yb}} = 171\times1.998\times10^{-26}/12$ kg. The calculated $\eta = 1.02\times10^{-6}$, which is a number close to zero. Therefore, for the transitions that change the phonon number from n_1 to n_2 ($n_1 \neq n_2$), the Rabi frequency is almost zero, which means the microwave can not excite any phonon.

In our microwave system setup, shown in Figure 3.6 (a), the signal comes from the mix of the standard RF source (we set the frequency at 12.462812118 GHz) and an Arbitrary-Waveform-Generator (AWG, can generate the waveform ranging from 150 to 250 MHz), where both signal sources are Rb atomic clock referenced. The AWG can provide the waveform as we designed, and thus we can change the amplitude, duration, and phase of the applied microwave field. After the mixer, the signal passes through a microwave amplifier, which is a customized amplifier (from bonn-elektronik) with high gain and narrow band-pass. The microwave power to the horn is around 10 W, and the horn antenna generates the wave propagating to the ion.

In the experiment, the microwave horn is mounted on a three-dimensional transition stage to change the position of the microwave horn, and another rotating stage is installed to change the angle between the antenna and the magnetic field generated by the Helmholtz coil. We carefully adjust the horn to achieve the maximum interacting strength between the ion and microwave. In Figure 3.6 (b) and (c), we show the experimental data on the transition between $|\downarrow\rangle$ and $|\uparrow\rangle$, with the fitting of the experimental data, our driving frequency of the clock qubit setting in the AWG is 180.01 MHz, and the π-time of the Rabi flipping between $|\downarrow\rangle$ and $|\uparrow\rangle$ is 11.39 μs.

Here, I want to mention the weak points of using microwave to implement operations: First, the strength of the magnetic dipole transition (between $|\downarrow\rangle$ and $|\uparrow\rangle$) is much weaker than the electric dipole transition (between ^{2}S$_{1/2}$ and ^{2}P$_{1/2}$), which limits the microwave for generating a fast gate. Second, the output of the microwave from the horn is a global operation to all the ions. Thus it is difficult to implement the individual addressing to the ions with the microwave.

3.3.3　Raman laser operations

For the situation of the counter-propagating Raman laser beams, with the induced transition between ^{2}S$_{1/2}$ and ^{2}P$_{1/2}$, and the laser wavelength 375 nm, the calculated η is 0.13 for a $(2\pi)2$ MHz trap frequency, which is much larger than the microwave.

In Figure 3.7, we experimentally measured the η of X mode. We prepare the ion in different number states: from $|\downarrow, n = 0\rangle$ to $|\downarrow, n = 10\rangle$, and then apply a resonant blue sideband laser to measure the Rabi frequency of the oscillation. Since the measured Rabi frequency for the different number state Ω_n has a relationship with the ground state Ω_0: $\Omega_n = \Omega_0 L_n^1(\eta^2)/\sqrt{n+1}$, we fit our experimental data and obtained that the η is 0.14,
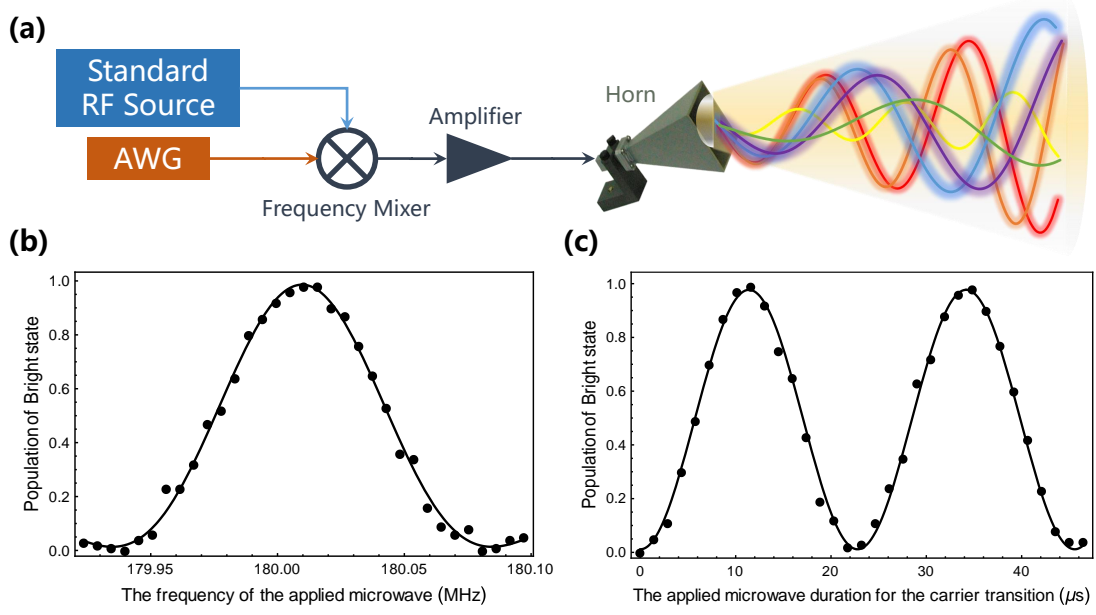
图 3.6　Microwave system and the transition between $|\downarrow\rangle$ and $|\uparrow\rangle$ induced by microwave. (a) A schematic diagram of the microwave system setup. A standard RF source is mixed with the AWG to generate the signal that controls the qubit. To realize a reasonable gate time via microwave, we need to use an amplifier to generate about 10 Watt microwave and send it to the horn. (b) and (c) The state of the ion is initialized at $|\downarrow\rangle$, and then we apply the microwave and detect the fluorescence count of the ion. (b) We scan the frequency of the microwave (controlled by the AWG) with a certain duration and find the resonant frequency for this transition via fitting the experimental data. (c) We apply the microwave with the resonant frequency and change the duration. We obtain the Rabi frequency of the transition via fitting the experimental data. In the figure, the dots are experimental data, and the solid curves are the fitting results.

where we use the trap frequency $(2\pi)1.8$ MHz. The experimentally fitting result has a difference with the theoretical calculated value 0.136, and the difference mainly comes from the non-perfect preparation of the number state.

With the Lamb-Dicke approximation, and following the Eq. (3-6), we do the Taylor series expansion with the first order truncation, we have

$$
\begin{aligned}
H_I &= \frac{\hbar\Omega}{2}(\sigma_+ e^{i[(\omega_{\text{HF}}-\omega)t+\phi]} e^{i\eta(a^\dagger e^{i\omega_X t}+ae^{-i\omega_X t})} + \sigma_- e^{-i[(\omega_{\text{HF}}-\omega)t+\phi]} e^{-i\eta(a^\dagger e^{i\omega_X t}+ae^{-i\omega_X t})}) \\
&\simeq \frac{\hbar\Omega}{2}[\sigma_+ e^{i[(\omega_{\text{HF}}-\omega)t+\phi]} + \sigma_- e^{-i[(\omega_{\text{HF}}-\omega)t+\phi]}] \\
&+ \frac{\hbar\Omega i\eta}{2}[\sigma_+ a^\dagger e^{i[(\omega_{\text{HF}}-\omega+\omega_X)t+\phi]} - \sigma_- a e^{-i[(\omega_{\text{HF}}-\omega+\omega_X)t+\phi]}] \\
&+ \frac{\hbar\Omega i\eta}{2}[\sigma_+ a e^{i[(\omega_{\text{HF}}-\omega-\omega_X)t+\phi]} - \sigma_- a^\dagger e^{-i[(\omega_{\text{HF}}-\omega-\omega_X)t+\phi]}]
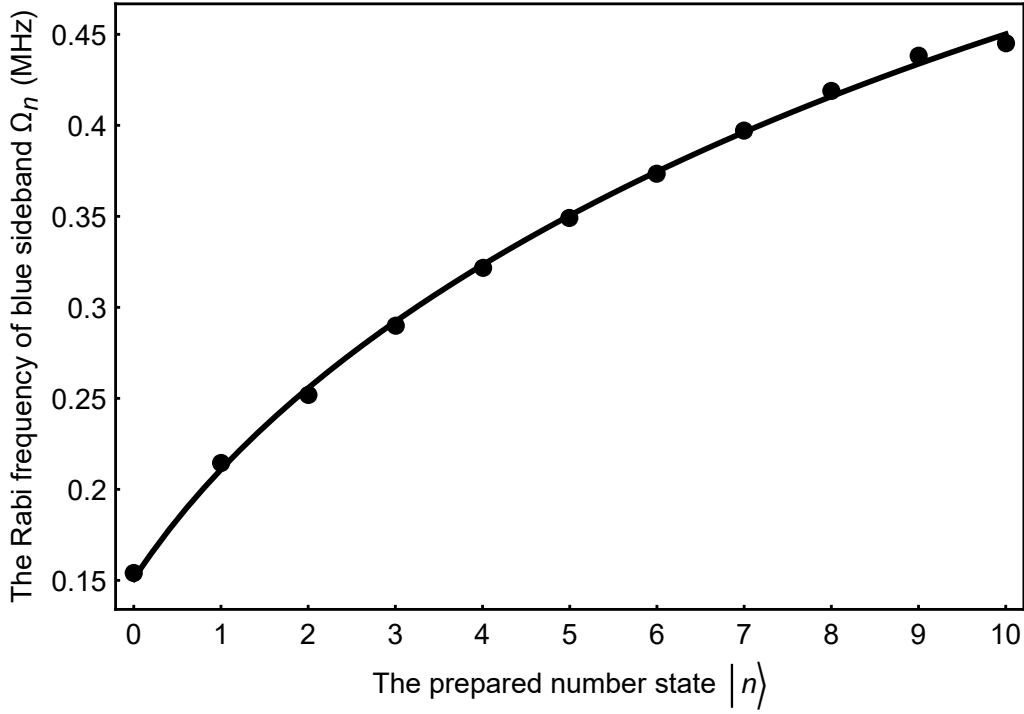\end{aligned}
\tag{3-8}
$$

图 3.7　Experimental measurement of the Lamb-Dicke parameter. We experimentally prepare the number state on X mode after sideband cooling. The trap frequency for this measurement is $\omega_X = (2\pi)1.8$ MHz. After preparing the number state, we apply the resonant blue sideband laser, and from the Rabi oscillation signal, we obtain the corresponding Rabi frequency. By fitting the experimental data points of Rabi frequencies with the Laguerre polynomial, we obtain η as 0.14. In the figure, the dots are experimental data, and the solid curve is the fitting result.

When the frequency of the external Raman laser field is set as $\omega = \omega_{HF}$, $\omega = \omega_{HF} + \omega_X$ and $\omega = \omega_{HF} - \omega_X$, we can realize carrier transition, blue sideband transition and red sideband transition, respectively.

Figure 3.8 shows our typical experiment configuration of the Raman laser. We use the counter-propagating 375 nm pulsed laser beam to hit the ion, where both laser beams are σ^+ polarized. The magnetic field generated by the Helmholtz coil is aligned along the laser propagating direction. Based on the setting of the Raman 1 and Raman 2 (frequency, duration, and phase), we can realize the internal state qubit operation, and manipulate the phonon degree of freedom. The idea of using the Raman laser is called stimulated Raman transitions, which is a two-photon process. As shown in Figure 3.8, Raman 1 transits the state from $|\downarrow\rangle$ to a virtual energy level that is detuned from $^2P_{1/2}$ of about 10.8 THz. Then, Raman 2 brings the state from the virtual energy level back to $|\uparrow\rangle$. In this process, an effective transition from $|\downarrow\rangle$ to $|\uparrow\rangle$ is realized.

We assume the electric field of two Raman lasers are $E_1(\text{x}) = \text{E}_1 \cos(k_1 X - \omega_1 \text{t} - \phi_1)$
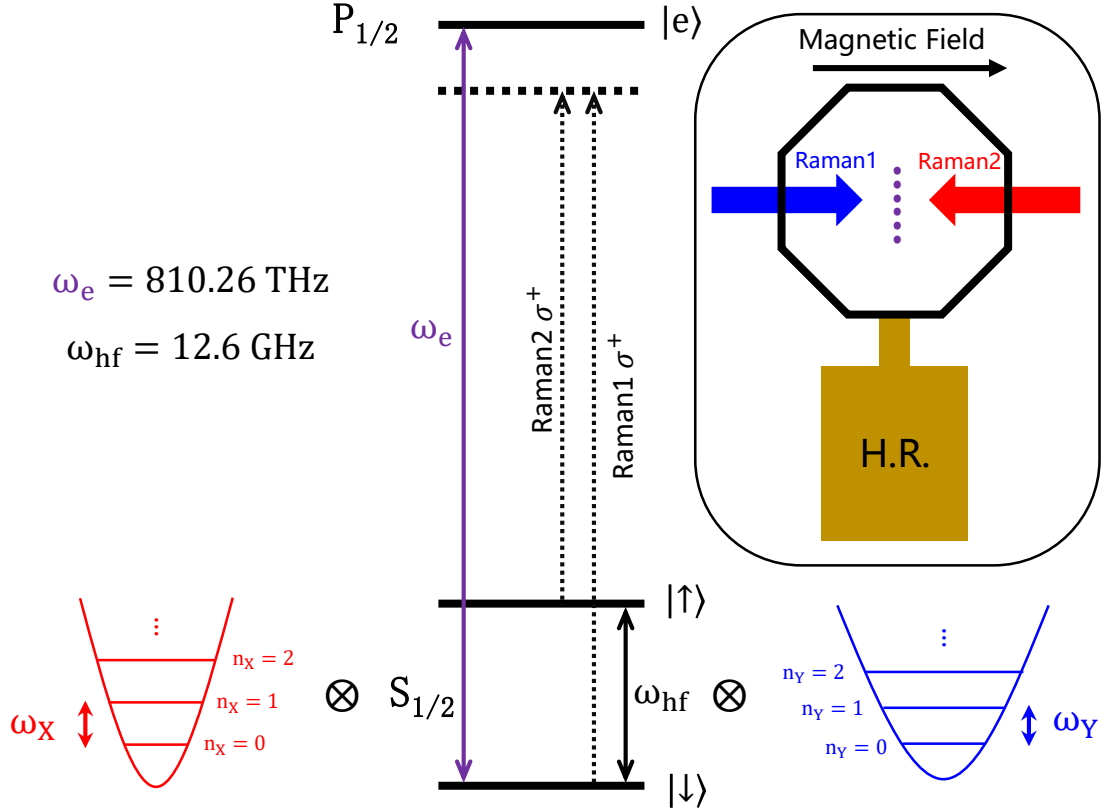
图 3.8 Energy level diagram of ^{171}Yb$^+$ with two motional modes and basic Raman transitions. The electronic levels ($|\uparrow\rangle, |\downarrow\rangle$) with the difference ω_{hf}, and the phonon levels of modes X and Y with the frequencies of ω_X and ω_Y are involved in the Raman process. By controlling the frequency difference of Raman1 and Raman2, we can implement single mode and two modes quantum operations. The inset shows the laser propagating direction in the experiment.

and $\boldsymbol{E}_2(\text{x}) = \text{E}_2 \cos(\boldsymbol{k_2 X} - \omega_2 \text{t} - \phi_2)$, Δ is the detuning from the virtual energy level to $|e\rangle$, and $\omega_1 - \omega_2 = \omega_{\text{HF}} + \delta\omega$. The interaction Hamiltonian of these two counter-propagating laser beams with the ion is

$$H_I = \frac{\hbar g_1}{2}(e^{i(\boldsymbol{k_1 X}+\phi_1)}e^{-i(\omega_{\text{HF}}+\delta\omega)}|e\rangle\langle\downarrow| + h.c.) + \frac{\hbar g_2}{2}(e^{i(\boldsymbol{k_2 X}+\phi_2)}|e\rangle\langle\uparrow| + h.c.) + \frac{\hbar\Delta}{2}|e\rangle\langle e|$$

(3-9)

where g_1 and g_2 are govered by the electric dipole coupling strength.

Under the situation of $\Delta \gg \gamma$, which states the spontaneous emission induced by the laser is negligible[25], and by applying the rotating wave approximation (RWA), we have the carrier transition, blue sideband transition and red sideband transition, when $\delta\omega = 0$,

$\delta\omega = \omega_X$ and $\delta\omega = -\omega_X$, respectively:

$$H_{car} = \frac{\hbar\Omega}{2}\left(\sigma_+ e^{i\Delta\phi} + \sigma_- e^{-i\Delta\phi}\right)$$

$$H_{bsb} = \frac{\hbar\Omega\eta}{2}\left(\sigma_+ a^\dagger e^{i\Delta\phi} + \sigma_- a e^{-i\Delta\phi}\right)$$

$$H_{rsb} = \frac{\hbar\Omega\eta}{2}\left(\sigma_+ a e^{i\Delta\phi} + \sigma_- a^\dagger e^{-i\Delta\phi}\right) \tag{3-10}$$

where $\eta = \Delta k X$, $\Delta k = k_1 - k_2$ is the difference of the wave vector, and $\Delta\phi = \phi_1 - \phi_2$ is the phase difference of the laser felt by the ion.

The Raman laser we are using is the mode-locked laser from the Coherent company (model: Mira-HP). The picosecond pulsed laser can generate a broadband optical frequency comb, which is essential for our control of state transitions. Our pulsed laser is generated by sending a high power pump laser (continuous-wave 532 nm laser, about 14 Watt) to an optical cavity, where the Ti:Sapphire crystal inside the cavity generates a red beam (we typically set the center wavelength of this red beam at 750 nm, the red laser is frequency doubled to 375 nm for the experimental usage). The length of the cavity decides the repetition frequency of the laser (around $(2\pi)76$ MHz). The electric field of a mode-locked laser can be described as

$$E(t) = E_n \sum_{-(N-1)/2}^{(N-1)/2} \exp\{(\omega_0 + n\omega_{\text{rep}})t + i\phi_n(t)\} \tag{3-11}$$

where E_n is the intensity of the n-th mode, ω_0 is the center frequency of the laser, ω_{rep} is the repetition frequency of the laser, and ϕ_n is the phase of the n-th mode.

We use two AOMs to switch the laser beam of Raman1 and Raman2, so that the output laser frequency from the AOMs are $n_1\omega_{\text{rep}} + \omega_{AOM1}$ and $n_2\omega_{\text{rep}} + \omega_{AOM2}$, where n_1 and n_2 are the order index of the optical frequency comb, as shown in Figure 3.9 (a). The order index of the optical frequency comb vary from 0 to infinity. In the experiment, we stabilize the repetition frequency of the picosecond pulsed laser to $(2\pi)76.047061$ MHz (see section 4.3.2 for the technique details). For the carrier transition, we set the frequency of AOM1 as $\omega_{AOM1} = (2\pi)250$ MHz, and AOM2 as $\omega_{AOM2} = (2\pi)231$ MHz, and with a 166 orders frequency combs difference, the generated frequency difference in Raman 1 and Raman 2 is $(n_1 - n_2)\omega_{\text{rep}} + \omega_{AOM1} - \omega_{AOM2} = (2\pi)(166 \times 76.047061 + (250 - 231))$ MHz $= (2\pi)12.642812118$ GHz $= \omega_{\text{HF}}$. For blue sideband transition and red sidebnad transition, we change the input frequency of AOM1 as $\omega_{AOM1} = (2\pi)(250 + \omega_M)$ MHz and $\omega_{AOM1} =$
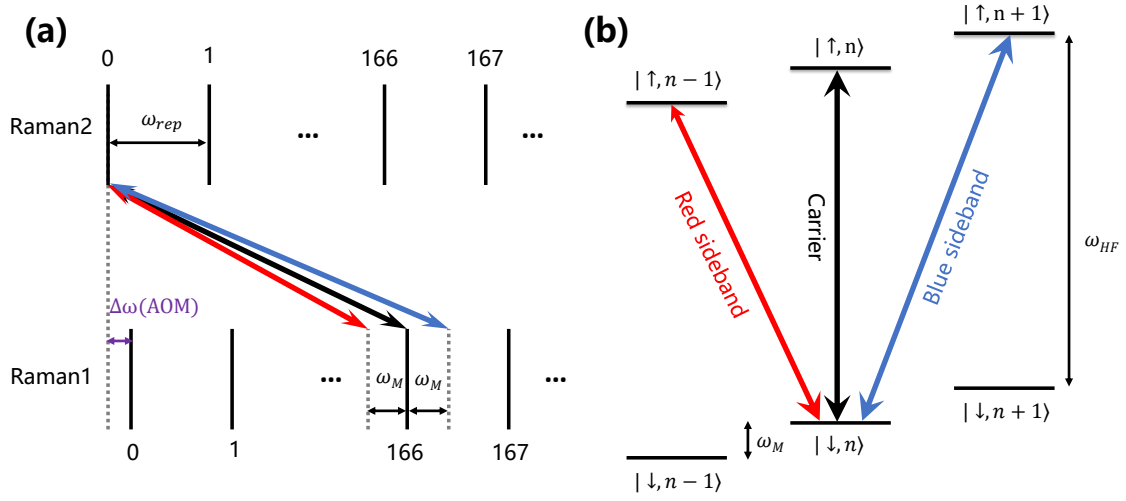
图 3.9　Schematic diagram of the Raman laser-induced transition based on the optical frequency comb. (a) We use the driving frequency of AOM1 and AOM2 to shift the optical frequency comb, and the frequency difference between Raman 1 and Raman 2 can generate the carrier, blue sideband and red sideband transition, respectively. In the experiment, We stabilize the repetition frequency of the Raman laser and realize these operations via changing the frequency difference $\Delta\omega$(AOM) between the drive frequency of AOM1 and AOM2. (b) The carrier flips the spin in the hyperfine energy levels between $|\downarrow\rangle$ and $|\uparrow\rangle$. The blue sideband transits the state between $|\downarrow, n\rangle$ and $|\uparrow, n-1\rangle$. The red sideband transits the state between $|\downarrow, n\rangle$ and $|\uparrow, n+1\rangle$. In the figure, ω_M is the trap frequency of the motional modes, and $\omega_{\text{HF}} = 12.642812118466$ GHz.

$(2\pi)(250 - \omega_M)$ MHz, where ω_M is the trap frequency of the motional mode.

　　Figure 3.10 shows our experimentally measured data of the drive frequency and the Rabi frequency of the carrier, blue sideband and red sideband transitions. The applied transitions are controlled by the AWG, which can generate a frequency, duration and phase controlled signal. The generated signal is sent to AOM1, and the Raman 1 laser is modulated as the input signal of AOM1. When we scan the drive frequency of the transition, we fix the duration of the applied laser and vary the frequency in AWG. When we scan the Rabi frequency of the transition, we fix the applied laser frequency with the resonant one and vary the applied duration. For the carrier and blue sideband transitions, we initialize the state of the ion to $|\downarrow, 0\rangle$, and then apply the corresponding operation laser to the ion. For the red sideband transition, we initialize the ion to state $|\uparrow, 0\rangle$ and then applied the red sideband transition laser to the ion.

　　By calculating the drive frequency difference of carrier and blue sideband, we obtain the trap frequency $\omega_M = 2.23$ MHz. This is slightly different from the result of calculating the difference between the carrier and red sideband (2.22 MHz). I think the main reason
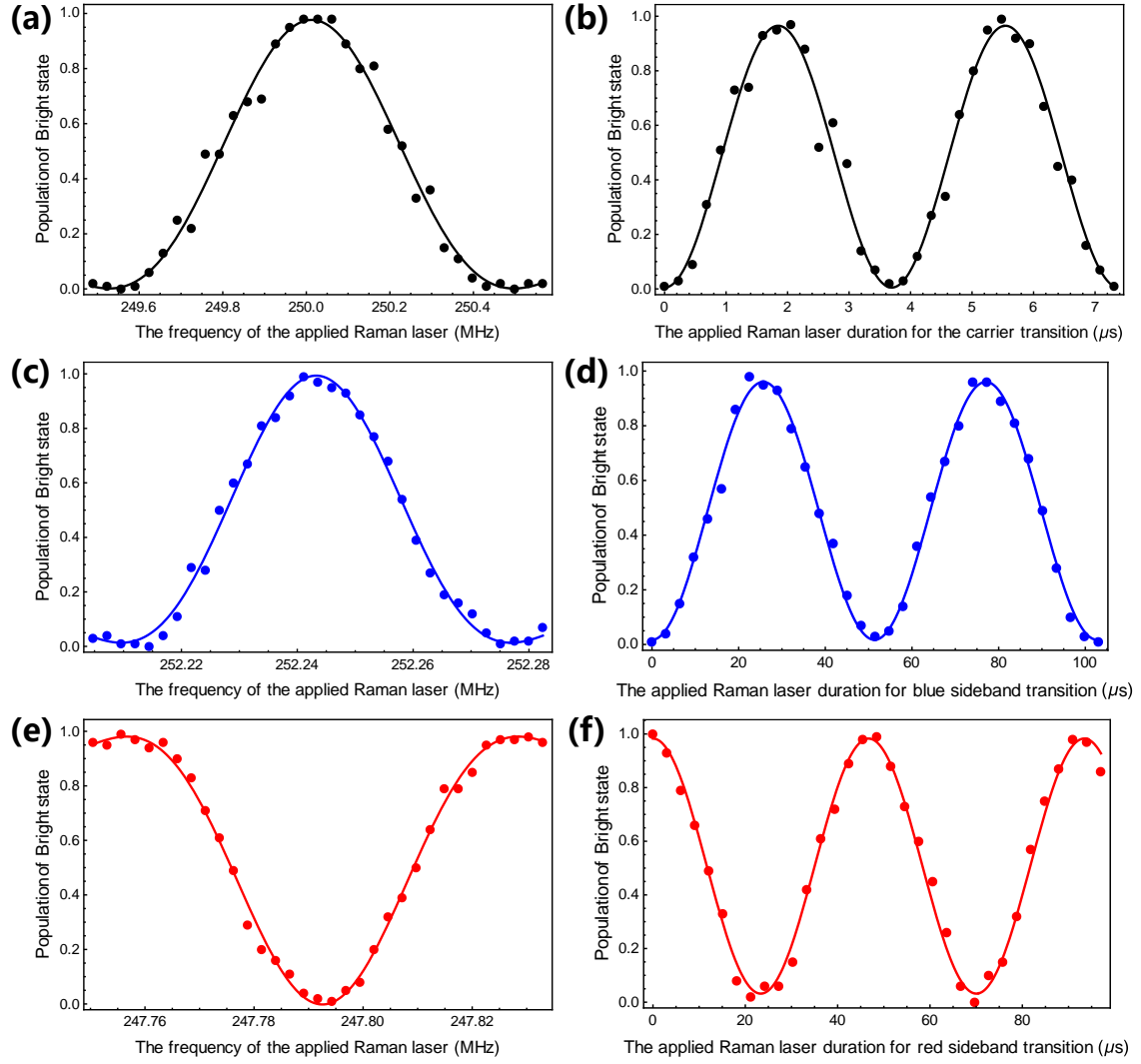
图 3.10 The experimentally measured data of carrier, blue sideband and red sideband transitions. (a) and (b) The experimental data for the frequency scan and duration scan of the carrier transition. By fitting the experimental data, the drive frequency is 250.013 MHz, and the Rabi frequency is (2π) 0.27 MHz. (c) and (d) The experimental data for the frequency scan and duration scan of the blue sideband transition. By fitting the experimental data, the drive frequency is 252.243 MHz, and the Rabi frequency is (2π) 0.019 MHz. (e) and (f) The experimental data for the frequency scan and duration scan of the blue sideband transition. By fitting the experimental data, the drive frequency is 247.793 MHz, and the Rabi frequency is (2π) 0.021 MHz.

for this difference is the accuracy of the data fitting and the intensity difference of blue sideband and red sideband that makes different A.C. stark shift. We also notice a slight Rabi frequency difference of the blue sideband and red sideband transition, and the reason is the different response behaviors of different frequencies in AWG and AOM, which results in the power difference felt by the ion. The big Rabi frequency difference between red (blue) sideband and carrier transition is the effect of Lamb-Dicke parameter.

I want to mention that the above operations (carrier, blue sideband and red sideband) are the essential parts of our trapped ion system when dealing with phonon degree of freedom. However, within the Raman laser beam, we can implement additional quantum operations, which offers us a complete toolbox to explore the quantum phenomenon with phonons. See section 6.3 for the spin-dependent operations and spin-independent operations.

3.4　Quantum state detection

In a quantum system, the results of any quantum computation need to be efficiently and faithfully measured. In this section, I will introduce qubit measurement in our trapped ion system with a single ion and multi-ions.

State detection in a trapped ion system is done by the standard fluorescence techniques, which shines a laser beam that is resonant with a cycling transition to the ion. Typically, this transition is resonant for one of the qubit states, but off-resonant for the other. In this sense, we can distinguish a "Bright" state and a "Dark" state[26–28]. When the cycling transition happens, the ion scatters out several photons out to space with a particular duration, and we use an objective lens to collect a fraction of photons and transfer these photons to either the photo-multiplier tube (PMT) or Electron-Multiplying charge-coupled device (EMCCD) to count the number of photons. The PMT holds a better signal to noise ratio, which results in a higher fidelity for the state detection. However, when the PMT receives a photon, the PMT cannot tell which ion scattered the photon due to the loss of spatial information. One may propose to use a strictly focused tiny detection laser beam to hit one ion each time and collect the corresponding signal, but the drawback of this scheme is the enormous amount of detection time as the number of ions increase. Instead, the Camera (EMCCD) can make up for this problem and becomes a good candidate for multi-ions detection.

In this section, I will discuss the theoretical detection model for the ^{171}Yb$^+$ ion and show how to distinguish between the "Bright" state and "Dark" state. Then, I will describe the imaging system used in our setup. After that, I will present the experimental results for the PMT and Camera. Finally, I will implement the state-detection-error correction scheme to our experimental raw data.

3.4.1　Theory of detection process

The detection of the ^{171}Yb$^+$ ion is done by shining a laser that is used to distinguish the state of $|F = 1\rangle$ (Bright state) and $|F = 0\rangle$ (Dark state) in $^2S_{1/2}$ manifold, which are separated by 12.643 GHz. This detection laser beam is resonant between $^2S_{1/2}\,|F = 1\rangle$ and $^2P_{1/2}\,|F = 0\rangle$, as shown in Fig. 3.11. The applied laser beam contains π, σ^+ and σ^- polarizations, and thus, the state of $^2S_{1/2}\,|F = 1, M_F = 0\rangle$, $^2S_{1/2}\,|F = 1, M_F = -1\rangle$ and $^2S_{1/2}\,|F = 1, M_F = 1\rangle$ can all be excited. Although the Zeeman splitting in $^2S_{1/2}\,|F = 1\rangle$ is $(1.4\,\text{MHz/G}) \times \text{B}$ (where B is the strength of magnetic field at the ion's location, and the Zeeman spiltting is typically around 10 MHz in our setup), the natural linewidth of $^2P_{1/2}\,|F = 0\rangle$ is $\gamma/2\pi = 19.7$ MHz, which gives the chance of $^2S_{1/2}\,|F = 1, M_F = -1\rangle$ and $^2S_{1/2}\,|F = 1, M_F = 1\rangle$ resonant with state $^2P_{1/2}\,|F = 0\rangle$ under the detection laser beam. In short, when the ion is in the Bright state, it will scatter out large number of photons under the cycling transition; when the ion is in the Dark state, since it is far off-resonant with the allowed transition, there will be no photons scattered out.
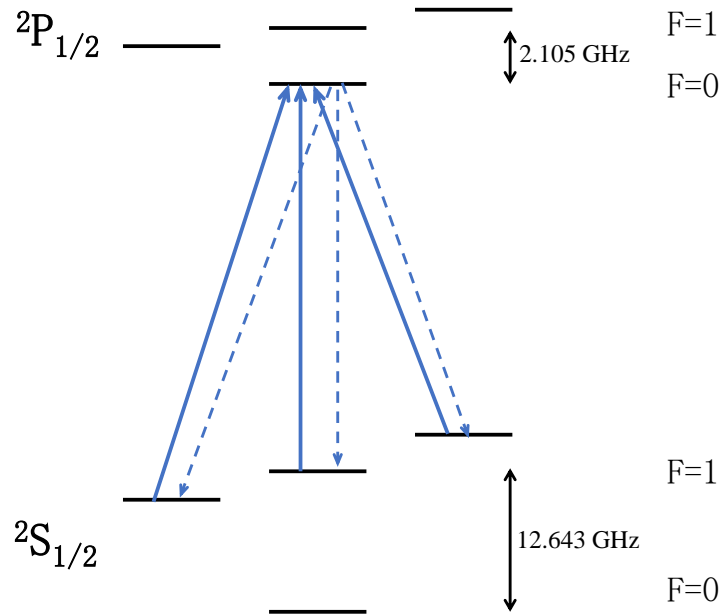
图 3.11　The detection transition. The detection laser beam is resonant between $^2S_{1/2}\,|F = 1\rangle$ and $^2P_{1/2}\,|F = 0\rangle$. Typically the laser beam contains equal π, σ^+ and σ^- polarization components. The solid blue lines are laser drive transitions, and the dashed lines are spontaneous emission decay transitions.

Another important point to mention is the asymmetric detection efficiency of the Bright state and Dark state. Due to the selection rule, the transition between $^2S_{1/2}\,|F = 0\rangle$

and ^{2}P$_{1/2}$ |F = 0⟩ is forbidden, thus the Dark state can only be resonant with the state ^{2}P$_{1/2}$ |F = 1⟩. As shown in Figure 3.11, for the Bright state to Dark state transition, it is 2.105 GHz off-resonant to the detection beam. For the Dark state to Bright state transition, it is 14.748 (=2.105+12.643) GHz off-resonant. Therefore, the Dark state holds a better detection efficiency than the Bright state for ^{171}Yb$^+$.

In an ideal atomic system, the distribution of collected photons from the ion's fluorescence obey the Poisson statistics. Typically, we run our experiment with certain repeats, with a given detection time and laser power, so that we can collect a mean number of photons, λ. The probability distribution of collected photons under the Poisson distribution is

$$P(n) = \frac{e^{-\lambda}\lambda^n}{n!} \tag{3-12}$$

where n is the number of photons.

The numerical simulation of the Poisson distribution is shown in Figure 3.12 (a), where we assume one ion scatters photons with a mean number $\lambda = 10$, and three ions scatter a mean number of 30 photons. As we can see in the figure, when the number of ions increases, the distribution becomes more extensive and becomes harder to distinguish the distribution between n ions and n+1 ions. This indicates that we cannot use PMT to detect a large number of ions with high fidelity.

In a real atomic system, the off-resonant coupling between the Bright state and Dark state happens with a non-negligible probability. The rate equations which describe this coupling has an exponential probability distribution. Therefore, the distribution of the photons scattered from the ion is a convolution of a Poisson and exponential[29,30]. With some theory investigation, followed by ref. [30], we define τ_D as the detection time and λ_0 as the mean collected photons number when the ion is in the Bright state. The Dark state distribution $P_{Dark}(n)$ and Bright state distribution $P_{Bright}(n)$ are:

$$P_{Dark}(n) = e^{-\alpha_1\lambda_0/\eta}\left[\delta_n + \frac{\alpha_1/\eta}{(1-\alpha_1/\eta)^{n+1}}\Gamma(n+1, (1-\alpha_1/\eta)\lambda_0)\right] \tag{3-13}$$

$$P_{Bright}(n) = \frac{e^{-(1+\alpha_2/\eta)\lambda_0}}{n!} + \frac{\alpha_2/\eta}{(1+\alpha_2/\eta)^{n+1}}\Gamma(n+1, (1+\alpha_2/\eta)\lambda_0) \tag{3-14}$$

where $\Gamma(n, x) \equiv \frac{1}{(n-1)!} \int_0^x e^{-t} t^{n-1} dt$. $\eta = \eta_D \frac{d\Omega}{4\pi} T$ is the total photon collection efficiency with the factors of detector efficiency (η_D), imaging system solid angle ($\frac{d\Omega}{4\pi}$) and optical transmission (T). $\alpha_1 \equiv \frac{\tau_D \eta}{\tau_{L1} \lambda_0}$ is the Dark state to Bright state leak probability per emitted photon with the average leak time τ_{L1}, and $\alpha_2 \equiv \frac{\tau_D \eta}{\tau_{L2} \lambda_0}$ is the Bright state to Dark state leak probability per emitted photon with the average leak time τ_{L2}.

Typically, we have the detector (PMT or Camera) with a quantum efficiency around $\eta_D = 30\%$ at our photon wavelength 369.5 nm. The solid angle $d\Omega/4\pi = \int_0^\theta 2\pi (R \sin \phi) R d\phi / (4\pi R^2) = (1 - \cos \theta)/2$, where $\sin \theta$ is the numeric aperture (N.A.) size of the objective lens. We estimate the optical transmission from the ion to detector as $T = 80\%$ (consider the photon loss cost by window, optical fiters and other optics). The leak probability for our ^{171}Yb$^+$ ion are $\alpha_1 = 2.04 \times 10^{-7}$ and $\alpha_2 = 1.00 \times 10^{-5}$.
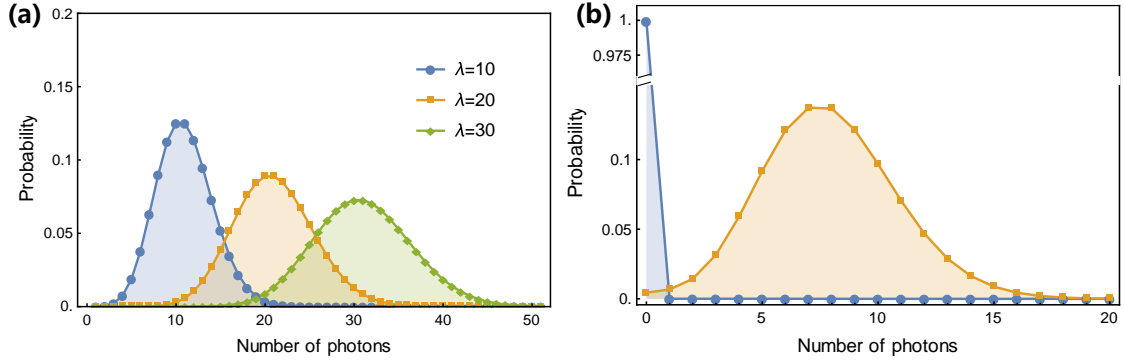
图 3.12　Numerical simulation for the distribution of the collected photons in trapped ion system. (a) In an ideal situation, the distribution of collected photons obeys the Poisson distribution. (b) The off-resonant coupling is considered for the detection transition, which results in the state leakage between Bright state and Dark state. Here, we numerically show the detection result for a well prepared Dark state and Bright state, and we assume the mean photon number $\lambda_0 = 8$ when the ion is bright. The blue and orange curves represent the photon distribution of the Dark state and Bright state, respectively.

Based on Eq. (3-13) and Eq. (3-14), we plot the collected photon distribution of the Dark state and Bright state in Figure 3.12 (b). In the numerical simulation, we used the parameters of our objective lens in the lab, a CVI Laser Optics (Model: UVO-20.0-10.0-355-532) with N.A.=0.2. We set the threshold to $n = 1$ to identify photon number $n \leq 1$ as Dark state, and $n > 1$ as Bright state in our experiment. The numerical calculation result shows that the Dark state calculate fidelity is 99.95%, and the Bright state is 98.89%.

3.4.2 Detection imaging system

图 3.13　Schematic diagram of the ion's fluorescence detection system.

The detection imaging system for the detection of an ion's fluorescence is shown in Figure 3.13. The whole detection imaging system consists of two stages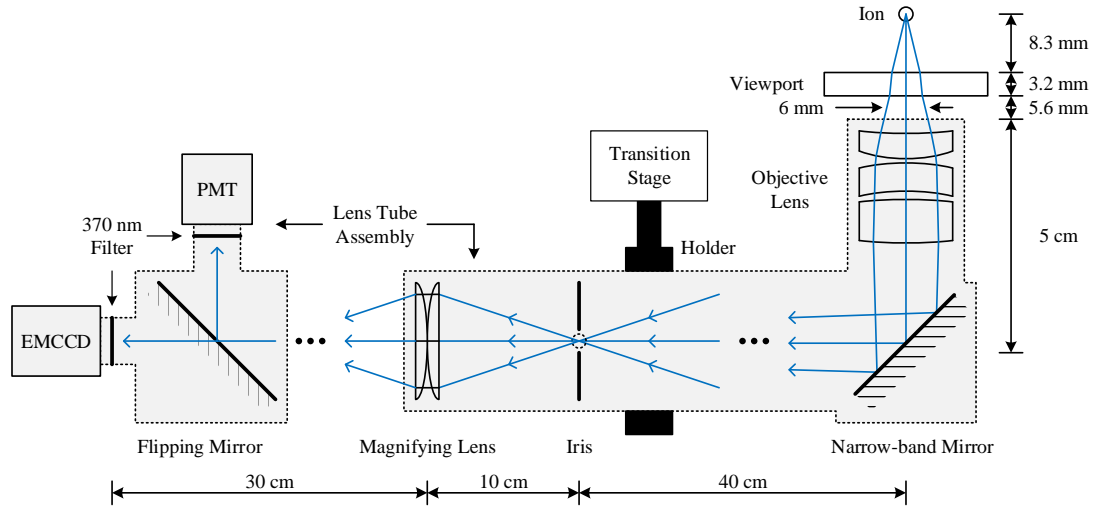: (a) The objective lens is used to collect the photons that the ion scatters out, and the ion is imaged at the Iris position, where the Iris is used to block noisy photons. (b) The second stage consists of the magnifying lens that magnifies the image of the ion to a more prominent size, and we use a flip mirror to select the collecting photon device, PMT or EMCCD. In the optical path of photons transferring to photon counting device, we install an optical filter to increase the signal to noise ratio (SNR) via filtering out the unwanted photons.

The camera (EMCCD) installed in the setup is essential for the quantum measurement of multi-ions. Furthermore, the camera plays a vital role when we first align our imaging system, and it is useful in the ion loading stage.

3.4.3 Detection with a PMT

Since the PMT can not resolve the spatial information of the ion chain, therefore we only use the PMT (Hamamatsu company, model: H10682-210) to collect the fluorescence counts from a single ^{171}Yb$^+$ ion, and distinguish the Bright state and Dark state. We use the FPGA board to count the number of TTLs generated by the PMT, where the number of TTLs is same as the number of the incident photons to the PMT. The first step of optimizing our detection imaging system is making sure that the ion can show a clear

image on the camera, and that the PMT can collect all the photons transferred by the optics. After that, we carefully optimize the size of the Iris (in front of the PMT) to block noisy photons.

The remaining part of the experiment in our PMT detection is setting the detection duration. In Figure 3.14 (a), we vary the duration of the applied detection laser beam, and record the collected photon counts for the Bright state $|\uparrow\rangle$ and Dark state $|\downarrow\rangle$. In a short duration region (less than 1000 μs), the collected photon count increases linearly for the Bright state and increases slowly for the Dark state. The counts in the Dark state come from the off-resonant coupling. In the experiment, we repeat the measurement 1000 times for each duration setting, and the counts in Figure 3.14 (a) are the average photon counts for the 1000 times.

To distinguish the Bright state and Dark state, we set the photon count threshold at 1, and we identity the collected photon number n $\leq$ 1 as the Dark state (n > 1 as the Bright state). For example, in the 1000 trials, if we have 800 times of the collected photon number being larger than 1, then we say that the Bright state population is 0.8 (or 80 %). With the threshold method, we can get our detection fidelity of the state $|\uparrow\rangle$ as $F_\uparrow = \eta_{\uparrow\to\uparrow}$ and $|\downarrow\rangle$ as $F_\downarrow = \eta_{\downarrow\to\downarrow}$, where $F_\uparrow = N_{n>1}/N_{total}$ and $F_\uparrow = N_{n\leq1}/N_{total}$, N_{total} is the total number of experiment trials, and $N_{n>1}$ ($N_{n\leq1}$) is the events count for the photon number larger (not larger) than 1. We plot the average fidelity $(F_\downarrow + F_\uparrow)/2$ in Figure 3.14 (b). The insets is the collected photon number distribution with a PMT at 300 μs for the Bright state $|\uparrow\rangle$ and Dark state $|\downarrow\rangle$, where the $F_\uparrow = 0.97$ and $F_\downarrow = 0.99$.

3.4.4　Detection with a camera

The benefit of using the EMCCD (or we call it the camera) in our trapped ion system is the capability of reading out several ions simultaneously in a single trapping zone; this is an essential step towards scaling up the trapped ion system. The EMCCD is a high gain, low noise camera compared to the normal ICCD, and the architecture of the frame-transfer detecting mode is shown in Figure 3.15 (a).

The image of the ions is captured on the image area with a specified exposure time, where the image area contains 512×512 active pixels of our camera (Andor company, model: iXon^{EM} + DU − 897), with each pixel size being $16\mu m \times 16\mu m$ with no gap between the pixels. The incident photons from the ion's fluorescence are converted into photoelectrons (charges). After the exposure process, these accumulated charges are
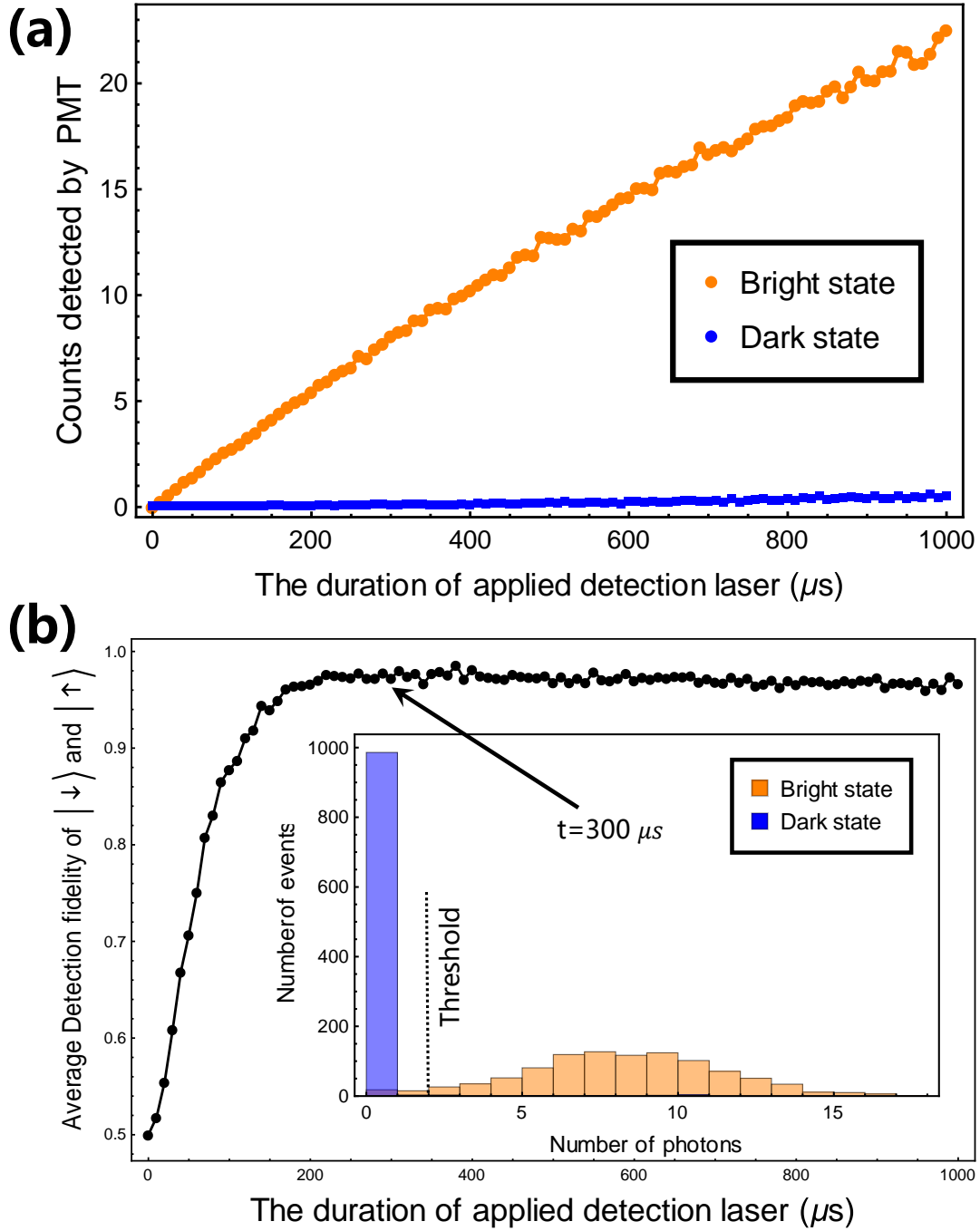
图 3.14 Experimental detection result with a PMT. (a) We experimentally prepare the initial state as $|\downarrow\rangle$ and $|\uparrow\rangle$, then apply a detection beam and collect the fluorescence counts, where we vary the duration of applied detection laser and observe the average photon counts. (b) The average measurement fidelity of $|\downarrow\rangle$ and $|\uparrow\rangle$ with different durations of detection, where we set the threshold as n=1. The insets is the collected photon distribution for the $|\downarrow\rangle$ and $|\uparrow\rangle$ states with 300 μs detection time.

rapidly shifted to the storage area, which prevents any further photons from ruining the data while the charges are reading out from the pixels. The readout of the charges from the storage area is a relatively slow process. It starts by shifting the lowest column vertically down to the readout register, and then horizontally shifts the charges through the gain register. Finally, pixel-by-pixel into the pre-gain register. The charges are converted to a count signal with the ADC (analogue-to-digital converter). When one row in the storage finishes the reading out process, another row is moved vertically down to the readout register. Therefore, the charges are vertically loaded into the readout register row-by-row and is amplified pixel-by-pixel in the gain register.

The high gain of the EMCCD happens in the gain register region. There are certain altering "clock" voltages applied on the horizontal gain register, which guide the movement of the charge between pixels. When the charge is moving to the next pixel, there is a small probability p of the original electron to generate a secondary electron via impact ionization[31,32]. Although p is small in each transfer (0.01-0.02), with a 512 times amplification, we can have a number $(1 + p)^{512}$, and our EMCCD can achieve a maximum gain as $G = 1000$.

The EMCCD detector is connected to a PCI interface card installed in a Windows computer. We can control the camera via the software provided by the factory, SOLIS, or we do the control through Labview, which is embedded in our central control system. The Labview code is in Appendix A. The benefit is that we can synchronize the process of the experiment operations generated FPGA with the camera, where the TTL signal from the FPGA is sent to the camera and alerts the camera to start the data acquiring process. The new version of this iXon^{EM} − 897 is a USB connection, which gives us a more convenient connection and more robust control.

Figure 3.15 (b) shows the procedure of the camera startup and experimental data acquiring. The EMCCD detector head is Peltier-cooled with a fanned heatsink and stays in the stable setting temperature (−80 °C) for our experimental usage, which makes the readout noise less than $1e^-$ with EM gain mode. I noticed that when the temperature of the head is above −40 °C, the efficiency of converting photons into charges is pretty low. The temperature cooling operation should always be active when our experiment is running. After the temperature is stabilized, we start the data acquiring, and the first step is setting the parameters. The EM gain in our setup is 1000, the pre-gain is × 5, the readout speed is 10 MHz, and the other setting parameters are in Table 3.1. Then, we can take the data
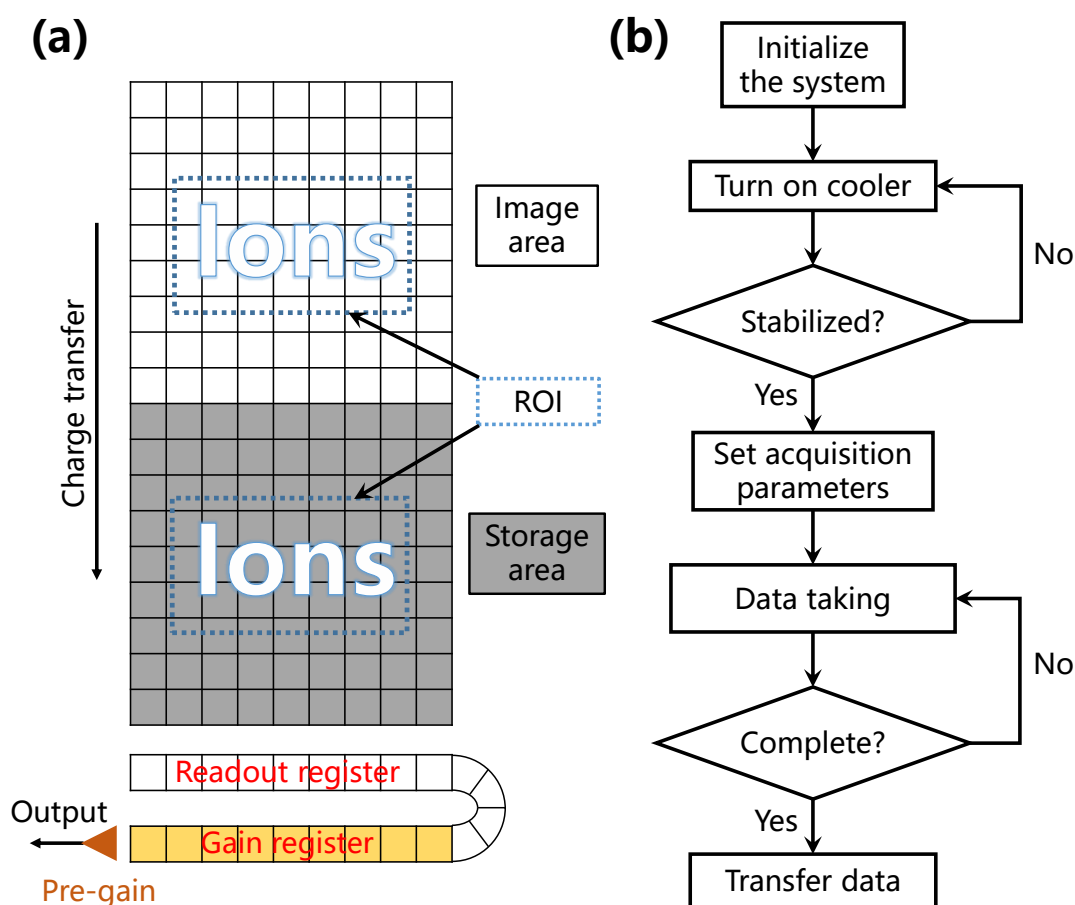
(a)

(b)

图 3.15　Detection process with EMCCD.

once the camera receives the TTL signal from the FPGA, the PCI card counts the number of the photons and sends the final collected data to the computer. We then use Labview to read out the number of counts from memory.

The camera can run in the internal and external trigger mode, and we can select from the two modes in Labview. We use the internal trigger mode as a monitor when we are loading ions, where the software generates the trigger with the specified period, and the period is settled by the setting parameters. The external trigger mode is essential for acquiring data. Here, we use the FPGA to synchronize the camera and other equipment, and the camera is in the external start trigger mode. Once it receives an external TTL rising edge, the camera starts the data acquiring after finish the keep clean cycle. The keep clean cycle is continuously happening while we do not take data, which ensures no charges are accumulated in the image area. Our quantum measurement is typically repeated N (100 to 1000) times. Therefore, we use the kinetic mode to collect all the N times data and send them to the computer after we finish acquiring the N times data.

表 3.1 Parameters setting for the EMCCD readout experiments

Parameter	Settable value	Values used in our experiment
Temperature of detector head (°C)	-120 to 20	-80
Readout modes	Image, Multi-track, FVB	Image
Vertical shift Speed (μs)	0.3, 0.5, 0.9, 1.7, 3.3	0.9
Vertical Clock Amplitude Voltage (V)	0, 1, 2, 3, 4	0
Horizontal shift speed (MHz)	10, 5, 1	10
EM gain	0 to 1000	1000
Pre Amp gain	1, 2.4, 5	5
Binning	1×1, 2×2, 4×4, 8×8	2×2
Region of interest		user define
Exposure time		user define
Number of kinetics		user define
Frame transfer mode	ON, OFF	OFF
Keep clean cycle	Enable, Disable	Enable

One remaining feature is acquiring the data with efficient time. The exposure time is determined by the laser shining time; we use the Region Of Interest (ROI) scheme to reduce the time of acquiring data in our experiment, where we set a small region that is less than the full image for the data taking. The ROI is indicated with dashed blue lines in Figure 3.15 (a). The working principle illustrates that the horizontal dimension of the ROI does not vary the readout time by much, but the vertical dimension of the ROI will affect the readout time a lot. Since the ion in the Paul trap is a linear chain, we experimentally put the ion chain along the horizontal direction of the image area. Therefore, the readout time for one ion and a long chain of ions is same.

When we are obtaining the photon counts of the ROI, we use the Binning in the vertical direction to accelerate the data readout process, and typically the data in the vertical direction is compressed into one column. From here, we have two ways to move on: one is the average method, which averages the counts of all the pixels; and the other method is fitting the photon distribution with the compressed one column of data and getting the brightness of each ion. I tested these two methods in our system and found that the data fitting method can provide a more stable result regarding the number of noisy photons fluctuations. The fitting function is the Gaussian function:

$$f(x) = A \times \exp\left(-\frac{(x-\mu)^2}{2\sigma^2}\right) + f_0 \tag{3-15}$$

where the offset f$_0$, position μ and distribution width σ are experimentally calibrated with an initializing of all the ions to Bright state $|\uparrow\rangle$, and we use the value obtained from calibration to do the experimental data fitting. In the fitting of experimental data, we only read the brightness of the ion, which corresponds to the value of A.

In the data processing step, we divide the ROI into several sub-images, and each image maps to one ion. Then we fit each sub-image and get the brightness A. Similar to the detection scheme with the PMT, we repeat the experiment N times and obtain the state population of each ion. Besides, we can also obtain the correlation between the ions in the camera detection. Here, I want to mention that the reason I do not use the $\sum f(x)$ to fit all the ion's count at once is mainly due to the fact that fitting with a complicated function is easy to fail in Labview. Therefore, I divide the ROI into sub-images.
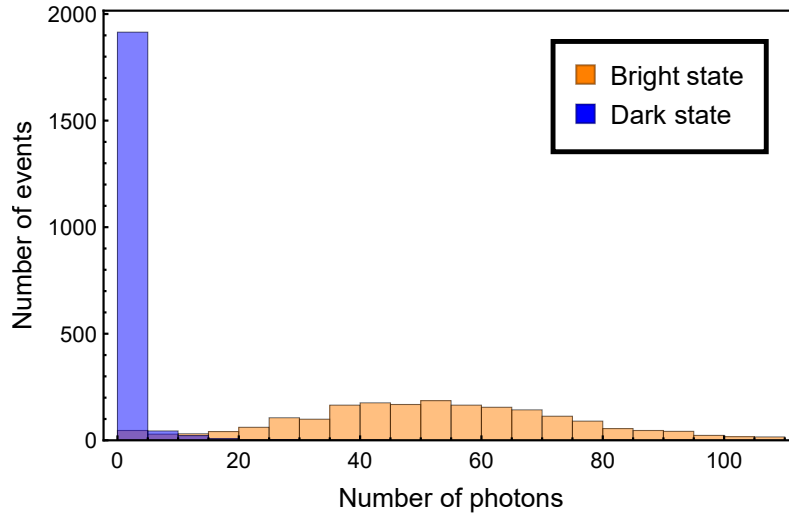

图 3.16 Single ion detection result with the EMCCD.

In the experimental setup of EMCCD detection, we improved our imaging system and used an N.A.= 0.6 objective lens to reduce the detection time (from Photon gear Inc, a customized lens[33]). The camera detection data for a single ion is in Figure 3.16, where we use the exposure time $800\mu s$ for the EMCCD, and optimize the detection laser beam intensity to make sure the mean photon number is about 50 for the Bright state. We use a 10 pixel $\times$ 10 pixel ROI to capture the image of the ion, and binning is 2×2. Then we experimentally prepare the Dark state $|\downarrow\rangle$ via the optical pumping process and prepare the Bright state $|\uparrow\rangle$ via a microwave π-pulse carrier transition. We repeat the process 2000 times for the detection of Bright state and Dark state, and collect the fluorescence photons during the 2000 times. With the threshold setting at 5 photons, we obtain the single ion

detection fidelity with the camera as $F_\downarrow = 0.969$ and $F_\downarrow = 0.971$.

We also experimentally checked the detection performance of two ions with the EMCCD, where we used the microwave to prepare the two ions in the $|\uparrow\rangle_1 |\uparrow\rangle_2$ state, and used optical pumping to prepare the two ions in $|\downarrow\rangle_1 |\downarrow\rangle_2$. The photon distribution of the two ions' Bright state and Dark state is in Figure 3.17. With the threshold setting at 5 for the first ion, and threshold setting at 2 for the second ion, we have the state fidelity for each ion as $F_{\downarrow,1} = 0.968$, $F_{\downarrow,2} = 0.976$, $F_{\uparrow,1} = 0.97$ and $F_{\uparrow,2} = 0.961$. The tiny detection fidelity difference with the single ion result comes from the crosstalk of the detection system.
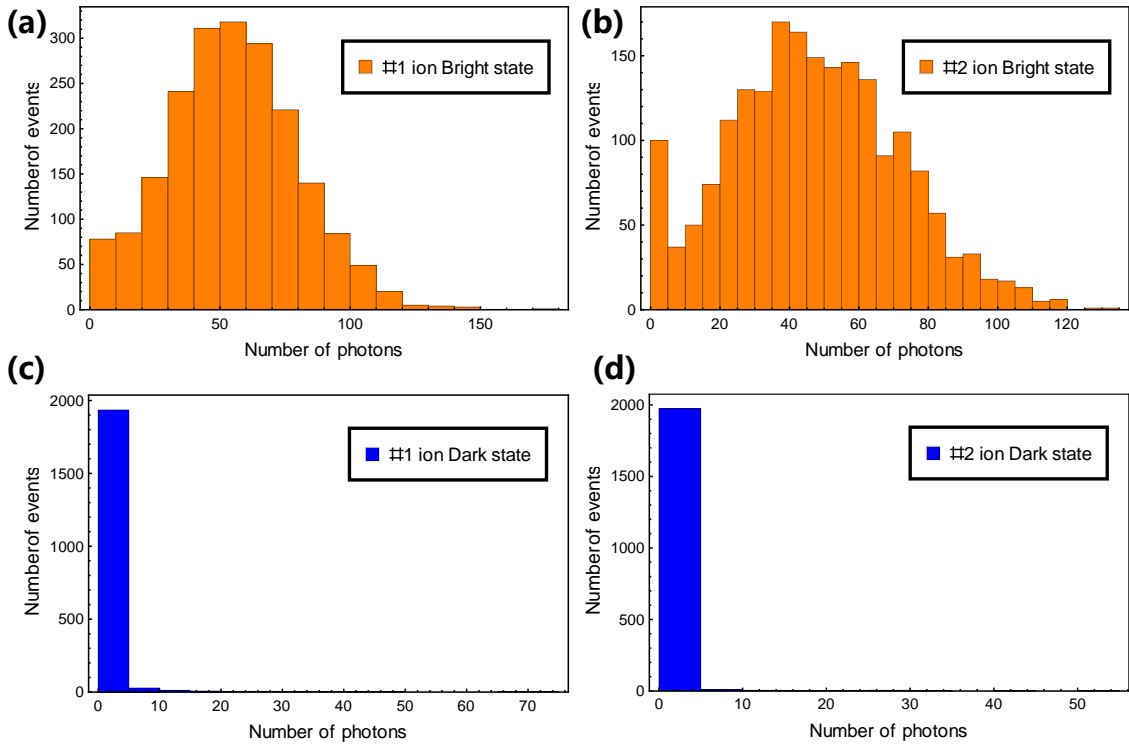
图 3.17 Two ions detection result with the EMCCD.

3.4.5 State-detection-error correction

Our quantum state detection with either the PMT or EMCCD is always not perfect, where the imperfection comes from the detector, off-resonant coupling, and scattering photons. Here, we use the theoretical proposal in Ref. [34] to correct our experimental data, which mainly corrects the errors caused by the detectors. This method gives us the opportunity of using imperfect detectors to simulate perfect detectors as long as their imperfection has been calibrated.

For a single qubit, the most general error model is characterized by a 2×2 matrix

$$D_1 = \begin{bmatrix} \eta_{\downarrow \to \downarrow} & 1 - \eta_{\uparrow \to \uparrow} \\ 1 - \eta_{\downarrow \to \downarrow} & \eta_{\uparrow \to \uparrow} \end{bmatrix} \tag{3-16}$$

where $\eta_{\downarrow \to \downarrow}$ ($\eta_{\uparrow \to \uparrow}$) is the probability of the Dark state being detected as a Dark state (Bright state being detected as a Bright state). The single qubit state correction is in Eq. 6-20.

For n qubits, we have the a possible outcome of 2^n states, and for each state, we have an experimentally measured probability $P_M(i)$, and a real state probability $P_R(i)$, where i is ranging from 1 to 2^n. Then the relation between the measured state and real state set is

$$P_M(1, 2, ..., 2^n) = \otimes_{k=1}^{n} D_k \cdot P_R(1, 2, ..., 2^n) \tag{3-17}$$

where D_k is the correction matrix for the k-th ion.

Figure 3.18 shows the state evolution of two ions under a microwave with state-detection-error correction. The initial state of the two ions is $|\downarrow\rangle_1 |\downarrow\rangle_2$, and we use the measured fidelity in section 3.4.4 to correct our experimental measured data. The microwave is a global operation to the two ions, and due to the close distance between the two ions (about 5 μm), we observe the same speed of flipping the spin.
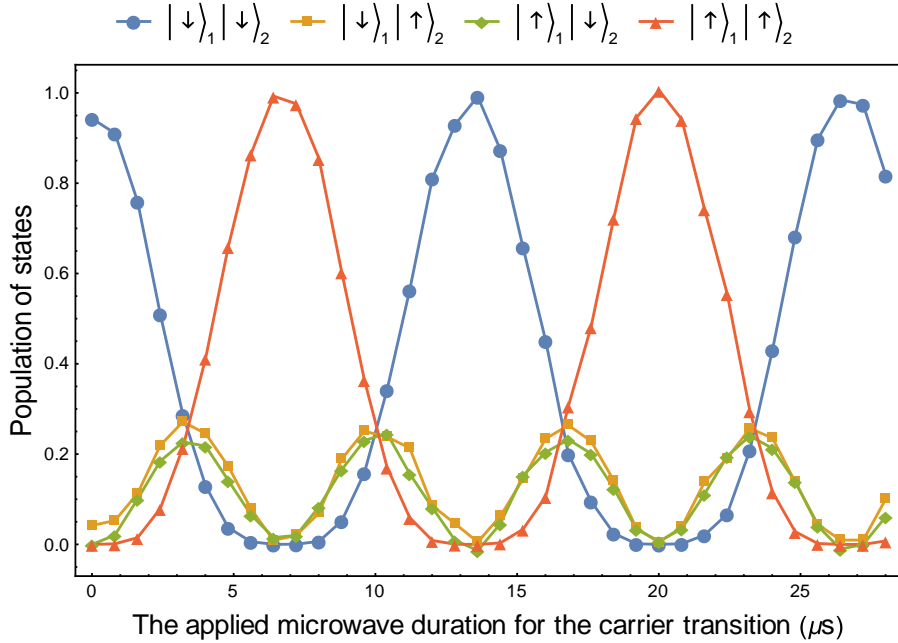

图 3.18　State-detection-error corrected data for the evolution of states of two ions.

第4章　Techniques involved in the trapped ion system

4.1　Schematic diagrams of optical beam path

In this section, I will introduce the optical path of the lasers we use daily, including the continuous-wave lasers (399 nm, 638 nm, 935 nm and 370 nm) and the picosecond pulsed laser (Mira-HP). These schematic diagrams can be a reference for new students who work in the laboratory.

4.1.1　Continuous-wave lasers

Four continuous-wave lasers are serving in our lab for the trapped Yb^+ ion system: 399 nm, 638 nm, 935 nm and 370 nm (from Toptica company). The 370 nm laser is our main laser, and the optical path is a little bit complicated. The rest of the three lasers are used for ionization or repumping, which have a relatively simple optical path.
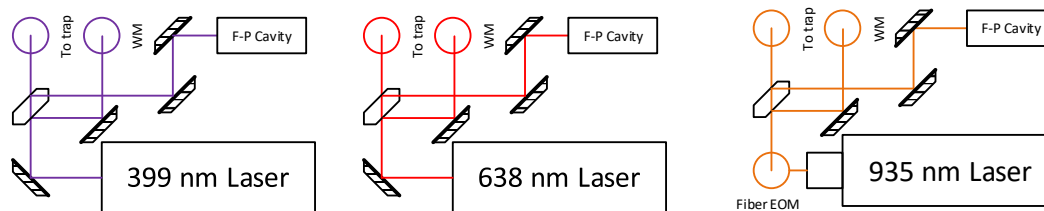

图 4.1　The optical path of 399 nm, 638 nm and 935 nm lasers in our trapped Yb^+ ion system.

We present the optical path of the 399 nm, 638 nm, 935 nm lasers in Figure 4.1; these three lasers are tunable single-mode Diode Lasers. We use a mica plate to split the power of the laser, and most of the laser beam power is transmitted through the mica plate. We couple this beam to a single-mode fiber and send it to the trap. The mica plate reflects two laser beams from the front surface and the back surface, and we use the reflected laser beam from the front surface to monitor the wavelength (WM in the figure) and the reflected laser beam from the back surface to track the modulated frequency sidebands (F-P Cavity in the figure). The F-P Cavity we are using in the experiment is from the Thorlabs company, which carries a Free Spectral Range (FSR) 1.5 GHz.

For the 399 nm and 638 nm laser beam optical path, the lasers are directly outputted

to free space from the laser body. The 935 nm is coupled to a fiber EOM through a FiberDock, which is used to generate a 3.1 GHz frequency sideband. Due to the fiber coupling efficiency, we lose about 20 mW beam power through this fiber EOM, and the final output power from the fiber EOM is 26 mW for our experimental usage.

Our 370 nm laser is from Toptica, which a high power semiconductor (TA) and frequency doubling stage (SHG pro) integrated tunable Diode laser. We split the amplified 740 nm laser beam into two paths inside the laser body: one is a direct output for the frequency stabilization, and the other beam is sent into the second-harmonic-generation cavity to generate the 370 nm laser beam. The 740 nm laser is frequency stabilized via a home-made optical cavity and the absorption signal of the iodine. See section 4.2.1 for the details of frequency stabilization.

Our quantum control of the ^{171}Yb$^+$ ion requires four laser beam components from the 370 nm laser:

- Strong beam (used for ion loading): about 1 mW, wavelength at 370 nm.
- Doppler cooling beam: about 10 μW, red detuned from the transition between ^{2}S$_{1/2}$ $|F = 1\rangle$ and ^{2}P$_{1/2}$ $|F = 0\rangle$, and carries a 14.7 GHz sideband.
- Optical pumping beam: about 5 μW, resonant with the transition between ^{2}S$_{1/2}$ $|F = 1\rangle$ and ^{2}P$_{1/2}$ $|F = 0\rangle$, and carries a 2.105 GHz sideband.
- Detection beam: about 5 μW, resonant with the transition between ^{2}S$_{1/2}$ $|F = 1\rangle$ and ^{2}P$_{1/2}$ $|F = 0\rangle$.

There are two basic ideas to implement the optical path of the 370 nm laser. One is splitting the laser beam from the very beginning into four paths, and propagating all the paths in a parallel structure. Another way is to align all the beam power to the trap, and during the laser propagating, we use AOMs to generate Doppler cooling, optical pumping, and detection, which is a series structure, shown in our design in Figure 4.2.

The Half-wave plate and Quarter-wave plate are used to adjust the polarization of the laser beam in our setup. The polarization of the laser beam is essential for the diffraction efficiency of the AOM and operations applied via the laser. The AOMs here are used as the fast optical beam switches (several nanoseconds) and play the role of a frequency shift (about several hundred MHz). In our experimental setup, the AOMs are on the laser beam waist position to achieve a high diffraction efficiency. The EOMs used here are driving by RF sources to generate the designed frequency sidebands of the laser. We use optics called the dichroic mirror to combine two laser beams that have a different wavelength,

with one beam passing through and the other beam reflecting from the Dichroic mirror (both efficiency higher than 90%). For laser beam of the same wavelength, i.e., the four components of the 370 nm laser beam, we use a PBS to combine them.

4.1.2 Picosecond pulsed laser

Our picosecond pulsed laser can generate an output of 375 nm laser of about 500 mWatt, where the laser is generated by the pumping of a high power 532 nm laser (Coherent company, Verdi G18, maximum output 18 W). The beam path of the picosecond pulsed laser is shown in Figure 4.3. We use the frequency comb of the pulsed laser to implement our quantum operations, an idea that is based on the stimulated Raman transition, which is a two-photon process. In the experiment, we use the first order output of AOM1 and AOM2 to generate two laser beams, and we compensate the arm length difference of two laser beams by a delay stage. In the experiment, we use a standard RF source to drive the AOM2 and keep the frequency fixed, and then we vary the input RF signal of AOM1 to realize different quantum operations.

The repetition frequency signal is observed via an ultra-fast photodiode, and we compare this signal with a standard RF source, which offers a reference for the stabilization of the repetition frequency. The AOM0 is used as a noise eater of the laser intensity, and this is an essential tool to compress the fluctuation of the laser beam intensity.

4.2 Frequency Stabilization of continuous-wave lasers

4.2.1 Stabilization of the 740 nm laser through an optical cavity and the iodine absorption signal

To realize an efficient quantum operation, the frequency stabilization of the 370 nm is essential in our system. Our 370 nm laser is frequency doubled from the 740 nm laser. From the output of the 740 nm laser, we can get big power (about 30 mW) for the usage of frequency stabilization. Thus we experimentally stabilize the frequency of the 740 nm laser by using a home-made optical cavity with the Pound-Drever-Hall (PDH) scheme[35], and the absorption signal of the iodine is used to provide an absolute frequency reference to stabilize the length of the optical cavity. The schematic diagram is shown in Figure 4.4.

In the experimental setup, the PDH module inside the controller box of the 740 nm laser offers a voltage modulation with frequency ω_m, and this modulation is applied to the diffraction grating piezo of the external cavity of the laser diode. Then the electric field

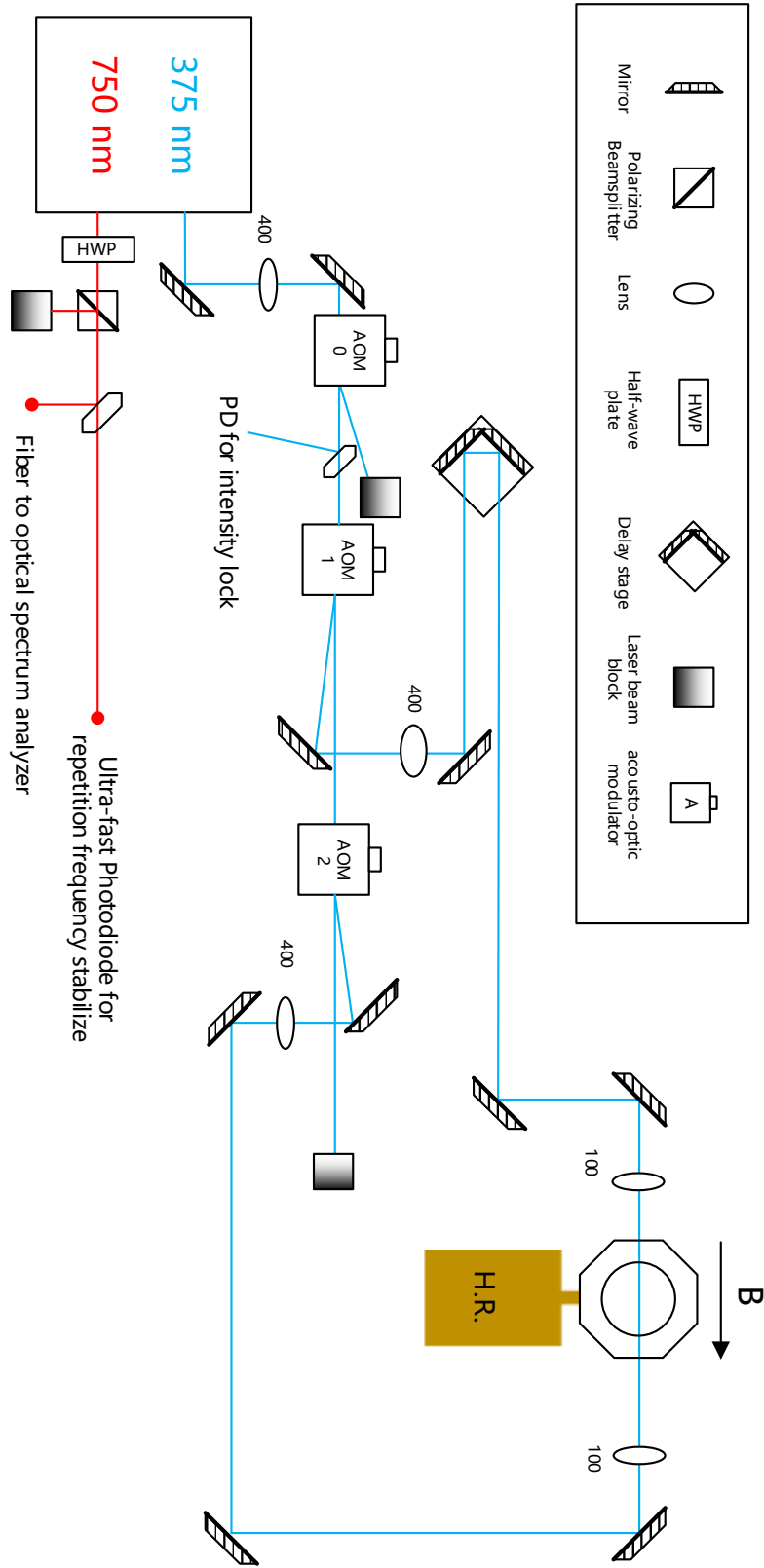图 4.2　The laser optical path of 370 nm in our trapped ion system.

图 4.3　The laser optical path of Picosecond pulsed laser in our trapped ion system.

of output laser beam is $E_0 e^{i(\omega_{\text{laser}}t + \beta \sin(\omega_m t))}$, which is similar to the working principle of EOM. Our home-made optical cavity is 15 cm in length and has a finesse 200. We send the reflected laser beam from the optical cavity to a photodiode and transfer the signal generated from the photodiode to the PDH module in the control box of the laser. The PDH module contains a phase shifter and a mixer, which obtains the derivative of the error signal. We send this PDH signal to a home-made PID (proportional–integral–derivative controller) electronic board and generate the feedback to the diode current of the laser.

Due to the temperature fluctuation, the length of the optical cavity can vary in the time domain. Therefore, we need to stabilize the length of the optical cavity and provide a more precise stabilization signal to the laser. One method is isolating the optical cavity from the environment, e.g., putting the optical cavity inside a vacuum chamber. Here, we use the absorption signal of iodine to provide an absolute reference. In the experiment, we use a fiber EOM (which shift the laser frequency by 13 GHz) to deliver 3 mW of the 740 nm laser beam to the optical path of the iodine part. We split the 3 mW laser beam into the pump beam and the probe beam, and these two beams counter-propagate through the iodine vapor and generate an error signal. The iodine vapor is heated to 350 °C, which makes the solid iodine becomes gas. The pump beam is phase modulated by a 15 KHz RF signal and together with the probe beam, we generate the saturated Doppler-free signal. Finally, we send the Doppler-free signal to a Lock-In amplifier to extract the error-signal, and the error-signal is passed to a home-made PID, where the PID generates a feedback signal to stabilize the length of the optical cavity.

4.2.2 Stabilization of the 935 nm laser through the wavelength meter

The free-running linewidth of the 935 nm laser is less than 10 MHz in a short time-scale, which is already enough for our experimental usage. However, in the experiment, the wavelength of the laser is always drifting in a long time-scale. We stabilize the 935 nm laser via the software of HighFinesse wavelength meter, where the software takes the measured value of the 740 nm laser as a reference. The software PID controls the feedback voltage to the laser diode. In our setup, as the intensity of the 935 nm laser beam focused at the ion position is much larger than the saturation intensity. Therefore, we did not notice a significant jump in the fluorescence counts while the wavelength has a small perturbation.
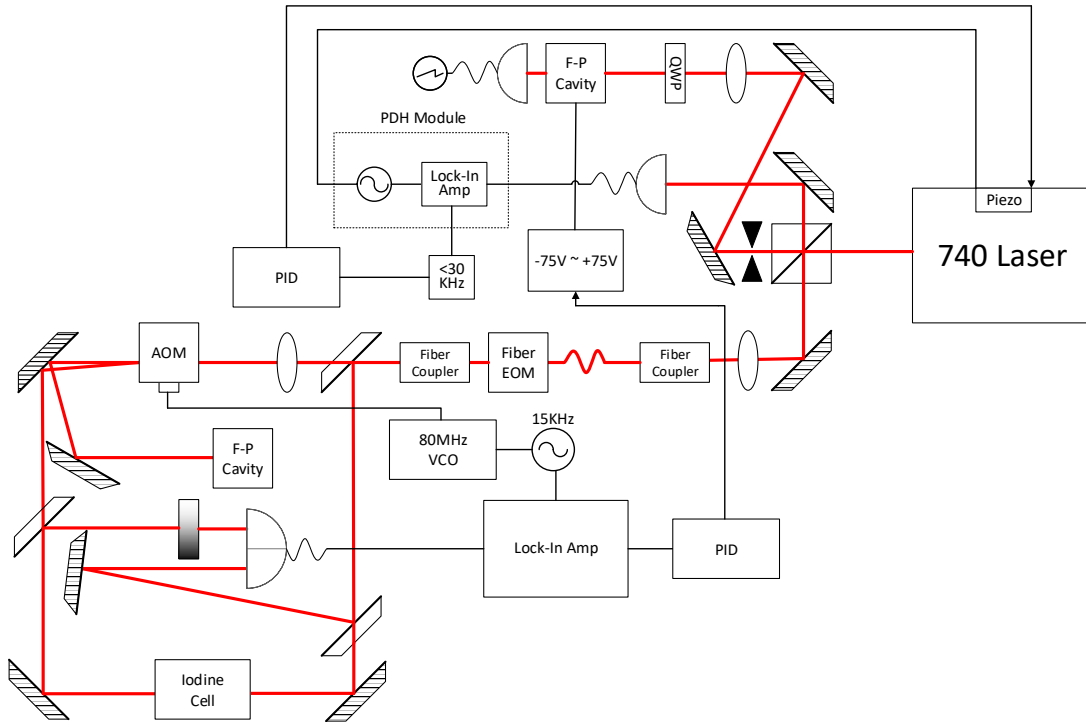
图 4.4 Stabilization of the 740nm laser through an optical cavity and the iodine absorption signal. The frequency of the laser is stabilized via a home-made optical cavity, and the length of the optical cavity is referenced to the absorption signal of iodine. The solid red lines in the figure illustrate as 740 nm laser.

4.3 Stabilization of the pulsed laser

4.3.1 Stabilization of intensity

To perform a good quantum operation via the Raman laser, we need to stabilize the intensity of the picosecond pulsed laser. Figure 4.5 shows the schematic diagram of the intensity stabilization. We use the Acousto-optic modulator (AOM) to realize an intensity noise eater of the laser beam. The AOM is based on the principle that sound waves traveling in a transparent medium locally changes its refractive index. If a frequency Ω of RF drive signal is applied to the AOM, the diffraction angle θ of the AOM is

$$\sin\theta = \frac{m\lambda}{2\Lambda} = m\frac{2\pi c}{n_0\omega} \Big/ \frac{2\pi v}{\Omega} \tag{4-1}$$

where n_0 is the refractive index of the medium, c is the speed of light in vacuum, ω is the frequency of the incident laser, v is the speed of sound in the medium, and $m = \ldots -2, -1, 0, 1, 2, \ldots$ is the order index of diffraction beams. For the AOM we are
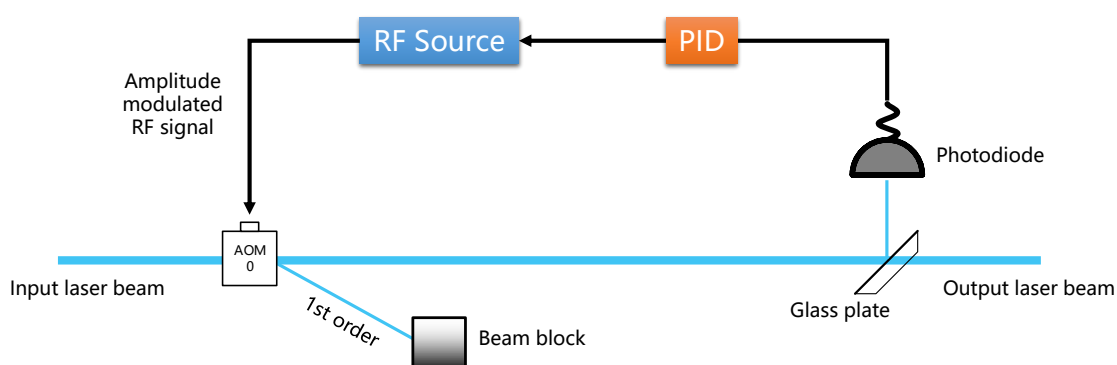
图 4.5　Stabilization of laser beam intensity of the picosecond pulsed laser.

using here, the sound speed is 4200 m/s. We typically use the 1st order (or the minus 1st order) diffraction beam, which has an output frequency shift of $\omega + \Omega$ (or $\omega - \Omega$).

The power ratio between the 1st (or minus 1st) order diffraction laser beam and the incident beam power is proportional to $\sin(\sqrt{I_s})^2$, where I_s is the intensity of the sound wave. In the small range of I_s, it is linearly controlled via the modulated RF power that is generated by the RF source.

Figure 4.5 shows our intensity stabilization of the Raman laser optical path. A large power of 375 nm laser beam (about 500 mW) is generated from the pulsed laser and sent to the optical path of the Raman laser. The AOM0 locates at the very beginning part of the optical path, and we input a small amount of the driving RF power to generate a weak first-order sideband. Then, in the remaining zero-order path, we use a glass plate to reflect a small beam power, and the reflected beam shoots into a high-speed photodiode. The photodiode is used to detect the intensity of the laser (Thorlabs company, model: DET 110). The photodiode feels the same fluctuation in the laser intensity as the main beam fluctuates. The detected electric signal is transferred to a PID to generate a feedback voltage to the RF source, where the RF source is amplitude modulated. In such a loop, we achieve the stabilization of laser intensity.

The experimentally measured data shows that the intensity fluctuation of the laser beam power can be suppressed down from 1% to 0.1% with our stabilization system.

Figure 4.6 shows the experimentally measured result of the beam waist of the Raman laser. We change the repetition frequency of the Raman laser, to satisfy $(2\pi)(166 \times 76.161519)$ MHz $= (2\pi)12.64281196$ GHz $= \omega_{HF}$, which gives the chance of a single Raman laser beam to excite the carrier transition. In the experiment, we mount the

focusing lens on a 3-dimensional transition stage and change the horizontal and vertical position of the stage. Then, we record the Rabi frequency of the corresponding carrier transition. Since the Rabi frequency is proportional to the intensity of the laser felt by the ion, we can obtain the beam waist of the laser via fitting the experimental data with different positions. With fitting, the beam waist of the laser is 50 to 60 μm. In the real experiment setup, we cover the whole pulsed laser body and the Raman optical beam path to reduce the perturbation from the airflow.
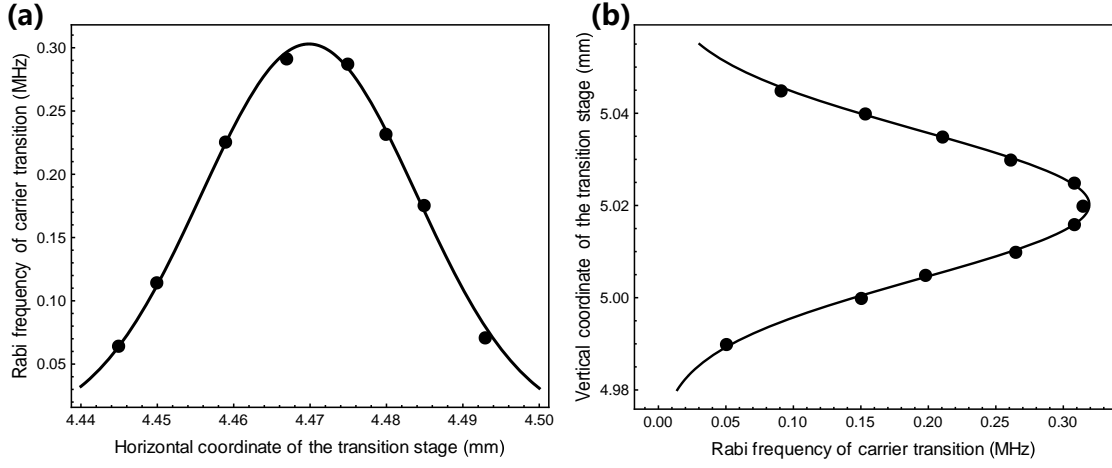

図 4.6　The measured result for the beam waist of the Raman laser. By fitting the experimental data, we obtain the beam waist in the horizontal direction (a) is 56.4 μm, and vertical direction (b) is 64.2 μm. The beam waist mentioned here is the full width at half maximum of the fitted peak.

4.3.2　Stabilization of repetition frequency

The inner optical cavity of the Mira-HP laser has a slow drift in length as the environment changes. Our quantum operations implemented via the Raman laser are based on the frequency comb. Hence the stability of the repetition frequency of the pulsed laser is essential for us. In our previous setup, we dynamically varied the input frequency of the AOM to ensure that the $\omega_{\mathrm{AOM}} + n\omega_{\mathrm{rep}}$ is an absolute value, i.e., equal to ω_{HF}. In our current scheme, we add an electric piezo to the Tweeter Mirror of the optical cavity inside the Mira-HP laser. This piezo provides direct access to stabilizing the length of the optical cavity, where we can stabilize the repetition frequency by stabilizing the length of the laser's inner optical cavity that generates the pulsed laser.

Inside the pulsed laser body, the inner optical cavity has two components to adjust the length of the cavity. One is the Stepper Motor, which can change the cavity by ± 1 cm,

which corresponds to the change in repetition frequency domain as ± 0.4 MHz. The other component is the piezo in the back of the Tweeter Mirror, and it can change the cavity length by 8 ± 1 μ m, which corresponds to the change in repetition frequency domain as ± 250 Hz. In the experiment, we use the stepper motor to realize a coarse adjustment, and the piezo is used for precise stabilization.
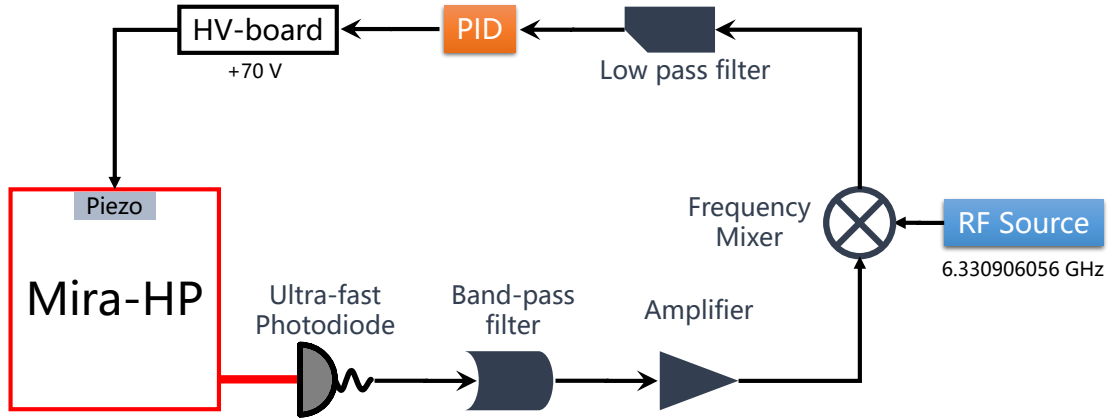
图 4.7　Stabilization of the repetition frequency of the picosecond pulsed laser.

The stabilization of the repetition frequency of the picosecond pulsed laser is shown in Figure 4.7. We use an ultra-fast photodiode to capture the repetition frequency signal of the pulsed laser, and the photodiode has a bandwidth larger than 12.5 GHz (From EOT company, model: ET-4000). The electric signal read from this photodiode not only contains the base frequency ω_{rep}, but also contains all the higher orders $n \times \omega_{\mathrm{rep}}$ terms, which gives us the ability to stabilize the repetition frequency with much higher accuracy. We pick up the 83th order signal via a narrow band-pass filter (from a local company), which locates at 6.31191 GHz. Then this signal is amplified with two amplifiers (Minicircuit company, model: ZVA-183-S+ and ZVE-3W-183+) to get a significant amplitude, and we mix the amplified signal with a standard RF source, whose mixer model is ZMX-7GR. After that, we filter out the high-frequency noise with a low pass filter, and the filtered signal is sent to the PID to generate an error signal. Before feeding back the voltage signal to the piezo, we need to add a static offset to the voltage, since the drive voltage of the piezo is 70 ± 60 V. Therefore, we use a home-made HV board to provide the 70 V offset.

The choosing frequency of the repetition frequency should be very careful because we do not want to excite any states via a single Raman beam. We make a (2π) 19 MHz

difference between the carrier transition and $n \times \omega_{\text{rep}}$

$$n \times \omega_{\text{rep}} - (2\pi)19 \text{ MHz} = \omega_{\text{HF}} \tag{4-2}$$

where we set $n = 166$ and $\omega_{\text{rep}} = 76.047061$ MHz.

The frequency of the standard RF source used in our setup is $\frac{n}{2} \times \omega_{\text{rep}} = 83 \times \omega_{\text{rep}} = 6.311906056$ GHz. We measure the stabilized repetition frequency with an RF counter, which shows the fluctuation of our repetition frequency to be less than 0.1 Hz.

4.4 Improvement for the coherence time of internal state and motional state

4.4.1 Reduction of the laser beam scattering

We have a magnetic field insensitive qubit $|\downarrow\rangle$ and $|\uparrow\rangle$, which has a long t_1 and t_2 time. However, the laser beam scattering (or beam leakage) from Doppler cooling, optical pumping and detection affect the coherence of the qubit a lot.

We experimentally measure the phase coherence of the qubit as the scheme described in Figure 4.8 (a), where we apply a $\pi/2$ carrier pulse with 0 phase after optical pumping, and generate the state $\frac{1}{\sqrt{2}}(|\uparrow\rangle + |\downarrow\rangle)$. Then we switch off the laser beam with a Ramsey gap time, and after that, another $\pi/2$ carrier pulse with π phase is applied. Finally, we measure the Bright state population. Here, the applied drive frequency of the carrier transition is different from the nature atomic resonant frequency (also called Ramsey frequency); the difference between the applied drive frequency and Ramsey frequency is the oscillation frequency in Figure 4.8 (b) and (c). We fit the experimental data and get the coherence for (b) is 2.5 ms, and (c) is 10.6 ms, where (b) is the case that contains some scattering from the 370 nm laser beam, and (c) is the result after we carefully optimized the optical beam path to reduce the scattering. We can also notice that the oscillation decay with some laser beam scattering will not converge to 0.5, but larger than 0.5, as shown in Figure 4.8 (b). This is due to the difference of states number between Bright state (three states: $|\uparrow\rangle$, $|+\rangle$ and $|-\rangle$)) and Dark state (one state: $|\downarrow\rangle$).

From the above experiment, we realized it is important to block the laser beam while we do not shine any 370 nm laser beam to the ion. This method can minimize the laser beam scattering and improve the coherence time of the clock state qubit. We found that the Electric-optic modulator is helpful for the laser beam switching (from the Comoptics INC company, model: 350-105), which contains a crystal inside the body and varies the

(a)

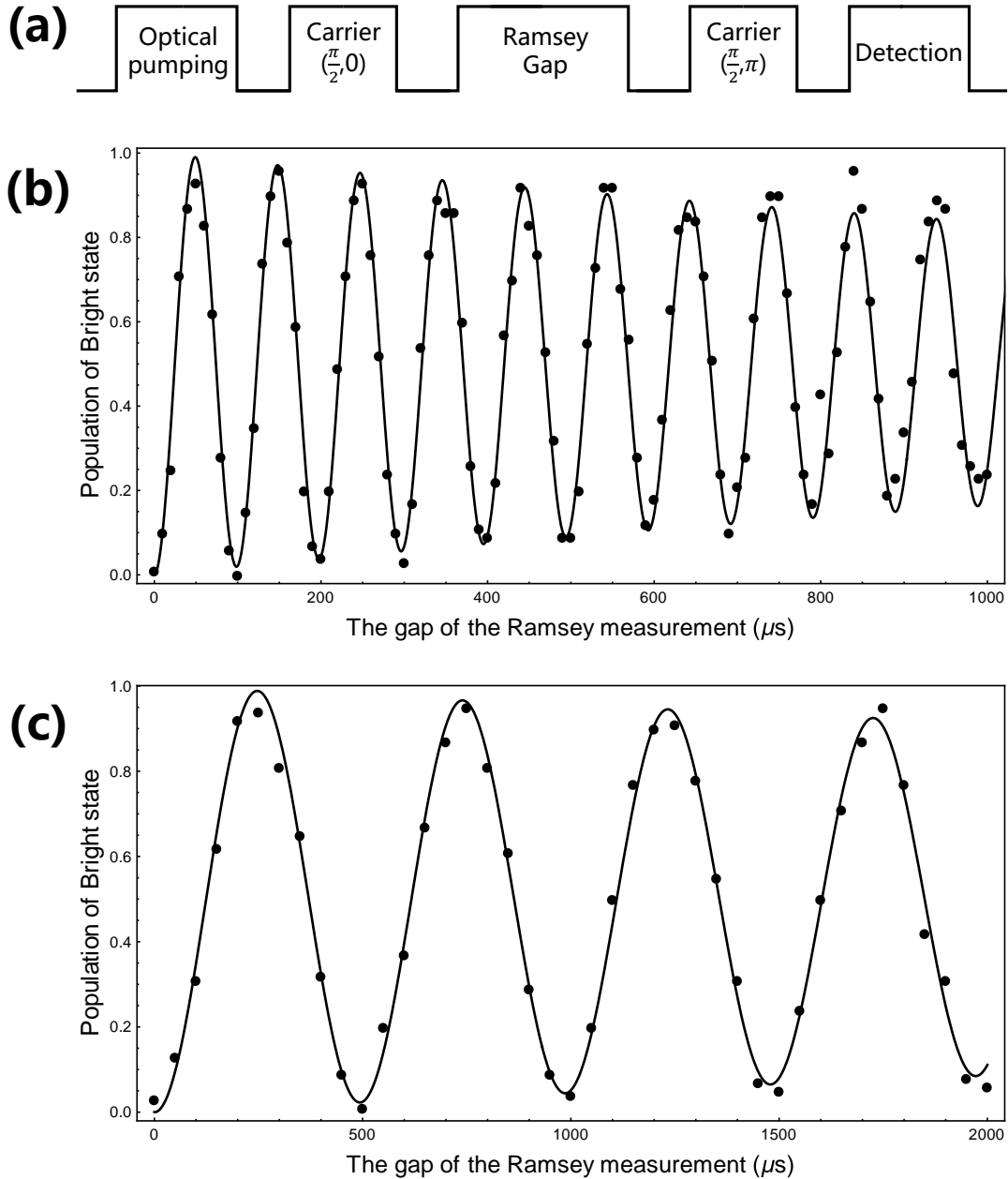| Optical pumping | Carrier $(\frac{\pi}{2},0)$ | Ramsey Gap | Carrier $(\frac{\pi}{2},\pi)$ | Detection |

(b)

(c)

图 4.8　Measurement of the phase coherence time of the clock state qubit. (a) The experimental measurement scheme for the gauge of coherence time of the qubit state, where we vary the Ramsey gap time to obtain the oscillations. (b) and (c) The measured coherence time with a large laser beam scattering and a reduced laser beam scattering. The difference between the applied drive frequency and Ramsey frequency is the oscillation frequency. The black dots are experimentally measured values and curves are the fitting results.

polarization of the laser beam based on the applied high DC voltage. There is also a PBS inside the EO modulator, and together with the crystal that changes the direction of polarization, we can switch the laser beam without changing the propagating direction of the laser beam. The Model 25D drive electronics is a high voltage push-pull power amplifier, which is capable of output voltage swings in the order of 175V P-P and provides the output repetition rates from the DC-30MHz (with a regular rise and fall times of 8 ns).
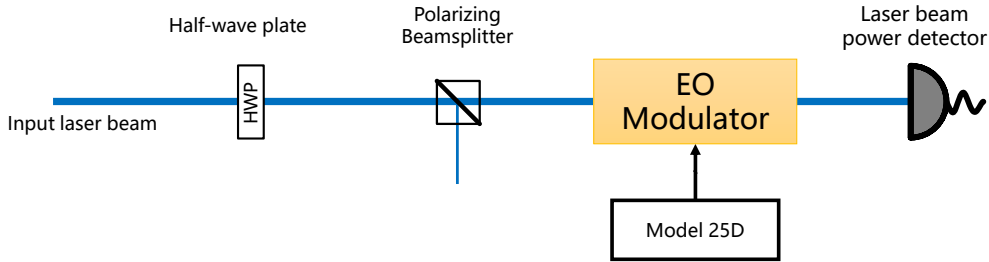

图 4.9 Experimental test of the EO modulator.

In the optical setup for testing the EO modulator, as shown in Figure 4.9, we use a PBS to purify the polarization of the input laser beam, change the applied voltage on the EO modulator, and then measure the output laser beam power. In the experiment, we reach a ratio between the maximum output power and minimum output power to be 180, which is a significant improvement for our laser beam switching off. In the later experimental work of realizing long coherence time for qubits[21], we use this EO modulator to block the laser beam and minimize the scattering.

4.4.2 Stabilization of the RF power in Helical Resonator

The stabilization of the RF power in the trap is essential for us, due to the manipulating of the motional modes in the trap strictly relying on the stability of the trap frequency. As we can see in Eq. (2-4) and (2-5), the trap frequency in the radial axis is proportional to the amplified voltage V_0 after the Helical Resonator, and is inversely proportional to the drive frequency Ω_T of the Helical Resonator. If we want to achieve high stability of the trap frequency, we need to stabilize both V_0 and Ω_T. Here, I am going introduce the first stage achievement by only stabilizing the V_0 in our setup.

Figure 4.10 shows the experimental measurement of the phase coherence time of the motional modes. We initialize the state of the ion to the motional ground state and
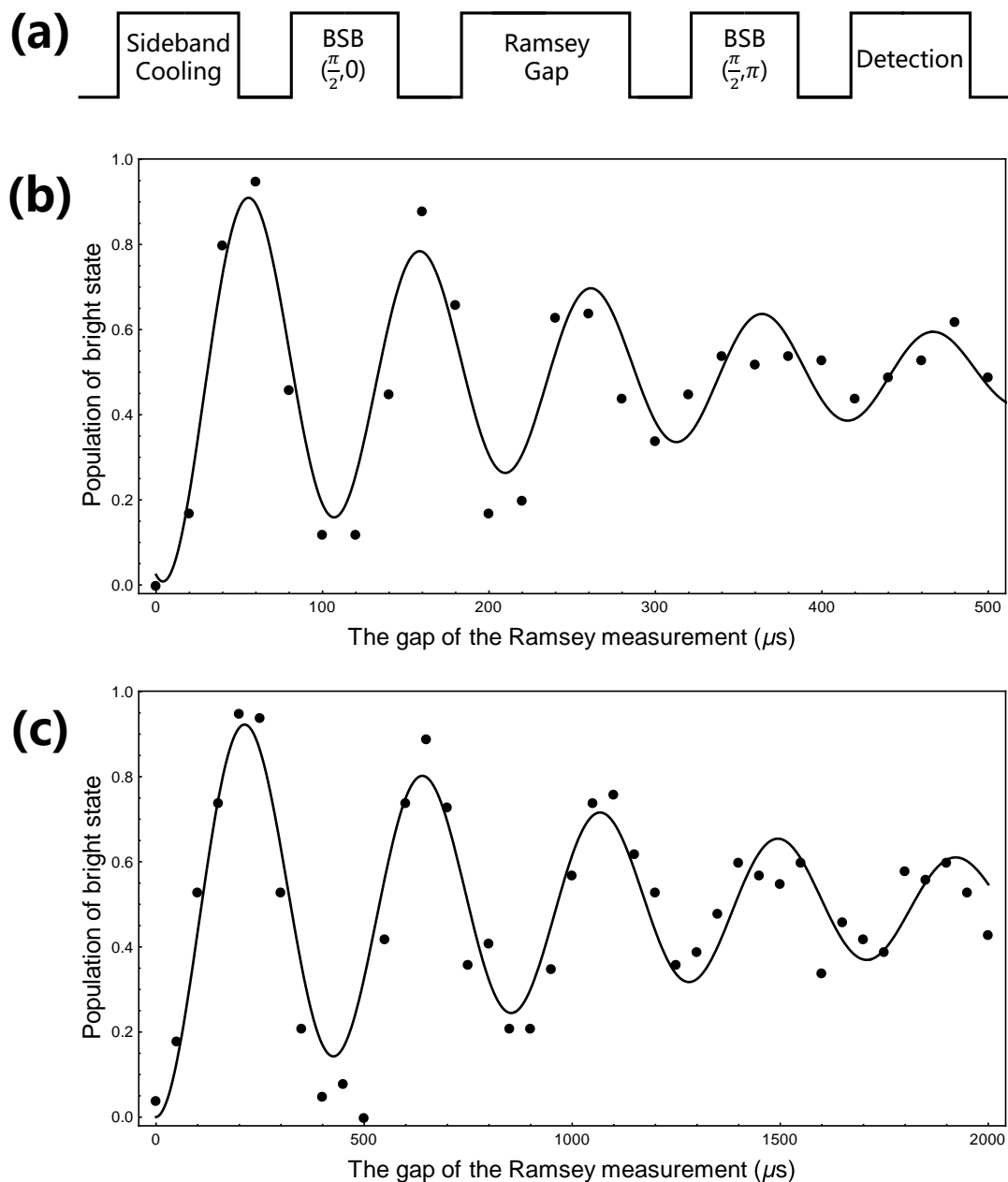
图 4.10 Measurement of the phase coherence time of the motional state. (a) The experimental measurement scheme for the gauge of coherence time of the motional state, where we vary the Ramsey gap time to obtain the oscillations. (b) and (c) The measured coherence time without and with the stabilization of the trap RF power to the trap. The difference between the applied drive frequency and Ramsey frequency of blue sideband transition is the oscillation frequency. The black dots are experimentally measured values and curves are the fitting results.

then apply the standard Ramsey measurement scheme. Here, we use a $\pi/2$ blue sideband pulse with 0 phase to generate the $\frac{1}{\sqrt{2}}(|\uparrow, 1\rangle + |\downarrow, 0\rangle)$. Then a Ramsey gap time with the laser switched off, after which another $\pi/2$ blue sideband pulse with π phase is applied. Finally, we resolve the bright state population and get the oscillation in Figure 4.10 (b) and (c). We fit the experimental data and get the coherence time of the motional state without stabilizing the RF power as 0.3 ms, and 1.3 ms with stabilizing of the RF power.
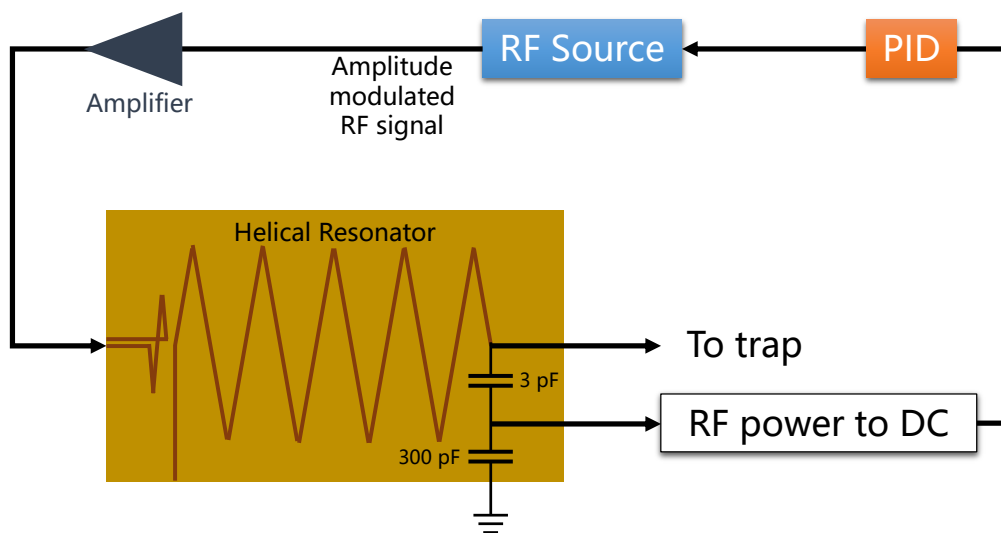

图 4.11　Schematic diagram for the stabilization of the RF power that supplies to the trap.

We actively stabilize the trap RF power via picking up a fraction of the RF signal that supplies the trap potential and feeds it back to the RF signal generator, as shown in Figure 4.11. Inside the Helical Resonator, we use capacitors to divide the amplified voltage and pick up about 1% for the usage of stabilization circuit. An RF power to DC converter is used to generate the corresponding DC voltage while the RF power is fluctuating, and with a PID, the feedback signal is transferred to the RF source, which outputs an amplitude modulated signal.

To note, recently, our group developed this stabilizing scheme with a frequency mixer instead of feeding it back to the RF source. The new scheme can improve the response speed of the feedback system.

第5章　Quantum simulation of molecular electronic structure

The central problem in quantum chemistry and molecular physics is to determine the electronic structure and the ground-state energy of atoms and molecules by solving the quantum many-body equations, which is usually intractable due to the exponential scaling to the size of the system. Quantum simulation[10,12,36–39] can provide the solution for such "exponential catastrophe" problem.

In classical computational chemistry, the coupled-cluster ansatz is one of the most commonly used *ab initio* methods, which is critically limited by its non-unitary nature. The unitary modification as an ideal solution to the problem is, however, extremely inefficient in classical conventional computation. In this chapter, I will provide the first experimental evidence that indeed the unitary version of the coupled cluster ansatz can be reliably performed in the physical quantum system, a trapped ion system. We perform a simulation on the electronic structure of a molecular ion (HeH^+), where the ground-state energy surface curve is probed, energies of excited-states are studied, and the bond-dissociation is simulated non-perturbatively. Our simulation takes advantages from quantum computation to overcome the intrinsic limitations in classical computation, and our experimental results indicate that the method is promising for preparing molecular ground-states for quantum simulation.

Due to the exponential computing resource requirement in the classical calculation of ground state energy problem, several quantum platforms had reported the quantum simulation results of the ground state energy for small molecules[6,40–45]. Here, we follow the theory proposal in Ref. [39], and we are using the Unitary Coupled Cluster (UCC) ansatz, which provides a generic and scalable scheme for generating a parameterized state for the variational method, more importantly, it can be implemented efficiently with quantum devices including trapped ions[46].

5.1　Ground state energy problem

For the ground-state problem, the developments of conventional quantum chemistry can be adopted to quantum computation. In computational chemistry, it has been the center focus to circumvent the problem by approximating the many-body Schrödinger equation and a series of theoretical and numerical methods have been developed.

The key ingredient of quantum molecular simulation consists of (*i*) ground (excited) -state preparation and (*ii*) energy estimation of the corresponding state[10,37]. Recently, the assessed costs for the energy estimation for a well-prepared ground-state in quantum computation have been immensely reduced[13,14,47–49], indicating that chemistry simulation can be one of the main applications of a quantum computer in the near future. However, it is remaining major obstacle to efficiently and reliably find the molecular ground state, which belongs to the class of extremely hard problems called Quantum Merlin Arthur, the quantum analog of NP-hard problem[50,51]. Recently various theoretical schemes for the ground-state problem have been proposed and proof-of-principle experimental demonstrations have been performed including the adiabatic[5,52,53] and algorithmic preparations[54–57].

The Phase Estimation Algorithm, as one of the well-known method for the solution of ground state problem, has been demonstrated in a photonic system[40], a nuclear magnetic resonance system[41], and a nitrogen-vacancy center system[43]. However, this method highly relies on the initially prepared eigenstate, and also need entirely coherent of the system to obtain high precision result[58].

As an alternative solution[9], the variational method, starts with the idea:

$$\frac{\langle \psi(\lambda)| H |\psi(\lambda)\rangle}{\langle \psi(\lambda)|\psi(\lambda)\rangle} \geq E_0 \tag{5-1}$$

Here, H is the Hamiltonian that characterizes the system, $\psi(\lambda)$ is the trial state (ansatz) wave-function with the parameter and E_0 is the smallest eigenvalue of H. As we varies the parameter set of λ, we can reach the minimum value of $\langle \psi(\lambda)| H |\psi(\lambda)\rangle$, thus the ground state wave-function $|\psi(\lambda_0)\rangle$ and ground state energy E_0 are obtained.

As a summarize for the experimental implementation of the variational method for the ground state energy problem, this idea has been done with a photonic system[42], a superconducting system[44], and our trapped ion system[46]. The most recent experiment was performed by the superconducting system with up to six qubits[6].

5.2 Coupled cluster method

Due to challenges in the experimental system, for many experiment demonstrations, the variational ansatz employed in the experimental was "device ansatz", which is device specific method. Here we are using a unitary coupled ansatz, which can be easily extended

to other systems.

The coupled-cluster method is one of the most prominent *ab initio* methods for finding a molecular ground state and it is considered to be the current gold standard[59–62]. In the second quantized representation, the coupled-cluster ansatz is given by the following form: $e^{\hat{T}} |G\rangle$, where $|G\rangle$ is some reference state, such as the Hartree-Fock ground state. The cluster operator $\hat{T} = \hat{T}_1 + \hat{T}_2 + \hat{T}_3 + ...$ is constructed by a sum of particle-hole operators $\hat{T}_n$, where

$$\hat{T}_n \equiv \frac{1}{(n!)^2} \sum_{ijk...,abc...} t_{ijk...}^{abc...} \left\{ \hat{a}^{\dagger}\hat{i}\hat{b}^{\dagger}\hat{j}\hat{c}^{\dagger}\hat{k}... \right\} , \tag{5-2}$$

with $\hat{i}, \hat{j}, \hat{k}, ...$ denotes the fermionic annihilation operators for the occupied orbitals of the reference state $|G\rangle$, $\hat{a}, \hat{b}, \hat{c}, ...$ for the unoccupied orbitals, and $t_{ijk...}^{abc...}$ denote the cluster amplitudes representing the transition amplitudes from $i, j, k...$ orbitals to $a, b, c...$ orbitals. In general, e^T is not unitary and hence the vector norm of the ansatz $e^{\hat{T}} |G\rangle$ is not necessarily conserved. The unitary extension of the coupled-cluster method takes the following form as an ansatz, $e^{\hat{T}-\hat{T}^{\dagger}} |G\rangle$, which preserves the vector norm. The energy $E = \langle G| e^{\hat{T}-\hat{T}^{\dagger}} H e^{\hat{T}-\hat{T}^{\dagger}} |G\rangle$, which is obtained by the unitary coupled-cluster ansatz, is minimized when $\partial E / \partial t_i = 0$ for all t's.

However, the coupled-cluster ansatz is built with the non-unitary operation, which leads to drawbacks such as lacking a variational bound on the ground-state energy[60–64]. The unitary version of the coupled-cluster methods would perfectly resolve the problem, whereas it is classically inefficient without proper truncation of the infinite series expansion. In the classical calculation, the unitary coupled-cluster ansatz can be manually expanded through the Baker-Campbell-Hausdorff expansion, which should be truncated at certain orders for further calculation, since the computational cost to include higher order increases exponentially. The problem of truncating the series expansion is that the truncated operator is no longer unitary, thus loses the advantages of the unitary coupled-cluster method, which provide the variational bound for the ground-state energy.

It has been a long-standing challenge to build an efficient computational scheme for the unitary coupled-cluster (UCC) ansatz. The authors of Refs [39,42] pointed that the UCC ansatz can be efficiently implemented in a quantum computer. In other words, the quantum implementation of the UCC method can outperform the classical computation for the problem of finding molecular ground-state.

The UCC scheme based on the form of the following ansatz

$$|\psi_{\mathrm{UCC}}\rangle = e^{T-T^\dagger}|G\rangle \qquad (5\text{-}3)$$

which apparently provides a solution of the non-Hermitianity problem in the coupled-cluster theory. However, classical implementation of the UCC have intrinsic limitation, e.g., infinite series of the expansion[64]. As a result, all classical applications of UCC involve some type of truncations with potentially uncontrollable errors. On the other hand, the unitary operator, $U \equiv e^{T-T^\dagger}$, can be considered as a time-evolution operator, $i.e.$, $U \equiv e^{-iH_{\mathrm{eff}}}$, driven by an effective Hamiltonian $H_{\mathrm{eff}} \equiv i(T-T^\dagger)$ with a dimensionless time interval set to be 1. Since the time-evolution is efficiently simulated in a quantum system[2], the quantum implementation of the UCC ansatz can reduce the computational cost much less than the classical requirement.

5.3 Classical calculation of HeH$^+$

5.3.1 Born-Oppenheimer approximation

A pictorial description of the molecular HeH$^+$ is shown in Figure 5.1 (a), the molecular HeH$^+$ consists of two nuclei and two electrons. All the following calculations start from the 1s orbit wave-function of Helium atom $\phi_1(r)$ and 1s orbital wave-function of hydrogen atom $\phi_2(r)$, as shown in Figure 5.1 (b).
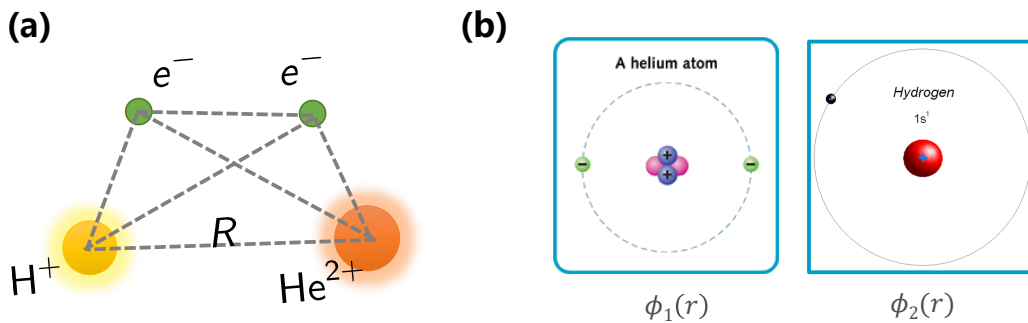

图 5.1　The molecule HeH$^+$. (a) The pictorial description of molecule HeH$^+$, here R is the distance between the two nuclei. (b) The classical calculation basis consists of the 1s orbit wave-function of helium atom and hydrogen atom.

The two-electron Hamiltonian of the molecular ion HeH$^+$ in atomic units, under the Born-Oppenheimer approximation, which assumes that the wave-function of nuclei and

electron can be separated and nuclei kinetic energy can be neglected, has the following form,

$$\hat{H}(\mathbf{R}_{\text{He}}, \mathbf{R}_{\text{H}}) = \sum_{i=1}^{2} \left(-\frac{1}{2}\nabla_i^2 - \frac{2}{|\mathbf{r}_i - \mathbf{R}_{\text{He}}|} - \frac{1}{|\mathbf{r}_i - \mathbf{R}_{\text{H}}|} \right) + \frac{1}{|\mathbf{r}_1 - \mathbf{r}_2|} \ . \tag{5-4}$$

5.3.2　Hartree-Fock process

In quantum chemistry calculation for molecules, expect some simplest molecules like the hydrogen atom, it is essential to introduce the approximation idea to the solution of many-body Schrödinger equation. The Hartree-Fock approximation is typically used as the starting point for more accurate results. The idea of approximation in the Hartree-Fock calculation is to replace the complicated many-electron problem by a one-electron problem in which electron-electron repulsion is treated in an average way, The procedure for solving the Hartree-Fock equation is called the self-consistent-field (SCF) method[65]. The Mathematica code for the calculation is in Appendix C.

During the calculation of Hartree-Fock process, we use the minimal STO-3G basis, which approximates the 1s orbits wave-functions (Slater-type orbitals) with three Gaussian functions, as follows

$$\sqrt{\frac{\xi^3}{\pi}}e^{-\xi r} \doteq c_1(\frac{2e_1}{\pi})^{3/4}e^{-e_1 r^2} + c_2(\frac{2e_2}{\pi})^{3/4}e^{-e_2 r^2} + c_3(\frac{2e_3}{\pi})^{3/4}e^{-e_3 r^2} \tag{5-5}$$

Under the calculation basis $\phi_1(r), \phi_2(r)$, we can calculate the physical operator (kinetic energy, potential energy) according to the self-consistent-field theory. we calculate one electron in the mean field generated by other 3 particles, we define the core Hamiltonian (not include the electron-electron interaction part) as H_{core}

$$H_{\text{core}} = \left(-\frac{1}{2}\nabla_i^2 - \frac{2}{|\mathbf{r}_i - \mathbf{R}_{\text{He}}|} - \frac{1}{|\mathbf{r}_i - \mathbf{R}_{\text{H}}|} \right) \tag{5-6}$$

Another prepare work is finding a transfer matrix that makes an orthogonal-normalized basis. Here, we followed the canonical process, the first step is calculating the direct inner-product matrix $S = \begin{pmatrix} \langle\phi_1(r)\,|\,\phi_1(r)\rangle & \langle\phi_1(r)\,|\,\phi_2(r)\rangle \\ \langle\phi_2(r)\,|\,\phi_1(r)\rangle & \langle\phi_2(r)\,|\,\phi_2(r)\rangle \end{pmatrix}$, then the basis transfer matrix can be written as $X_0 = \begin{pmatrix} 1/\sqrt{2} & 1/\sqrt{2} \\ 1/\sqrt{2} & -1/\sqrt{2} \end{pmatrix} \cdot \begin{pmatrix} \sqrt{1+S_{12}} & 0 \\ 0 & \sqrt{1-S_{12}} \end{pmatrix}$. To note the electron-

electron interaction, we introduced a simplified notation as

$$\langle \mu\nu|\lambda\sigma\rangle \doteq \langle \phi_\mu(r)\phi_\nu(r)|\phi_\lambda(r)\phi_\sigma(r)\rangle$$

Now comes to the iteration process, shown in Figure 5.2. We start with the core Hamiltonian H_{core}, then we calculate the new operator under the basis transfer matrix X_0, $F_{i,s} = X_0^\dagger.F_i.X_0$. From the process of diagonalizing the matrix $F_{i,s}$, we can get another transfer matrix C_i (which is consist of the eigenvector of $F_{i,s}$). After that, we obtain the total transfer matrix $TC_i = X_0.C_i$ (it is also known as an orthogonal normalize matrix). The electron charge density distribution matrix is $P_i(\mu,\nu) = 2\Sigma_a^{N/2}TC_{i\mu,a}TC_{i\nu,a}^*$, $G_i(\mu,\nu) = \Sigma_{\lambda,\sigma}P_i(\lambda,\sigma)(\langle\mu\nu|\sigma\lambda\rangle - \frac{1}{2}\langle\mu\lambda|\sigma\nu\rangle)$. Then we have the final updated Fock operator as $F'_{i+1} = F_i + G_i$. The termination check of the iteration is $F'_{i+1}? = F_i$, if it is not converged yet ,we will update the F_i, otherwise terminate with the output result

$$E_{tot} = \frac{2}{R} + \Sigma_\mu\Sigma_\nu P(\mu,\nu)(H_{core}(\mu,\nu) + F(\mu,\nu)) \tag{5-7}$$
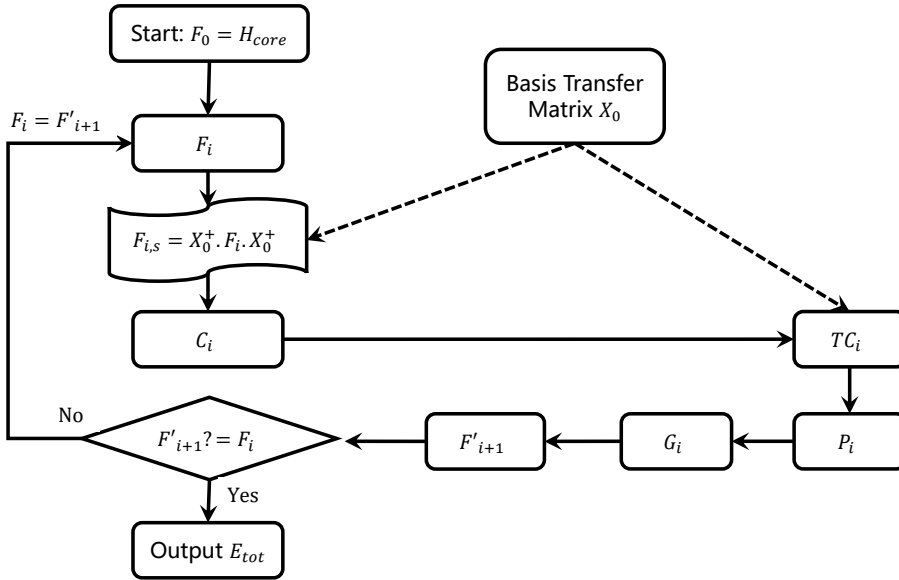

图 5.2　Self-Consistent-Field process

After the above Self-Consistent-Field process, we get the final orthogonal normalized transfer matrix TC_{final}, within this we achieved the Hartree-Fock space orbit wave-

function for the molecule HeH$^+$: $\begin{pmatrix} \phi_1'(r) \\ \phi_2'(r) \end{pmatrix} = TC_{final} \cdot \begin{pmatrix} \phi_1(r) \\ \phi_2(r) \end{pmatrix}$. This is called as the Hartree-Fock independent particle orbit wavefcuntion. which is shown in Figure 5.3
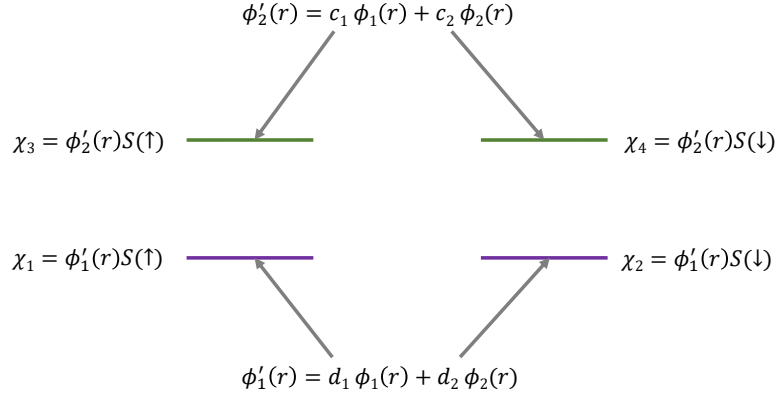

图 5.3 The orthogonal basis obtained by the Hartree-Fock process.

5.3.3 Second quantization process

After Hartree-Fock process, the Hartree-Fock ground state and two independent spatial orbitals $\phi_1'(r)$, $\phi_2'(r)$ are achieved. The electron is an elementary fermion with spin 1/2 which obeys the Pauli exclusion principle. Consider the spin together with the space orbit wave-function, and we have the following configuration. Considering the electron's spin together with the two space orbit wave-function ($\phi'(r) \otimes spin$), we note as $\chi_{p(q,r,s)}(r)$, where p, q, r, s can be 1, 2, 3, 4 represent for $\{1 \uparrow\}, \{1 \downarrow\}, \{2 \uparrow\}, \{2 \downarrow\}$, The second quantized Hamiltonian can be write down as

$$H(R) = \sum_{pq} h_{pq}(R)\hat{a}_p^\dagger \hat{a}_q + \frac{1}{2} \sum_{pqrs} h_{pqrs}(R)\hat{a}_p^\dagger \hat{a}_q^\dagger \hat{a}_r \hat{a}_s \tag{5-8}$$

where

$$h_{pq} = \int dr \chi_p(\vec{r})^*(-\frac{1}{2}\nabla_e^2 - \sum_a \frac{Z_a}{|\vec{r}_a - \vec{r}|})\chi_q(\vec{r})$$

$$h_{pqrs} = \int d\vec{r}_1 d\vec{r}_2 \frac{\chi_p(\vec{r}_1)^* \chi_q(\vec{r}_2)^* \chi_r(\vec{r}_1)\chi_s(\vec{r}_2)}{|\vec{r}_1 - \vec{r}_2|}$$

As shown Eq. (5-8), $h_{pq}(R)$ and $h_{pqrs}(R)$ are related to one electron and two electron transitions, respectively and the index p, q, r, s stands for the four possible states in our

Hilbert space. The terms of $h_{pq}(R)$ and $h_{pqrs}(R)$ are computed numerically with the scaling of $O(M^4)$, where M is the number of molecular orbits. The creation and annihilation operators in the Hamiltonian (5-8) are mapped to spin Pauli operators by performing the Jordan-Wigner transformation and pairs of Pauli operators are mapped to four-level systems. After the mapping, the Hartree-Fock basis for HeH$^+$ consists of the following set of four states, $\{|G\rangle, |E_{11}\rangle, |E_{12}\rangle, |E_2\rangle\}$ as shown in Figure 5.5(a).

5.4 Trapped ion implementation of the unitary coupled cluster
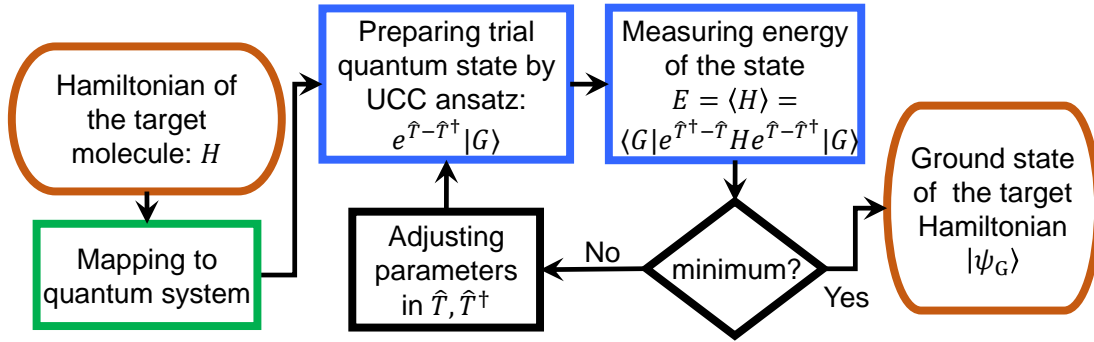
5.4.1 Experimental implementation procedure

图 5.4 The implementation procedure of the UCC algorithm in a quantum system.

The whole procedure of finding the ground state of a target molecule is shown in Figure 5.4, which is also discussed in Refs [39,42]. After efficiently preparing a trial state with UCC ansatz in a quantum system that maps the classical basis set of the target molecule, we measure the average energy of the state. The preparation of the UCC ansatz and the energy measurement are performed in the quantum system. Based on a classical feedback algorithm, we adjust the parameters, $i.e.$, the cluster amplitudes of the UCC ansatz. We repeat the quantum process of preparation and measurement until we find the variational minimum of the target Hamiltonian.

5.4.2 Mapping of HeH$^+$ on ^{171}Yb$^+$ ion

The electron excitation operators, which excite the electrons out of the Hartree-Fock ground state, up to two electron excitations are given by,

$$T_1 = t_{11}a_{2\downarrow}^{\dagger}a_{1\downarrow} + t_{12}a_{2\uparrow}^{\dagger}a_{1\uparrow}, \ T_2 = t_2 a_{2\downarrow}^{\dagger}a_{2\uparrow}^{\dagger}a_{1\uparrow}a_{1\downarrow} \tag{5-9}$$
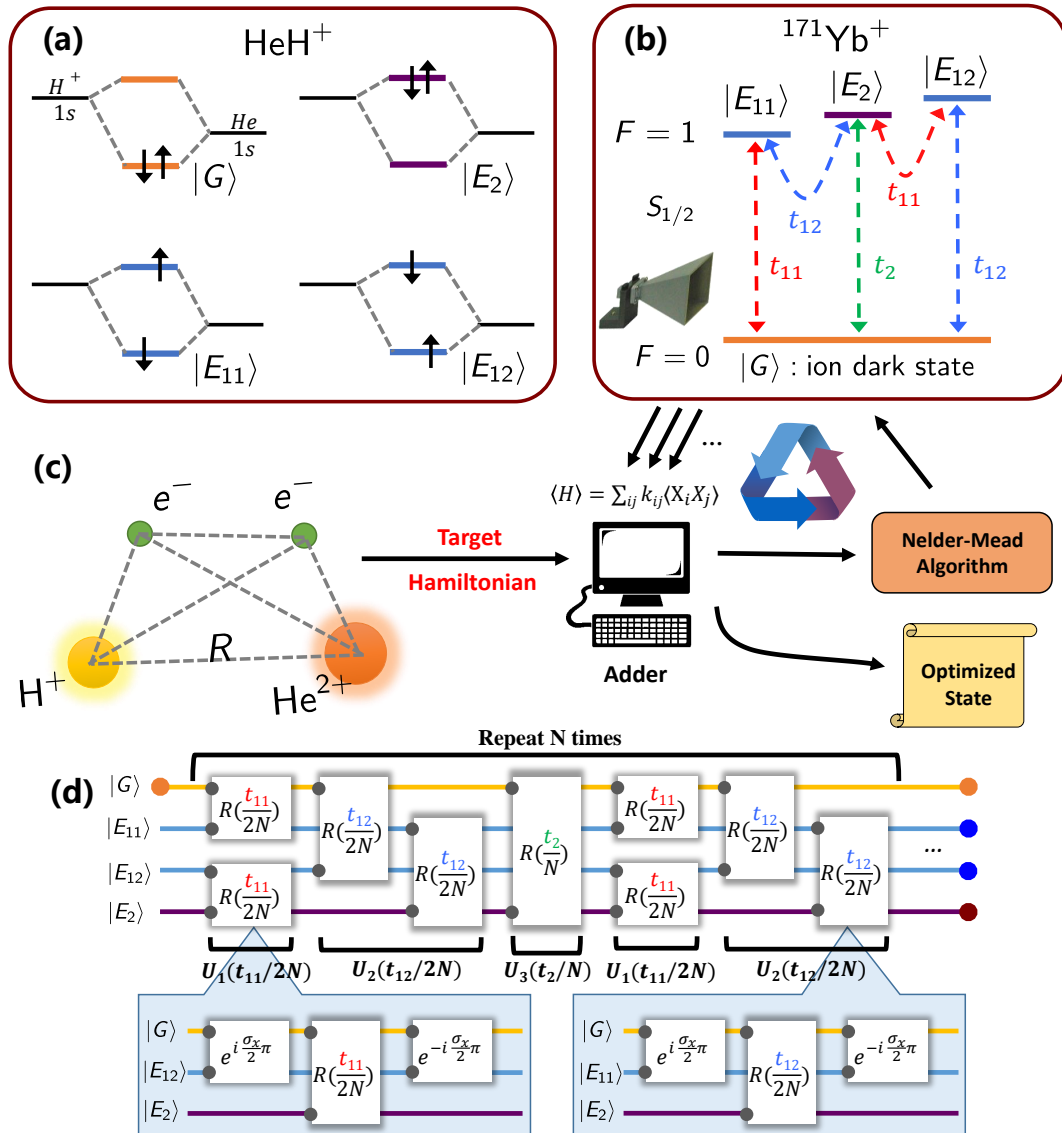
图 5.5 Implementation of the Unitary coupled Cluster in the trapped ion system. (a) The Hartree-Fock basis states of the target molecule, HeH^+. (b) The mapping of the basis states on the energy levels of $^{171}Yb^+$ including cluster amplitudes t_{11}, t_{12}, and t_2, which are controlled by the duration of microwave pulses. (c) The classical minimum search algorithm supports the finding of ground state energy. (d) The microwave pulse sequence for the preparation of the UCC ansatz. The effective time evolution operator $e^{T-T^\dagger}$ is expanded by the Suzuki-Trotter scheme.

Note that all the terms are spin preserving, and the t_{11}, t_{12}, t_2 are in general complex numbers to be determined by an optimization process. After the same mapping process of the Hamiltonian (5-8), the effective Hamiltonian $H_{\text{eff}} \equiv i(T - T^\dagger)$ can be decomposed into three parts: $\hat{H}_{\text{eff}} = \hat{H}_1 + \hat{H}_2 + \hat{H}_3$, where

$$
\begin{aligned}
\hat{H}_1(t_{11}) &= it_{11}\left(|E_{11}\rangle\langle G| + |E_2\rangle\langle E_{12}|\right) + \text{h.c.} \\
\hat{H}_2(t_{12}) &= it_{12}\left(|E_{12}\rangle\langle G| + |E_2\rangle\langle E_{11}|\right) + \text{h.c.} \\
\hat{H}_3(t_2) &= it_2|E_2\rangle\langle G| + \text{h.c.}
\end{aligned}
\tag{5-10}
$$

We realize the effective Hamiltonian H_{eff} in a quantum system of multiple energy levels in trapped $^{171}\text{Yb}^+$ ion. As shown in Figure 5.5(b), four energy levels in the ground-state manifold of $^2S_{1/2}$ of the $^{171}\text{Yb}^+$ are employed[66,67] to map the basis state as $|F = 0, m_F = 0\rangle \equiv |G\rangle$ and $|F = 1, m_F = -1, 1, 0\rangle \equiv \{|E_{11}\rangle, |E_{12}\rangle, |E_2\rangle\}$, which are separated by $\omega_{\text{HF}} - \omega_z$, $\omega_{\text{HF}} + \omega_z$ and ω_{HF}, where the hyper-fine splitting of $\omega_{\text{HF}} = (2\pi)\,12.642821\text{GHz}$, Zeeman splitting of $\omega_z = (2\pi)\,13.586\text{MHz}$ with the static magnetic field of $B = 9.694\text{G}$.

5.4.3 Microwave implementation for the time evolution operator

The unitary operator $U \equiv e^{-iH_{\text{eff}}}$ is implemented as a time evolution of the system with the effective Hamiltonian H_{eff} as shown in Figure 5.5(d). The initialization of the state to $|G\rangle$ is performed by the standard optical pumping technique. The transitions $\{|G\rangle \leftrightarrow |E_{11}\rangle, |G\rangle \leftrightarrow |E_{12}\rangle, |G\rangle \leftrightarrow |E_2\rangle\}$ are implemented by applying resonant microwaves. The other transitions $\{|E_{11}\rangle \leftrightarrow |E_2\rangle, |E_{12}\rangle \leftrightarrow |E_2\rangle\}$ are achieved by applying composite pulse sequences shown in the insets of Figure 5.5(d). Consequently, the experimental implementation of the unitary operator U is achieved by the sequence depicted in Figure 5.5(d), which results from the second-order Suzuki-Trotter expansion.

The corresponding unitary transformation is labeled as $U_i(\alpha) = e^{-iH_i(\alpha)\tau}$ for $\tau = 1$, which forms the elements in the Suzuki-Trotter expansion for $e^{T-T^\dagger}$, i.e.,

$$
e^{\hat{T}-\hat{T}^\dagger} = \left[\hat{U}_1\left(\frac{t_{11}}{2N}\right)\hat{U}_2\left(\frac{t_{12}}{2N}\right)\hat{U}_3\left(\frac{t_2}{N}\right)\hat{U}_1\left(\frac{t_{11}}{2N}\right)\hat{U}_2\left(\frac{t_{12}}{2N}\right)\right]^N + \hat{O}\left(1/N^3\right).
$$

$$
\hat{U}_1\left(\frac{t_{11}}{2N}\right) = e^{-i\left(\frac{t_{11}}{2N}(|E_{11}\rangle\langle G|+|E_2\rangle\langle E_{12}|)+\text{h.c.}\right)}
$$

$$
\hat{U}_2\left(\frac{t_{12}}{2N}\right) = e^{-i\left(\frac{t_{12}}{2N}(|E_{12}\rangle\langle G|+|E_2\rangle\langle E_{11}|)+\text{h.c.}\right)}
$$

$$\hat{U}_3\left(\frac{t_2}{N}\right) = e^{-i\left(\frac{t_2}{N}|E_2\rangle\langle G|+\text{h.c.}\right)} \tag{5-11}$$

where We set $N = 2$ in most of our experimental simulations.

The transformations of $\hat{U}_1$, $\hat{U}_2$ and $\hat{U}_3$, the terms of $e^{-i\left(\frac{t_{11}}{2N}|E_{11}\rangle\langle G|+\text{h.c.}\right)}$, $e^{-i\left(\frac{t_{12}}{2N}|E_{12}\rangle\langle G|+\text{h.c.}\right)}$, and $e^{-i\left(\frac{t_2}{2N}|E_2\rangle\langle G|+\text{h.c.}\right)}$ are implemented by the direct microwave transitions with the frequencies of $\omega_{\text{HF}} - \omega_Z$, ω_{HF}, and $\omega_{\text{HF}} + \omega_Z$. The transformations of $e^{-i\left(\frac{t_{12}(t_{11})}{2N}|E_2\rangle\langle E_{11}(E_{12})|+\text{h.c.}\right)}$ are decomposed by the three direct pulses of $e^{-i\frac{\pi}{2}\hat{\sigma}_x^{\{E_2,G\}}} e^{-i\left(\frac{t_{12}(t_{11})}{2N}|E_{11}(E_{12})\rangle\langle G|+\text{h.c.}\right)} e^{i\frac{\pi}{2}\hat{\sigma}_x^{\{E_2,G\}}}$ for the implementations, where $\hat{\sigma}_x^{\{E_2,G\}} = |E_2\rangle\langle G| + \text{h.c.}$.

Then the UCC amplitudes are represented by the multiplication of relevant Rabi frequency and time. Since the UCC amplitudes t_{11}, t_{12} and t_2 are much smaller than 1, which corresponds to much less than the π pulse of microwaves, the errors from small Trotter expansion, N=2 in our demonstration, are negligible.

5.4.4　Construction of the ansatz state energy

We can obtain the energy $\langle H \rangle = \sum_{pq}\langle H_{pq}\rangle + \sum_{pqrs}\langle H_{pqrs}\rangle$, where $H_{pq} = h_{pq}\hat{a}_p^\dagger\hat{a}_q$ and $H_{pqrs} = h_{pqrs}\hat{a}_p^\dagger\hat{a}_q^\dagger\hat{a}_r\hat{a}_s$, by term-by-term measurements and addition of all of them in the target Hamiltonian (5-8).

In the experiments, we consider the situation that includes two electrons of different spins at the ground $1s$ orbit of Helium or Hydrogen, which can be described by the 4×4 Hamiltonian. Labeling the many-body energy levels as $1, 2, 3, 4$, the explicit matrix form of the Hamiltonian is given by

$$\hat{H} = \begin{bmatrix} h_{11} + h_{22} + h_{1212} & h_{42} + h_{4121} & h_{31} + h_{3212} & h_{4321} \\ h_{24} + h_{2141} & h_{11} + h_{44} + h_{1414} & h_{2341} & h_{31} + h_{3414} \\ h_{13} + h_{1232} & h_{1432} & h_{22} + h_{33} + h_{2323} & h_{42} + h_{4323} \\ h_{1234} & h_{13} + h_{4143} & h_{24} + h_{2343} & h_{33} + h_{44} + h_{3434} \end{bmatrix} \tag{5-12}$$

For the experimental measurement, this matrix is expanded by the Pauli basis, i.e., $\langle \hat{H} \rangle = \sum_{i,j} k_{ij}\langle \hat{X}_i\hat{X}_j \rangle$, where $\hat{X}_i \in \{\hat{I}, \hat{\sigma}_x, \hat{\sigma}_y, \hat{\sigma}_z\}$. This procedure works for small systems, as the number of measurements will scale exponentially. In general, for large systems, one can keep a polynomial number of measurements by performing the Jordan-

Wigner transformation,

$$\hat{a}_j \rightarrow \hat{I}^{\otimes j-1} \otimes \hat{\sigma}_+ \otimes \hat{\sigma}_z^{\otimes N-j} \quad , \quad \hat{a}_j^\dagger \rightarrow \hat{I}^{\otimes j-1} \otimes \hat{\sigma}_- \otimes \hat{\sigma}_z^{\otimes N-j} , \qquad (5\text{-}13)$$

to the second-quantized Hamiltonian in (5-12).

The energy $\langle H \rangle$ of the UCC ansatz state can be obtained by the addition of the results of term-by-term measurements, $\sum_{pq} \langle H_{pq} \rangle + \sum_{pqrs} \langle H_{pqrs} \rangle$. Here, we take $\langle H_{11} \rangle$ as an example:

$$\langle H_{11} \rangle = \langle h_{11} \hat{a}_1^\dagger \hat{a}_1 \rangle = \mathrm{Tr}\left(\rho_{\mathrm{UCC}}^{\mathrm{exp}} \begin{bmatrix} h_{11} & 0 & 0 & 0 \\ 0 & h_{11} & 0 & 0 \\ 0 & 0 & 0 & 0 \\ 0 & 0 & 0 & 0 \end{bmatrix} \right) = h_{11} (\rho_{11} + \rho_{22})$$

The total number of term-by-term measurements is the same as the total number of non-zero terms of h_{pq}, h_{pqrs}, which is 24 for our simulation. In fact, since there is no zero component in the Hamiltonian (5-12), we need the information of all the components of the density matrix of the UCC ansatz, which requires 15 times of measurements with the normalization condition. In our small-scale simulation, therefore, the full quantum state tomography is more efficient than the term-by-term measurements due to the redundancy. In our experiment, we obtain the energy by the quantum state tomography of the density matrix. It is equivalent to the term-by-term measurement in our scale measurements since we can use the information of all components of the density matrix for the term-by-term method.

Note that as the system size increases, we do not need the full knowledge of the density matrix of the state for the energy measurement, since the number of terms in the Hamiltonian (5-8) scales polynomially[39,42]. Since we need the full knowledge of the density matrix for our small-scale simulation, we reconstruct the full density matrix $\rho_{\mathrm{UCC}}^{\mathrm{exp}}$ by the standard quantum state tomography, which requires 15 times of measurement, and obtain the energy by $Tr\left(\rho_{\mathrm{UCC}}^{\mathrm{exp}} H \right)$. For the relevant components of the density matrix, we repeat the standard measurements up to 1000 times, which give 3.2% projection uncertainty of standard deviation. We also note that since the number of independent terms in the Hamiltonian increases polynomially as $O(M^4)$, where M is the number of orbitals, for the large size of a molecule, the term-by-term construction of energy is

much more efficient than the quantum state tomography of the density matrix. Up to $M = 4$, however, there is no essential difference in energy measurement between by the full quantum state tomography and by term-by-term methods.

5.4.5　Unitary coupled cluster parameters searching process

The energy functional derived from the UCC ansatz in the minimum basis set of the HeH$^+$ involves three complex parameters, *i.e.* t_{11}, t_{12}, and t_2, which are equivalent to six real parameters. It can be shown that in the weak excitation regime, the energy functional is minimized when $t_{11} = t_{12} \equiv t \in \mathbb{R}$. First of all, the electron excitation operator in Eq. (5-9) should be optimized with $t_{11} = t_{12}$ to maintain the spin-flip symmetry, since the model Hamiltonian (5-8) is spin independent.

The matrix form of the second quantized Hamiltonian $\hat{H}(R)$ in the Hatree-Fock basis (5-12) is a real symmetric matrix, and the off-diagonal terms are small compared to the diagonal terms as long as the Hartree-Fock approximation is valid. The contributions from the real and imaginary part of the parameters in the energy function can be separated up to the second order, thus the energy functional can be formally written as follows,

$$E(t_{11}, t_{12}, t_2) = E_g^{\text{HF}} + \Delta E_r(\mathfrak{R}[t_{11}], \mathfrak{R}[t_{12}], \mathfrak{R}[t_2]) + \Delta E_i(\mathfrak{I}[t_{11}], \mathfrak{I}[t_{12}], \mathfrak{I}[t_2]) \quad (5\text{-}14)$$

where $\mathfrak{R}[\cdot]$ and $\mathfrak{I}[\cdot]$ represent the real and imaginary parts of a complex parameter. Note that $\Delta E_r(\cdot)$ and $\Delta E_i(\cdot)$, depending on independent variational parameters, can be minimized separately. We focusing on the contribution of the imaginary parts of the variational parameters, *i.e.* $\Delta E_i(\cdot)$, which up to the second order can be proofed to non-negative as follows,

$$
\begin{aligned}
\Delta E_i &= \mathfrak{I}[t_{11}]^2 \Delta_{11} + \mathfrak{I}[t_{12}]^2 \Delta_{12} + \mathfrak{I}[t_2]^2 \Delta_2 \\
&\quad + 2\mathfrak{I}[t_{11}]\mathfrak{I}[t_{12}]H_{11,12} + 2\mathfrak{I}[t_{11}]\mathfrak{I}[t_2]H_{11,2} + 2\mathfrak{I}[t_{12}]\mathfrak{I}[t_2]H_{12,2} \\
&\geq |\mathfrak{I}[t_{11}]\mathfrak{I}[t_{12}]|\left(\Delta_0 - |H_{11,12}|\right) \\
&\quad + |\mathfrak{I}[t_{11}]\mathfrak{I}[t_2]|\left(\Delta_0 - |H_{11,2}|\right) + |\text{Im}[t_{12}]\mathfrak{I}[t_2]|\left(\Delta_0 - |H_{12,2}|\right) \\
&\geq 0 \qquad\qquad\qquad\qquad\qquad\qquad\qquad\qquad\qquad\qquad (5\text{-}15)
\end{aligned}
$$

where $\Delta_s \equiv E_s^{\text{HF}} - E_g^{\text{HF}}$ is the Hatree-Fock excitation energies, $\Delta_0 = \text{Min}(\Delta_{11}, \Delta_{12}, \Delta_2)$ is the minimum Hatree-Fock excitation energy, and $H_{s,s'} \equiv \langle E_s | \hat{H}(R) | E_{s'} \rangle$ the off-diagonal

terms in the matrix form (5-12), with the subscripts s and s' running over the Hatree-Fock excited states. In deriving the last inequality, we utilize the fact that $\Delta_0 \ll |H_{s,s'}|$. The inequality $\Delta E_i \gg 0$ holds when at least two out of the three variational parameters are zero, so $(\Im[t_{11}], \Im[t_{12}], \Im[t_2]) = (0, 0, 0)$ actually minimize the energy functional.

The preparation and the measurement of the UCC ansatz are performed in the quantum system and the minimization process is supported by the classical algorithm. The measured value of $\langle H \rangle$ for the prepared UCC ansatz is taken as an input for a classical optimization algorithm, which compares it to the previous values and suggests a new set of $\{t_{11}, t_{12}, t_2\}$ so that the same procedure is repeated until the resulting $\langle H \rangle$ converges to some value. As a result, we obtain an optimized state with minimal energy for approximating the ground state of HeH$^+$ in the form of the UCC ansatz in Eq. (5-3). In our realization, we use a popular Nelder-Mead minimum search algorithm[68].

Figure 5.6 shows an instance of the energy optimization process, when the nuclei separation of HeH$^+$ is fixed to be $R = 1.7$ $a.u.$. Note that throughout the paper, the atomic unit ($a.u.$) is used. The algorithm is capable of finding the minimum energy and state in around hundred iterations with the full six-parameter simulations as shown in Figure 5.6(a). About twice fewer iterations shown in Figure 5.6(b) can be achieved with an ansatz simplified to contain two parameters. Since both cases provide equivalent results, we focus on the two-parameter ansatz in the following discussion. Figures 5.6(c)(d) show the typical search of minimum energy by the classical Nelder-Mead algorithm with two parameters.

5.5　Experimental results

In this section, we report the first experimental realization of the UCC ansatz with a minimal basis, based on quantum simulation in a multi-level of a trapped ^{171}Yb$^+$ ion. We simulate the electronic structure of a molecular ion (HeH$^+$)[42,43] and reliably find the molecular ground-state as well as the corresponding energy by the UCC ansatz and the variational method, which can be considered as an alternative method for the energy estimation[40]. Moreover, we apply the quantum UCC method to compute excited states and chemical-bond softening non-perturbatively.
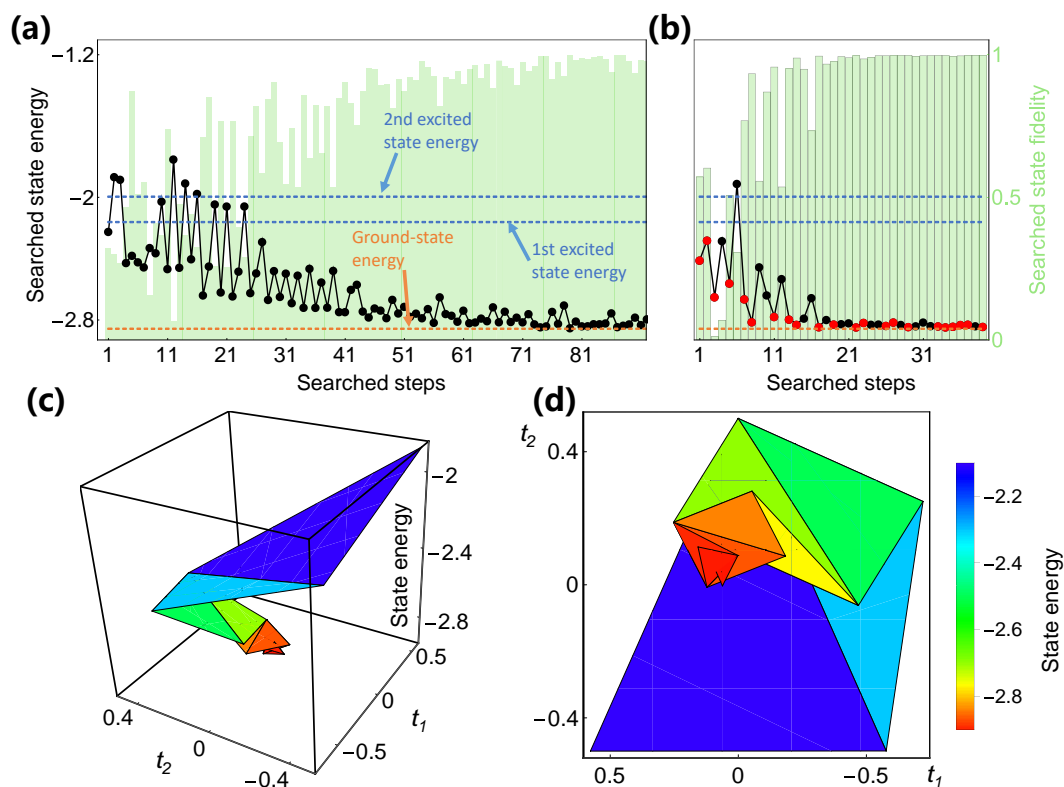
图 5.6 The search process of the minimum energy at $R = 1.7 a.u.$ assisted by the classical Nelder-Mead algorithm with UCC ansatz. The measured energy $\langle H \rangle$ (dots) and the fidelity of the prepared state (bars) to the ideal ground state depending on the number of iterations (a) with full six parameters and (b) with two parameters. For both cases, the algorithm converges to the ground-state energy obtained by the exact diagonalization with the decent fidelity of the state. Red dots show the successful steps that contribute to the convergence. (c) The side view and (d) the bottom view of the searching process with two parameters for the successful steps. The atomic unit ($a.u.$) is used for the energy through all the figures.

5.5.1 Ground state energy of HeH$^+$

Figure 5.7 shows the energy curve of the ground state of HeH$^+$ depending on the nuclear distance R, where each point is obtained by the procedure of Figure 5.6. The experimental data are in agreement with the energy (orange line) calculated by the exact diagonalization of the full matrix of Hamiltonian (5-8) within the error bars. From the energy curve, the equilibrium distance between the nuclei is located at $R = 1.73 a.u.$ with the corresponding energy of $E = -2.86 \pm 0.05 \ a.u.$.
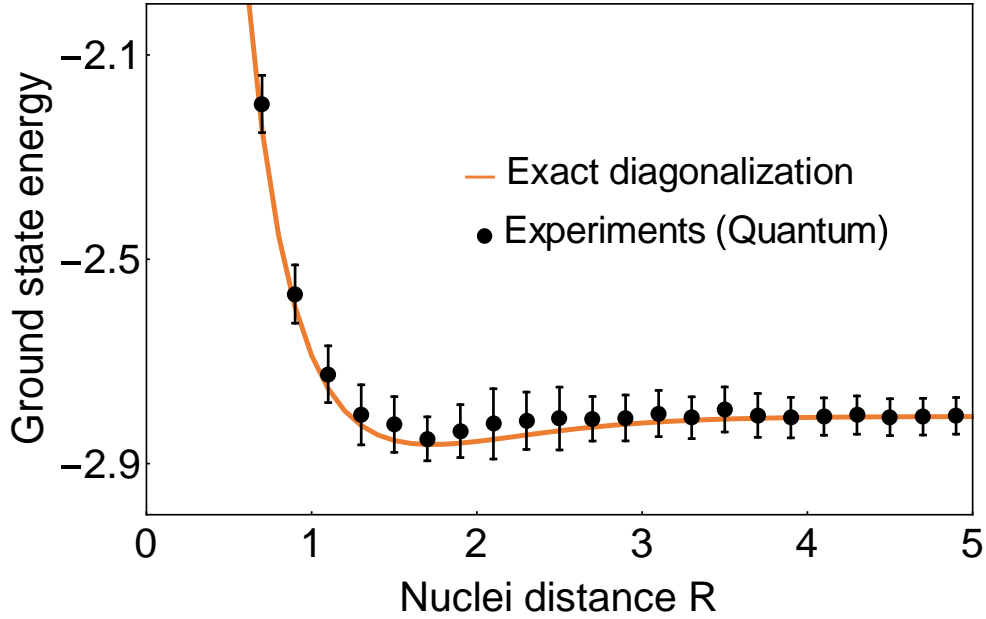
图 5.7　The ground state energy of HeH$^+$ depending on the inter-nuclei distance R. The error-bars of the experimental data mainly come from the quantum projection noise of 1000 repetitions for each term of the Hamiltonian (5-8).

5.5.2　The Electric field effect on HeH$^+$

Furthermore, the same procedure can be used to study the non-perturbative behaviors of the HeH$^+$ molecular ion under strong electric field with the new target Hamiltonian including the effect of the electric field as $\mathbf{E} \cdot (\mathbf{r}_1 + \mathbf{r}_2) - \mathbf{E} \cdot (2\mathbf{R}_{\mathrm{He}} + \mathbf{R}_{\mathrm{H}})$. Figure 5.8(a) shows the phenomenon of chemical-bond softening of HeH$^+$ (at $R = 1.7$ $a.u.$) as the strength of the electric field increases, which eventually leads to a dissociation of the molecular ions[69]. We compare our non-perturbative results with those obtained through the first-order and second-order perturbation theories shown in Figure 5.8(b).

To evaluate the molecule property under the static electric field, we need to recalculate the new orthogonal normalized basis $\phi'_1(r)$, $\phi'_2(r)$ through the Hartree-Fock process and get the matrix representation of the second quantization Hamiltonian. The system's Hamiltonian under static electric field takes following form

$$\hat{H}_{elec} = \sum_{i=1}^{2} \left(-\frac{1}{2}\nabla_i^2 - \frac{2}{|\mathbf{r}_i - \mathbf{R}_{\mathrm{He}}|} - \frac{1}{|\mathbf{r}_i - \mathbf{R}_{\mathrm{H}}|} \right) + \frac{1}{|\mathbf{r}_1 - \mathbf{r}_2|} + \mathbf{E} \cdot (\mathbf{r}_1 + \mathbf{r}_2) - \mathbf{E} \cdot (2\mathbf{R}_{\mathrm{He}} + \mathbf{R}_{\mathrm{H}})$$

(5-16)

Then, we take second quantization Hamiltonian as a new "Target Hamiltonian". By combining quantum computer with classical computer (UCC process), the ground state

of $\hat{H}_{elec}$ is resolved. For the perturbation theory with $\hat{H}_{elec} = \hat{H}_0 + \lambda V$, we use $\hat{H}_0 = \hat{H}(\mathbf{R}_{He}, \mathbf{R}_H)$ and $\lambda = |\mathbf{E}|$, $V = \epsilon \cdot (\mathbf{r}_1 + \mathbf{r}_2) - \epsilon \cdot (2\mathbf{R}_{He} + \mathbf{R}_H)$, where $\epsilon = \mathbf{E}/|\mathbf{E}|$.
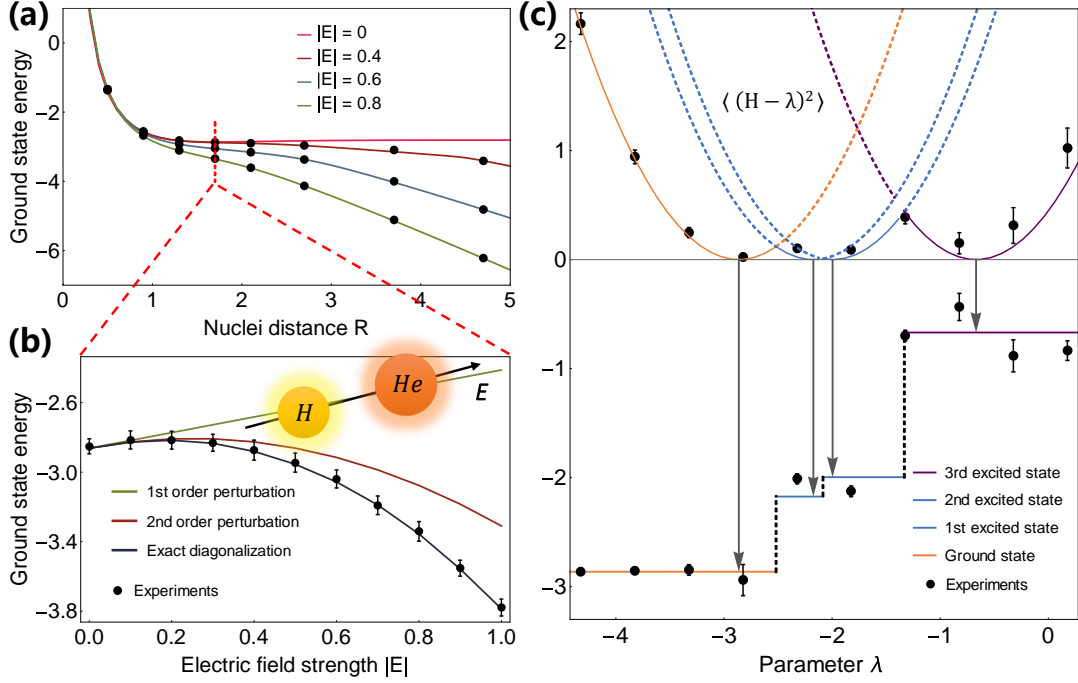

图 5.8 Applications of the UCC simulation. (a) The ground state energy of HeH$^+$ subject to a static electric field along the nuclei axis for different strengths. (b) The comparison between the UCC quantum simulation and the perturbation theory at given inter-nucleus distance $R = 1.7a.u.$. (c) The search process of the energies of excited states of H by finding the ground-state energy of the Hamiltonian $(H - \lambda)^2$ by scanning the values of λ. When λ is the energy of an excited state, the experimental minimum value of $\langle (H - \lambda)^2 \rangle$ tends to be zero. We also can calculate the excited-state energy from other non-zero values of $\langle (H - \lambda)^2 \rangle$. If λ is on the left (right) side of the excited energy, the positive (negative) solution of $E_{\text{meas}} = \langle (H - \lambda)^2 \rangle$ provides the excited energy.

5.5.3 Excited states energy of HeH$^+$

We also study the excited states of H by changing the target Hamiltonian to $(H - \lambda)^2$, where λ is a parameter close to the energy of an excited state, which turns the excited state of H into the ground state of $(H - \lambda)^2$. In the experiment, we uniformly scan the values of λ and apply the same UCC procedure to find the minimum energy in a given λ. As shown in Figure 5.8(c), we observe that the required precision for the computation of excited states should be much higher than the separation of the energies. In the current limited system, we obtain the energy of the highest excitation that has relatively large energy gap to other states but the rest of them are not well resolved.

To obtain the excited states energy, the reconstructed Hamiltonian $(H - \lambda)^2$ is needed. We can see the eigenstate of H is also the eigenstate of $(H - \lambda)^2$, for eigenstate $H |E_i\rangle = E_i |E_i\rangle$

$$\langle E_i| H |E_i\rangle = E_i$$
$$\langle E_i| (H - \lambda)^2 |E_i\rangle = (E_i - \lambda)^2 \tag{5-17}$$

When we scan the parameter λ, the searched state energy of $(H - \lambda)^2$ is quadratic function of the variable λ, as is shown in Figure 5.8(c). When the minimal state energy of $(H - \lambda)^2$ is searched, λ is the eigenstate energy of H. In the algorithm, we manually scan all the possible value of λ. When searched state energy is near to 0, it indicates λ is close to the eigenstate energy of H, which could be a ground state or excited state.

5.6 Discussion and conclusions

Our current realization is capable of simulating any molecule up to four electronic levels with a single ion. In general, a molecule of N electrons system in M molecular orbitals ($M \geq N$) can be implemented with M qubits system or $M/2$ qudits, four-level systems shown in our realization, through the Jordan-Wigner transformation and four-level mapping. For the UCC implementation with M qubit system, it requires the simulation of time-evolution of M-body interaction, which is equivalent to the nonlocal product of M Pauli operators. The simulation of such M-body interaction, which is the most challenging operation in the UCC protocol, can be performed by applying $2M$ times of CNOT-gate or 2 times of the multi-particle Mølmer-Sørensen gates[39,70,71]. The measurement of M-qubit Hamiltonian with the $O(M^4)$ terms has been already well established in the trapped ion system. For the $M/2$-qudit Hamiltonian, we can simply use the same measurement scheme used in our experimental demonstration. The UCC scheme for the trapped ions can be applied to other physical platforms[3,38,72].

We emphasize the computational complexity of the quantum implementation of the UCC method scales polynomially with the number of orbitals M. Including the maximum excitation up to k, each cluster operator contains k creation operators and k annihilation operators. For a total of M orbital modes, therefore, we have a total of $O(M^{(2k)})$ terms. After the Jordan-Wigner transformation, the fermionic operators are mapped into spin operators, which requires $O(M)$ operations. The total number of scaling

as the number of molecular orbits M is $O(M^{(2k+1)})$. Moreover, the time evolutions and the measurements in our UCC implementation allow parallel computation[39,42], which boosts the performance. Our experimental realization of UCC method opens a new dimension of quantum simulation and offers a solution for the classical coupled-cluster methods. We note that some of other current developments and understandings in the coupled-cluster schemes could be adapted in quantum UCC scheme. Moreover, our UCC scheme could be applied to other large eigenvalue problems in network search algorithm and condensed matter physics.

第6章　Quantum emulation of molecular vibronic spectroscopy

Molecules are one of the most demanding quantum systems to be simulated by quantum computers because of their complexity and the emergent role of quantum nature. Recently, it has been suggested that Gaussian boson sampling[73,74] can simulate molecular spectroscopy: this particular problem is also expected to reveal the excellence of the quantum computing[75,76]. In this chapter, I will present the first quantum device that generates the molecular spectroscopic signal of SO_2 as an example, with phonons in a trapped ion system[77]. To perform a reliable Gaussian sampling, we develop the essential experimental technology with phonons, which includes the phase-coherent manipulation of displacement, squeezing, and rotation operations with multiple modes in a single realization. The required quantum optical operations are implemented through Raman laser beams. We discuss the difference between spin-independent and spin-dependent implementation of quantum optical operations. Finally, we show the molecular spectroscopic signal reconstruction scheme: collective projection measurements for two-phonon-mode. Our experimental demonstration would pave the way to large-scale molecular quantum simulations, which are classically intractable but would be easily verifiable by real molecular spectroscopy.

6.1　Boson sampling and vibronic spectroscopy

As starting from the original proposal by Aaronson and Arkhipov in 2011, boson sampling computer is believed to demonstrate the quantum supremacy with less demanding resources than the universal quantum computer[78]. In another word, this would be the first problem that classical computer intractable while the quantum computer can solve with a reasonable resource. Serious experimental endeavors have been reported to realize the small-scale version only in photonic systems[79–84].

The boson sampling problem is described as follows: a linear interferometer contains N modes with input and output ports, M indistinguishable bosons are injected from the input ports, The output ports probability distribution of bosons is the task to solve, the detailed description can be found on ref [85]. $|\psi_{out}\rangle = \hat{R} |\psi_{in}\rangle$, where $|\psi_{in}\rangle$ and $|\psi_{out}\rangle$ are the input state and output state, $\hat{R}$ stands for the transformation of the liner network (also called beamsplitter operator, or rotation operator). For classical computation, the output

distribution is hard to achieve due to the requirement of the matrix permanent of $\hat{R}$, which belongs to the complexity class $\#P$ problem.

Vibronic spectroscopy involves simultaneous changes in the vibrational and electronic) energy states of a molecule. The intensity of allowed vibronic transitions is governed by the Franck–Condon principle. Vibronic spectroscopy may provide information, such as bond-length, on electronic excited states of stable molecules[86]. The calculation of Franck-Condon factors takes the form $\left[\int \Psi_f^\star \cdot \Psi_i d\tau\right]^2$, where Ψ_i and Ψ_f denote the initial and final vibronic state with respect to the transition.

Figure 6.1 depicts a scheme for reconstructing the spectroscopy at zero Kelvin from the output measurements of the trapped-ion simulator, the transition intensities from the ground state to the excited states are aligned according to the transition frequencies.
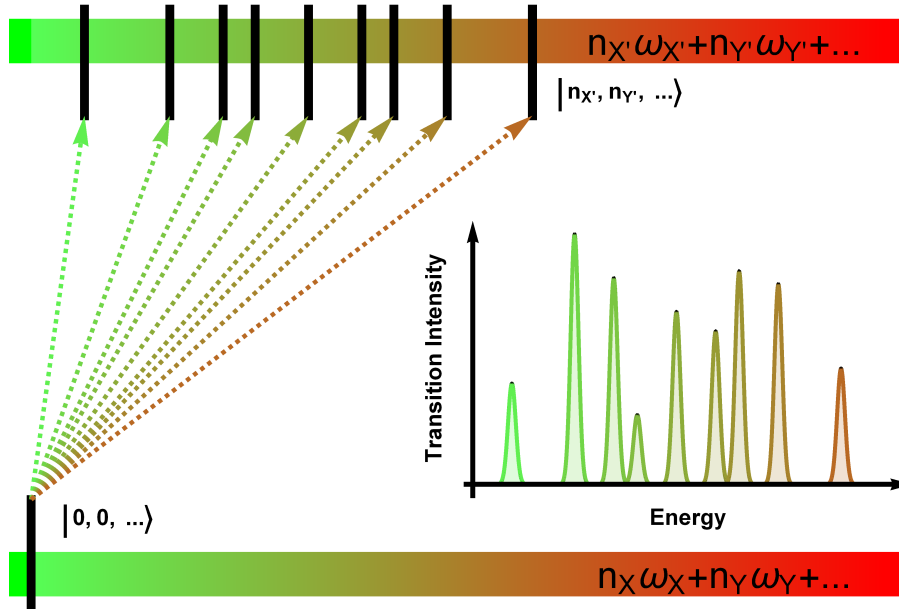
图 6.1　Generic diagram for molecular transition process at $T = 0$ K. The lower bar indicates the initial state and the upper bar shows the final states after the process. The vibronic spectroscopy is constructed by measuring the transition probabilities from $|n_X = 0, n_y = 0, ...\rangle$ to $|n_{X'}, n_{Y'}, ...\rangle$.

For the molecular vibronic spectroscopy, it carries the vibrational transitions between nuclear manifolds belonging to two electronic states of a molecule[75,87], we take the molecular SO_2 as our example, shown in Figure 6.2. Upon the electronic transition, a molecule undergoes structural deformation, vibrational frequency changes and rotation of normal modes; within a harmonic approximation to the electronic potential energy surfaces, these are equivalent to the displacement ($\hat{D}$), squeezing ($\hat{S}$) and rotation ($\hat{R}$)
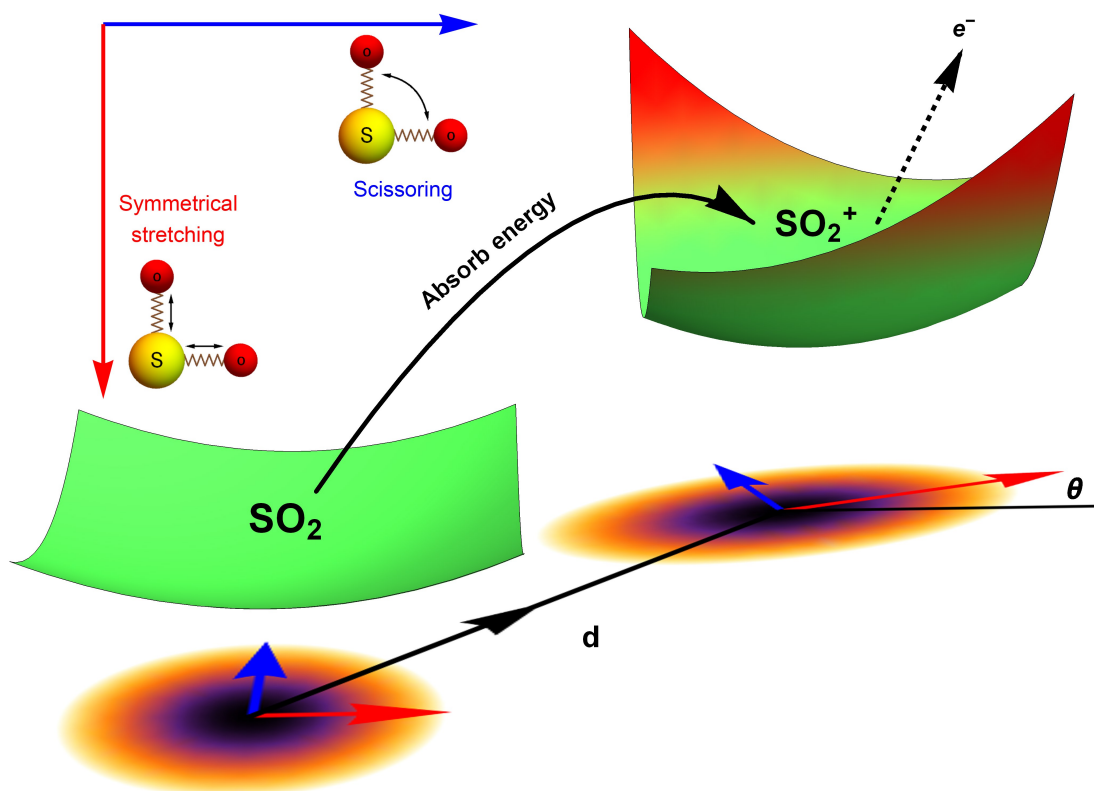
图 6.2 Pictorial description of the photoelectron spectroscopy of SO_2. The photoelectron process of $SO_2 \rightarrow SO_2^+$. The molecule is initially at the vibrational ground state of the symmetrical stretching and scissoring modes. After absorbing a photon, an electron is removed from the molecule, and the molecule finds a new equilibrium structure for SO_2^+, where the new potential energy surface is displaced, squeezed, and rotated from the original one. The transition of SO_2^- $\rightarrow SO_2$ can be described similarly.

operations in quantum optics, respectively. The (mass-weighted) normal coordinates of initial ($\mathbf{Q}$) and final ($\mathbf{Q}'$) states are related linearly as $\mathbf{Q}' = \mathbf{U}\mathbf{Q} + \mathbf{d}$, where $\mathbf{U}$ is called the Duschinsky rotation matrix and $\mathbf{d}$ is a displacement vector of the multidimensional harmonic oscillators in the mass-weighted coordinate, the corresponding dimensionless displacement vector $\boldsymbol{\alpha}$ for the quantum optical operation is used in this chapter[87]. As a result, the molecule performs a multi-mode Bogoliubov transformation[88] between the (vibrational) boson operators of the initial and final electronic states[75,76]. The probability distribution regarding a given molecular vibronic transition frequency (ω_v) at zero Kelvin, that is, spectroscopy (Franck-Condon profile), is read as a Fermi's golden rule for a unitary

Gaussian operator $\hat{U}_{\text{Dok}}$[75,87,89],

$$F(\omega_{\text{v}}) = \sum_{\mathbf{m}=\mathbf{0}}^{\infty} |\langle \mathbf{m}|\hat{U}_{\text{Dok}}|\mathbf{0}\rangle|^2 \delta(\Delta_{\omega_{\text{v}}}) \tag{6-1}$$

where $\Delta_{\omega_{\text{v}}} = \omega_{0-0} + \omega_{\text{v}} - (\sum_{k=1}^{M} m_k \omega'_k)$, with the k-th vibrational frequency (ω'_k) of a molecule in the final electronic state (ω_k belongs to the initial electronic state). The constant off-set frequency ω_{0-0}, which includes the electronic transition and the zero-point vibrational transition, is set to be zero here without losing the generality. $|\mathbf{0}\rangle = |0_1, \ldots, 0_M\rangle$ and $|\mathbf{m}\rangle = |m_1, \ldots, m_M\rangle$ are the initial and final M-dimensional Fock states, respectively.

Doktorov et al.[89] decomposed $\hat{U}_{\text{Dok}}$ in terms of the elementary quantum optical operators as follows:

$$\hat{U}_{\text{Dok}} = \hat{D}_N(\boldsymbol{\alpha})\hat{S}_N^{\dagger}(\boldsymbol{\zeta}')\hat{R}_N(\mathbf{U})\hat{S}_N(\boldsymbol{\zeta}) \tag{6-2}$$

where $\hat{D}_N, \hat{S}_N$ and $\hat{R}_N$ are the N-mode operators of displacement, squeezing and rotation[90] (see also section 6.2.1); $\boldsymbol{\alpha}(= \boldsymbol{\zeta}'\mathbf{d}/\sqrt{2\hbar})$ is a (dimensionless) molecular displacement vector, $\boldsymbol{\zeta} = \text{diag}(\ln\sqrt{\omega_1}, \ldots, \ln\sqrt{\omega_N})$ and $\boldsymbol{\zeta}' = \text{diag}(\ln\sqrt{\omega'_1}, \ldots, \ln\sqrt{\omega'_N})$ are diagnoal matrices of the squeezing parameters, and $\boldsymbol{U}$ is a unitary rotation matrix. The actions of the quantum optical operators are defined in Ref. [90]. Therefore, the sequential operations of the quantum optical operators in Eq. (6-2) to the vacuum state and the measurement in Fock basis, as in Eq. (6-1), can simulate the Franck-Condon profile[75].

6.2　Trapped ion emulation of molecular vibronic spectroscopy

The process of molecular vibronic spectroscopy can be understood as a modified boson sampling with Gaussian input states such as thermal and squeezed vacuum states. The Gaussian boson sampling, which is classified as the classically hard problem in the computational complexity perspective[73,74], requires more quantum optical operations on top of beam splitting and phase shifting operations for the standard boson sampling. The boson sampling, however, is challenging in an optical system[79–82] because of the difficulties in preparing the initial states: single Fock states for the original boson sampling and squeezed coherent states for the molecular simulation. Non-optical boson sampling devices, such as trapped-ion[91,92] and superconducting circuit [93], have been suggested

theoretically for the scalable boson sampling machine to overcome the difficulties of the optical implementation in preparing the single photon states. Moreover, these non-optical devices can handle the squeezed states with relative ease. Here, we present the first quantum simulation of molecular vibronic spectroscopy with a particular example of photoelectron spectroscopy of sulfur dioxide (SO_2)[94,95].
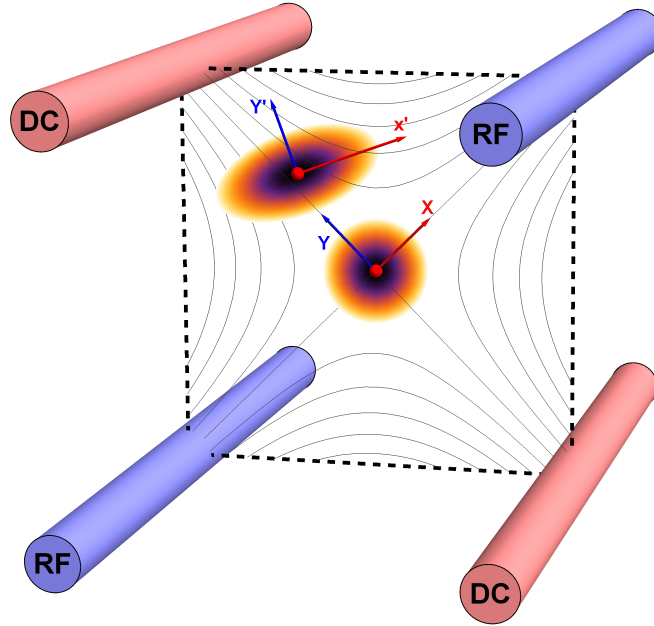

图 6.3　The trapped-ion emulator for molecular vibronic spectroscopy. The trapped-ion emulator is performing the Gaussian transformation for the molecular vibronic spectroscopy. The two vibrational modes of SO_2 are mapped to two radial modes (X and Y) of a single trapped-ion. The photoelectron process is simulated by applying series of quantum optical operations, which are implemented by Raman laser beams (see section 6.3). Generally, the photoelectron process of more complicated molecules with N vibrational modes can be mapped to the collective motional modes of N ions with the similar operations by Raman laser beams.

Figure 6.3 schematically illustrates quantum optical operations of Eq. (6-2) in the trapped-ion device for the molecular vibronic spectroscopy of SO_2. Our trapped-ion simulation is performed using a single $^{171}Yb^+$ ion confined in the 3-dimensional harmonic potential generated by the four-rod trap. The two vibrational modes of the molecule are mapped to the two radial phonon modes (X and Y) of an ion, with the trap frequencies $\omega_X = (2\pi)2.6$ MHz and $\omega_Y = (2\pi)2.2$ MHz.

After the mapping of the Hilbert space between the real molecule and simulator is established, the molecular spectroscopy is simulated through the following procedure: (i) the ion is first initialized to the motional ground state, (ii) the quantum optical operations

in Eq. (6-2) are then sequentially applied, and (iii) finally, the vibronic spectroscopy is constructed using the collective projection measurements (see section 6.4) on the transformed state.

Accordingly, for the first step of the molecular spectroscopy simulation, we prepare the ion in the ground state $|n_X = 0, n_Y = 0\rangle$ by the Doppler cooling and the resolved sideband cooling methods[96,97]. Next, we perform the required displacement, squeezing and rotation operations by converting the molecular parameters to the corresponding device parameters. The molecular parameters α, ζ', U and ζ can be obtained via conventional quantum chemical calculations with available program packages (e.g., Ref. [98]). See section 6.2.2, for the details of the parameter conversion for SO_2.

6.2.1　General definition of Quantum optical operators

We define, herein, the quantum optical operators we have used in this chapter. $\boldsymbol{a}$ and $\boldsymbol{a}^\dagger$ are N-dimensional column vectors for the bosonic annihilation and creation operators, respectively. That is,

$$\boldsymbol{a} \equiv (a_1, a_2, ..., a_N)^{\mathrm{T}} , \ \boldsymbol{a}^\dagger \equiv (a_1^\dagger, a_2^\dagger, ..., a_N^\dagger)^{\mathrm{T}} \tag{6-3}$$

where $[a_i, a_j^\dagger] = \delta_{ij}$.

The N-mode displacement operator is defined as below with the displacement vector $\boldsymbol{\alpha} = (\alpha_1, \alpha_2, ..., \alpha_N)$,

$$\hat{D}_N(\boldsymbol{\alpha}) = \exp\{\alpha \boldsymbol{a}^\dagger - \alpha^* \boldsymbol{a}\} \tag{6-4}$$

The N-mode squeezing operator is defined as below with the squeezing parameter matrix $\boldsymbol{\zeta} = \mathrm{diag}(\zeta_1, \zeta_2, ..., \zeta_N)$.

$$\hat{S}_N(\boldsymbol{\zeta}) = \exp\{\frac{\boldsymbol{a}^{\mathrm{T}} \boldsymbol{\zeta}^\dagger \boldsymbol{a}}{2} - \frac{(\boldsymbol{a}^\dagger)^{\mathrm{T}} \boldsymbol{\zeta} \boldsymbol{a}^\dagger}{2}\} \tag{6-5}$$

The N-mode rotation operator is defined as below with a unitary matrix $\boldsymbol{U}$,

$$\hat{R}_N(\boldsymbol{U}) = \exp\{(\boldsymbol{a}^\dagger)^{\mathrm{T}} \ln(\boldsymbol{U}) \boldsymbol{a}\} \tag{6-6}$$

6.2.2　Experimental parameters for quantum optical operations

We present in this section, the parameters used in the trapped-ion device for the quantum optical operations. The displacement operator with two modes is rewritten as follows,

$$\hat{D}_2(\boldsymbol{\alpha}) = \hat{D}(\alpha_X, \alpha_Y) =$$
$$\exp\{\alpha_X a_X^\dagger - \alpha_X^* a_X\}\exp\{\alpha_Y a_Y^\dagger - \alpha_Y^* a_Y\}. \tag{6-7}$$

As seen in Eq. (6-7), the displacement operations of the X and Y modes can be implemented independently.

The squeezing operator with the two mode parameter $\boldsymbol{\zeta} = \mathrm{diag}(\ln\sqrt{\omega_1}, \ln\sqrt{\omega_2}) = \mathrm{diag}(\zeta_X, \zeta_Y)$ can be rewritten as follows,

$$\hat{S}_2(\boldsymbol{\zeta}) = \hat{S}(\mathrm{diag}(\zeta_X, \zeta_Y)) =$$
$$\exp\{\frac{\zeta_X}{2}(a_X a_X - a_X^\dagger a_X^\dagger)\}\exp\{\frac{\zeta_Y}{2}(a_Y a_Y - a_Y^\dagger a_Y^\dagger)\}. \tag{6-8}$$

In the trapped-ion experiment, the squeezing operations are limited to the range of $\zeta_X(\zeta_Y) \le 4$ in Eq. (6-8). Since $\hat{U}_{\mathrm{Dok}}$ involves the squeezing and inverse squeezing operations, we can freely re-scale the squeezing parameters with a single arbitrary constant. In our experiment, we rescale the squeezing parameters by a factor of 1/25, $\mathrm{diag}(\zeta_X, \zeta_Y) = \mathrm{diag}(\ln(\sqrt{\omega_1}/25), \ln(\sqrt{\omega_2}/25))$ for the first squeezing operation and $\mathrm{diag}(\zeta_X', \zeta_Y') = \mathrm{diag}(\ln(\sqrt{\omega_1'}/25), \ln(\sqrt{\omega_2'}/25))$ for the anti-squeezing in the Eq (6-2). As discussed in Ref [75], the Doktorov operation $\hat{U}_{\mathrm{Dok}}$ in Eq (6-2) can be expressed in terms of the ladder operators as

$$\boldsymbol{a'}^\dagger = \frac{1}{2}(\boldsymbol{J} - (\boldsymbol{J}^t)^{-1})\boldsymbol{a} + \frac{1}{2}(\boldsymbol{J} + (\boldsymbol{J}^t)^{-1})\boldsymbol{a}^\dagger + \frac{1}{\sqrt{2}}\boldsymbol{\alpha} \tag{6-9}$$

where $\boldsymbol{J} = \boldsymbol{\zeta}'\boldsymbol{U}\boldsymbol{\zeta}^{-1}$. Since $\boldsymbol{J}$ is invariant for the parameter sets $(\boldsymbol{\zeta}', \boldsymbol{\zeta})$ and $(\boldsymbol{\zeta}'/\mathbf{25}, \boldsymbol{\zeta}/\mathbf{25})$ as an example, the resulting $\hat{U}_{\mathrm{Dok}}$ is maintained.

The two mode rotation operation can be written simply with a rotation angle θ,

$$\hat{R}_2(\boldsymbol{U}) = \hat{R}(\theta) = e^{\theta(\hat{a}_X^\dagger \hat{a}_Y - \hat{a}_X \hat{a}_Y^\dagger)} \tag{6-10}$$

where $U = \begin{pmatrix} \cos\theta & \sin\theta \\ -\sin\theta & \cos\theta \end{pmatrix}$ becomes the unitary rotation matrix. The rotation angle θ is controlled by Raman laser beams in the trapped-ion simulation.

表 6.1　Parameters for the trapped-ion simulation of SO_2

	$SO_2 \rightarrow SO_2^+$	$SO_2^- \rightarrow SO_2$
α_X, α_Y	$(-0.026, 1.716)$	$(1.360, -0.264)$
ω_1', ω_2'	$(1112.7, 415)$	$(1178.4, 518.9)$
ζ_X', ζ_Y'	$(0.288, -0.204)$	$(0.317, -0.093)$
U	$\begin{pmatrix} 0.982 & 0.188 \\ -0.188 & 0.982 \end{pmatrix}$	$\begin{pmatrix} 0.998 & 0.065 \\ -0.065 & 0.998 \end{pmatrix}$
θ	0.1892	0.065
ω_1, ω_2	$(1178.4, 518.9)$	$(989.5, 451.4)$
ζ_X, ζ_Y	$(0.317, -0.093)$	$(0.229, -0.162)$

6.3　Quantum optical operations implementation in trapped ion system

We implement the quantum optical operations ($\hat{D}$, $\hat{S}$ and $\hat{R}$) via controlling Raman laser beams. Figure 3.8 shows the energy diagram of a trapped $^{171}Yb^+$. The two levels in hyperfine structure of $^2S_{1/2}$ manifold are usually used to realize a qubit, which are denoted as $|\downarrow\rangle \equiv |F = 0, m_F = 0\rangle$ and $|\uparrow\rangle \equiv |F = 1, m_F = 0\rangle$. The red color (mode X) and blue color (mode Y) harmonic oscillators stand for the motional degrees of freedom. The Raman process is implemented via the virtual energy level, which is 10.8 THz detuned from $P_{1/2}$ level, $|e\rangle$.

Here, From the theory aspect of view, we show two ways of implementing these Quantum optical operations, spin-dependent implementation and spin-independent implementation. Both schemes rely on the experiment configuration of counter-propagating Raman laser beam. For each quantum optical operator, the spin-independent operator requires one frequency in Raman 1 + one frequency in Raman 2, while the spin-dependent operator requires one frequency in Raman 1 + two frequencies in Raman 2. The details are presented in following sections.

6.3.1　Spin-dependent operations

In this section, the introduced operations are internal-state dependent, which requires one frequency in Raman 1, ω_{R1}, and two frequencies and phases in Raman 2, $\omega_{\text{R2,1}}$ and $\omega_{\text{R2,2}}$, where Raman 1 and Raman 2 are counter-propagating towards the ion. Here, we show how the quantum optical operations are implemented with these laser beams. We start from the light-matter interaction Hamiltonian as shown in the following equation,

$$H = \frac{\hbar\omega_{\text{hf}}}{2}\sigma_{\text{Z}} + \hbar\omega_{\text{X}}(a_{\text{X}}^{\dagger}a_{\text{X}} + \frac{1}{2}) + \hbar\omega_{\text{Y}}(a_{\text{Y}}^{\dagger}a_{\text{Y}} + \frac{1}{2})$$
$$+ \sum_{j=1,2}\frac{\hbar g}{2}(\sigma_{+} + \sigma_{-})(e^{i(\vec{k}\cdot\vec{r}-\omega_{L,j}t+\phi_j)} + e^{-i(\vec{k}\cdot\vec{r}-\omega_{L,j}t+\phi_j)}), \tag{6-11}$$

where g is the Rabi frequency, $\sigma_{+} = |{\uparrow}\rangle\langle{\downarrow}|$ and $\sigma_{-} = |{\downarrow}\rangle\langle{\uparrow}|$, effective laser frequencies $\omega_{L,j} = \omega_{R1} - \omega_{R2,j}$, phases ϕ_j and $\vec{k}\cdot\vec{r} = k_{\text{X}}x + k_{\text{Y}}y$.

The interaction Hamiltonian with respect to $H_0 = \frac{\hbar\omega_{\text{hf}}}{2}\sigma_{\text{Z}} + \hbar\omega_{\text{X}}(a_{\text{X}}^{\dagger}a_{\text{X}} + \frac{1}{2}) + \hbar\omega_{\text{Y}}(a_{\text{Y}}^{\dagger}a_{\text{Y}} + \frac{1}{2})$ with rotating wave approximation and the Lamb-Dicke approximation $\eta_{\text{X(Y)}}^2(2\langle n\rangle + 1) \ll 1$, where Lamb-Dicke parameters $\eta_{\text{X}} = \sqrt{2}k_{\text{X}}\sqrt{\hbar/2M_{\text{Yb}}\omega_{\text{X}}} = 0.080$ and $\eta_{\text{Y}} = \sqrt{2}k_{\text{Y}}\sqrt{\hbar/2M_{\text{Yb}}\omega_{\text{Y}}} = 0.087$, can be written as

$$H_I = \sum_{j=1,2}\frac{\hbar g}{2}\sigma_{+}\{1 + i\eta_{\text{X}}(a_{\text{X}}e^{-i\omega_{\text{X}}t} + a_{\text{X}}^{\dagger}e^{i\omega_{\text{X}}t})$$
$$+ i\eta_{\text{Y}}(a_{\text{Y}}e^{-i\omega_{\text{Y}}t} + a_{\text{Y}}^{\dagger}e^{i\omega_{\text{Y}}t})$$
$$- \eta_{\text{X}}\eta_{\text{Y}}(a_{\text{X}}e^{-i\omega_{\text{X}}t} + a_{\text{X}}^{\dagger}e^{i\omega_{\text{X}}t})(a_{\text{Y}}e^{-i\omega_{\text{Y}}t} + a_{\text{Y}}^{\dagger}e^{i\omega_{\text{Y}}t})\}$$
$$e^{-i\delta_j t}e^{i\phi_j} + \text{h.c.}, \tag{6-12}$$

where $\delta_j = \omega_{L,j} - \omega_{\text{hf}}$.

When we consider the resonant terms, we have the following effective Hamiltonian. By setting $\delta_1 = \omega_{\text{X}}$, $\delta_2 = -\omega_{\text{X}}$, as shown in Figure 6.4 (a), the displacement operation $\hat{D}$ of a single mode (here, mode X as an example) is written as

$$\hat{D}(\alpha_{\text{X}}, 0) = \exp\left\{-i\alpha_{\text{X}}(\sigma_{+}e^{i\phi_A} - \sigma_{-}e^{-i\phi_A})(a_{\text{X}}^{\dagger}e^{-i\phi_B} + a_{\text{X}}e^{i\phi_B})\right\},$$

where $\alpha_{\text{X}} = tg_D = t\frac{\eta_{\text{X}}\hbar g}{2}$, $\phi_A = \phi_1 + \phi_2$ and $\phi_B = \phi_2 - \phi_1$. When $\phi_1 = \phi_2 = \pi/2$, $\hat{D}(\alpha_{\text{X}}, 0)$ becomes σ_x-dependent displacement operation. We change it to σ_z-dependent

displacement operation with additional $\pi/2$ carrier rotation pulses (along σ_y and σ_{-y} axis) before and after σ_x−dependent displacement.

Similarly, by setting $\delta_1 = \omega_X - \delta_S$, $\delta_2 = -\omega_X - \delta_S$, as shown in Figure 6.4 (b), the squeezing operation $\hat{S}$ of a single mode (here, mode X as an example) is written as

$$\hat{S}(\zeta_X, 0) = \exp\left\{-i\zeta_X(a_X^\dagger a_X^\dagger e^{i\phi_B} + a_X a_X e^{-i\phi_B})\sigma_z\right\}, \tag{6-13}$$

where $\zeta_X = tg_S = t\dfrac{\hbar\eta_X^2 g^2}{8}\left(\dfrac{1}{\delta_1} - \dfrac{2}{\delta_1 - \omega_X} + \dfrac{1}{\delta_1 - 2\omega_X}\right)$ and $\phi_B = \phi_2 - \phi_1$. In our experiment, the δ_S is set as five times of anti-Jaynes-Cummings coupling Rabi frequency ($\eta_X g$).

For rotation operation $\hat{R}$, we set $\delta_1 = -\omega_X - \delta_R$, $\delta_2 = -\omega_Y - \delta_R$, which leads the configuration shown in Figure 6.4 (c). In our experiment, the δ_R is also set as five times of anti-Jaynes-Cummings coupling Rabi frequency ($\eta_X g$).

$$\hat{R}(\theta) = \exp\left\{-i\theta(a_X^\dagger a_Y e^{-i\phi_B} + a_X a_Y^\dagger e^{i\phi_B})\sigma_z\right\}. \tag{6-14}$$

where $\theta = tg_R = t\dfrac{\hbar\eta_X\eta_Y g^2}{4}\left(\dfrac{1}{-\delta_1} + \dfrac{1}{-\delta_1 + \omega_X - \omega_Y} + \dfrac{1}{\delta_1 - \omega_X} + \dfrac{1}{\delta_1 + \omega_Y}\right)$ and $\phi_B = \phi_2 - \phi_1$.
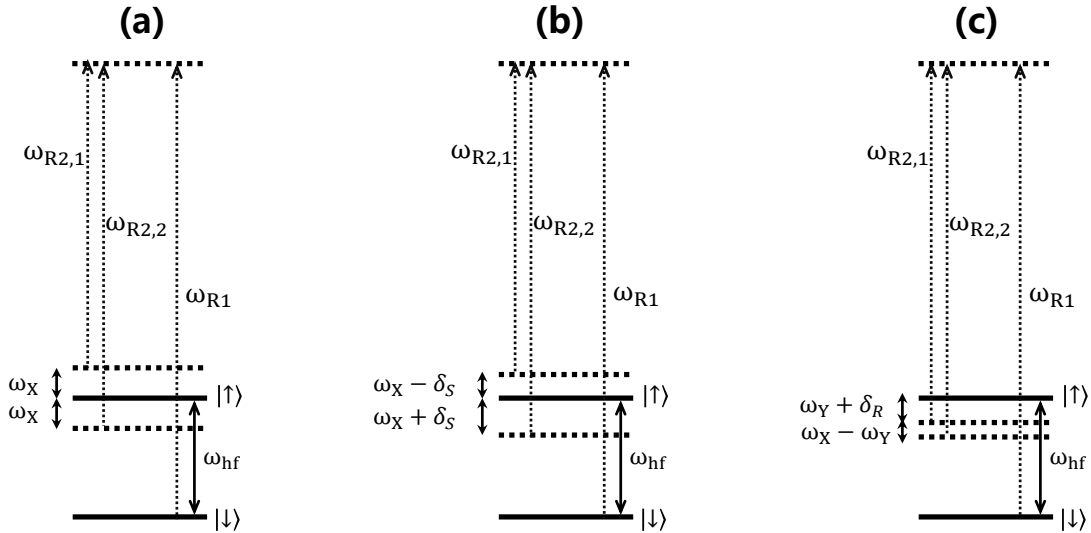
图 6.4　Trapped-ion implementation of the spin-dependent quantum optical operations. The Hilbert space is composed of two phonon modes of X and Y and the internal electronic state $|\uparrow\rangle$ and $|\downarrow\rangle$. The quantum operations are implemented via control the frequency and phase of $\omega_{R2,1}$ and $\omega_{R2,2}$. (a) Coherent displacement operation $\hat{D}$ and (b) squeezing operation $\hat{S}$ on X mode as an example. (c) Rotation operation $\hat{R}$ between X and Y modes.

When we only consider the Hilbert space with the state $|\downarrow\rangle$, all the above σ_z−dependent forces can be simplified to the quantum optical operations shown in section 6.2.2.

6.3.2 Spin-independent operations

With a similar way of deriving process, here, we consider one frequency ω_1 in Raman 1 laser and ω_2 in Raman 2 laser. The displacement operation $\hat{D}$ of single mode (here, mode X as an example) by setting two Raman laser frequencies $\omega_1 = \omega_e - \Delta$, $\omega_2 = \omega_e - \Delta + \omega_X$, Δ is the energy gap from the virtual energy level to $|e\rangle$, which leads the configuration shown in Figure 6.5 (a),

$$\hat{D}(\delta_X, 0) = \exp\left\{-it\frac{\hbar g^2 \eta_X}{2\Delta}(a_X^\dagger e^{i\Delta\phi} + a_X e^{-i\Delta\phi})\right\},\tag{6-15}$$

where $\Delta\phi = \phi_2 - \phi_1$ is the relative phase between Raman 1 laser beam and Raman 2 laser beams.

Similarly, we can perform the squeezing operation $\hat{S}$ of single motional mode (here, mode X as an example) by setting two Raman laser frequencies as $\omega_1 = \omega_e - \Delta$, $\omega_2 = \omega_e - \Delta + 2\omega_X$, which leads the configuration shown in Figure 6.5(b),

$$\hat{S}(\zeta_X, 0) = \exp\left\{-it\frac{\hbar g^2 \eta_X^2}{2\Delta}(a_X^\dagger a_X^\dagger e^{i\Delta\phi} + a_X a_X e^{-i\Delta\phi})\right\},\tag{6-16}$$

When the two Raman laser beam frequencies as seted as $\omega_1 = \omega_e - \Delta$, $\omega_2 = \omega_e - \Delta + (\omega_X - \omega_Y)$, which is represented by the configuration shown in Figure 6.5 (c).

$$\hat{R}(\theta) = \exp\left\{-it\frac{\hbar g^2 \eta_X \eta_Y}{2\Delta}(a_X^\dagger a_Y e^{i\Delta\phi} + a_X a_Y^\dagger e^{-i\Delta\phi})\right\}.\tag{6-17}$$

6.3.3 Experimental performance of spin-dependent operations

In real experimental situation, since the laser carries the phase information while propagating, the phase relation between Raman 1 laser and Raman 2 laser can be easily destroyed due to the air disturbance. So the spin-independent implementation is not suitable for this kind of sequentially applied operations experiment.

We use the spin-dependent operators in real experiment, The optical phase instability between Raman 1 and Raman 2 caused by the beam fluctuation does not influence the

(a)   **(b)**   **(c)**
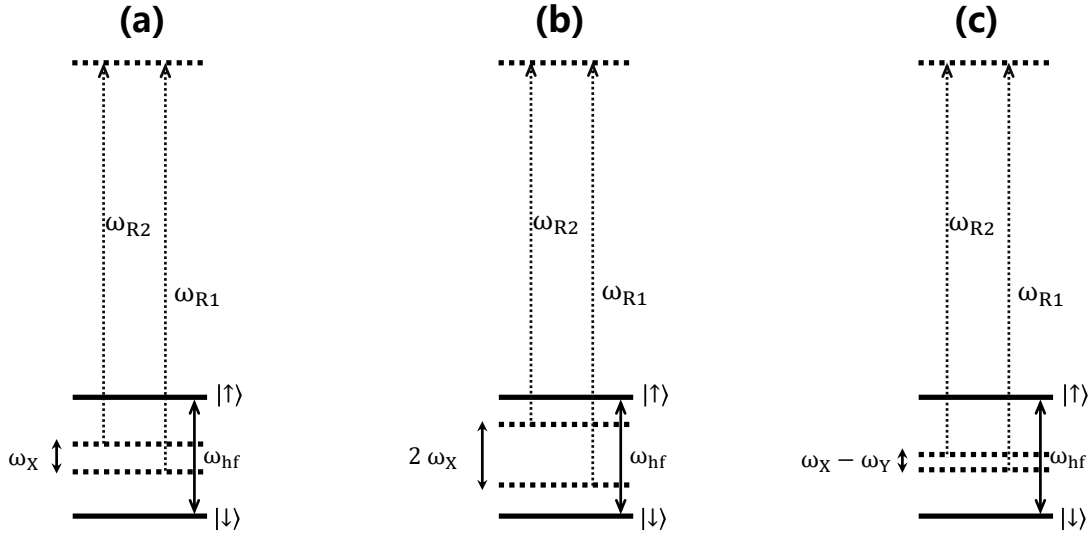
图 6.5   Trapped-ion implementation of the spin-independent quantum optical operations. The quantum operations are implemented via control the frequency and phase of ω_1 and ω_2. (a) Coherent displacement operation $\hat{D}$ and (b) squeezing operation $\hat{S}$ on X mode as an example. (c) Rotation operation $\hat{R}$ between X and Y modes.

coherence of quantum operations, since all the phases ϕ_B of all these quantum operations are controlled by RF sources on Raman 2. so the phase coherence among them are well preserved, as discussed in section 6.3.1.

The quantum optical operations (displacement $\hat{D}$, squeezing $\hat{S}$ and rotation $\hat{R}$), which preserves phase coherence among them, are implemented by the σ^+-polarized Raman laser beams from a Picosecond pulsed laser with a wavelength of 375 nm (see section 6.3.1). In the trapped-ion experiment, the quantum optical operations with the desired parameters can be performed by controlling the applied laser frequency, duration, intensity and phase. With different Raman laser configurations, we can realize displacement, squeezing and rotation operations, respectively[99,100]. Figure 6.6 (a) shows the performance of the experimental displacement $\hat{D}_2(\alpha) = \hat{D}(\alpha_X, 0) = e^{\alpha_X \hat{a}_X^\dagger - \alpha_X^* \hat{a}_X}$ and squeezing $\hat{S}_2(\zeta) = \hat{S}(\text{diag}(\zeta_X, 0)) = e^{\frac{1}{2}(\zeta_X^* \hat{a}_X \hat{a}_X - \zeta_X \hat{a}_X^\dagger \hat{a}_X^\dagger)}$ operations, where a_X and $a_X^\dagger$ are the annihilation and creation operators of bosonic mode X, respectively. The amount of the displacement α and the squeezing parameter ζ are controlled by the duration of the corresponding Raman beams with the rates of 0.042 μs^{-1} and 0.004 μs^{-1}, respectively. We examine the trapped-ion implementation of the rotation operation $\hat{R}_2(U) = \hat{R}(\theta) = e^{\theta(\hat{a}_X^\dagger \hat{a}_Y - \hat{a}_X \hat{a}_Y^\dagger)}$ between modes X and Y with two sets of initial states, as indicated in Figure 6.6 (b). The rotation angle θ is also controlled by the duration of the operation with a rate of 0.005

rad μs^{-1}. The oscillations in Figure 6.6 (b) of the initial state $|n_X = 1, n_Y = 0\rangle$ (orange and green) are twice slower than those from state $|1, 1\rangle$ (blue, black and red), as expected. We note that at $t = 157\mu s$, the near zero probability of $\langle 1, 1| \hat{R} |1, 1\rangle$ originates from the Hong-Ou-Mandel interference[100].

We confirm the phase coherence between $\hat{D}$ and $\hat{S}$ by experimentally reconstructing the Wigner function of a coherent displacement state and a squeezed vacuum state. The comparisons with theoretical calculation are shown in Figure 6.7. We reconstruct the Wigner function by using the iterative maximum-likelihood algorithm on the phonon number distribution for eight different angles in the phase space[99,101]. The phonon number distribution is constructed in three steps: (i) prepare the initial coherent state or squeezed vacuum state, (ii) coherent push the initial state with eight different angles, (iii) apply the standard Jaynes Cummings coupling and resolve the distribution through the fitting of the observed oscillations.

6.4　Scheme for the construction of vibronic spectroscopy

Figure 6.8 (b) illustrates the transition between the two-dimensional Fock spaces resulting from the two-dimensional harmonic oscillators. We perform the collective quantum-projection measurement of the final state $|n_X, n_Y\rangle$ advanced from the measurement scheme of Ref. [101,102]: first, we transfer the population of a target state $|n_X, n_Y\rangle$ to the $|0, 0\rangle$ state by a sequence of π-pulse transitions. Then, we measure the state population by applying three sequential fluorescence-detections combined with the uniform red sideband technique (see section 6.4.1). Our quantum projection measurement is limited by the imperfection of the state transfer and the fluorescence-detection efficiency. We plot the fidelity of the collective projection measurement of $|n_X, n_Y\rangle$ state in Figure 6.8 (b). Based on the fidelity analysis, We perform measurement-error corrections for the experimental raw data (see section 6.4.2 for the detailed information).

6.4.1　Method for collective projection measurements

We explain in this section the pulse sequence for the detection of population in an arbitrary phonon state $|\Sigma, n_X, n_Y\rangle$, where we indicate the internal qubit state Σ ($\downarrow$ or $\uparrow$) of the phonon state ($|n_X, n_Y\rangle$).

The first step is to transfer the population in the target state $|\downarrow, n_X, n_Y\rangle$ to $|\downarrow, 0, 0\rangle$: it is performed by applying a sequence of π-pulse transitions, as shown in Figure 6.9 (a), i.e.,
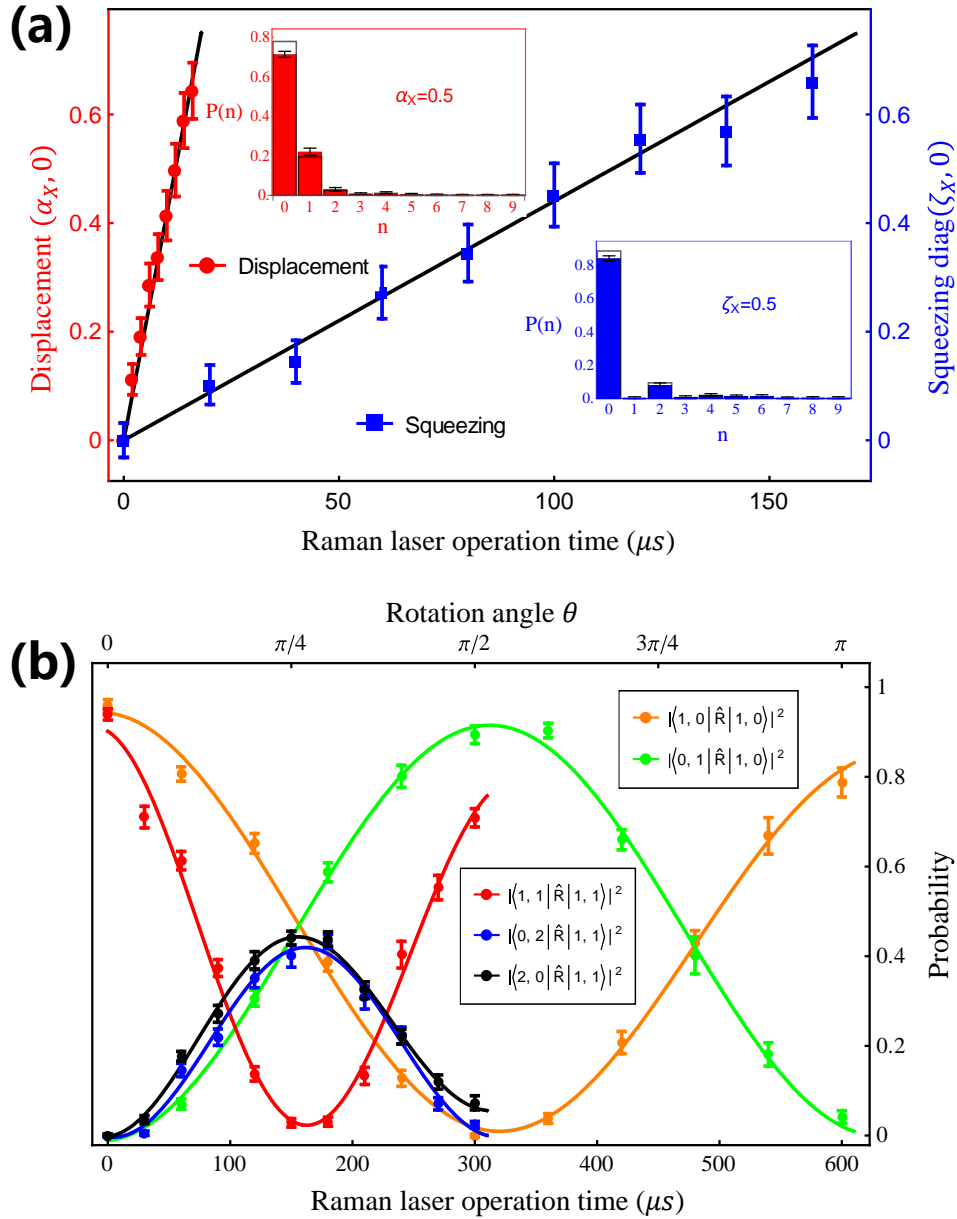
图 6.6 Trapped-ion demonstration of quantum optical operations; $\hat{D}$, $\hat{S}$, and $\hat{R}$. (a) Displacement $\alpha = (\alpha_X, 0)$ (red) and squeezing $\zeta = \mathrm{diag}(\zeta_X, 0)$ (blue) of mode X are controlled by the duration of Raman laser beams. The insets show the measured phonon distribution for $\alpha_X = 0.5$ and for the squeezing parameter of $\zeta_X = 0.5$. (b) The evolution of rotation operation between mode X and Y. The ion is first prepared in state $|n_X = 1, n_Y = 0\rangle$ (orange and green) and $|1, 1\rangle$ (blue, black and red), then we apply the rotation operation, finally measure the corresponding Fock state population via collective projection measurement method. Here all the operations are implemented by Raman laser beams. The dots represent the experimental data and the lines are obtained by fitting. The error bars stand for 95% confidence level.
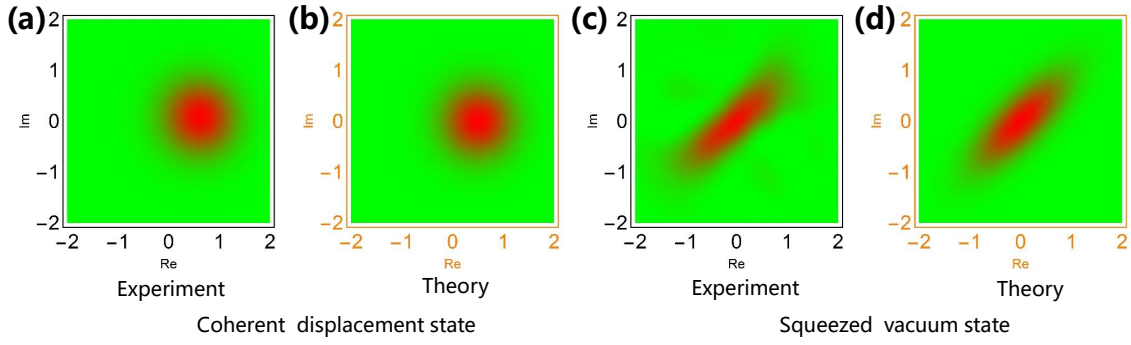
图 6.7　Coherent displacement and squeezed vacuum state Wigner functions. (a) and (b) represents for the coherent displacement state with $\alpha_X = 0.5$. (c) and (d) represents for the squeezed vacuum state with $\zeta_X = 0.5$.

with the following steps,

$$
\mathbf{a}: \; |\downarrow, n_X, n_Y\rangle \xrightarrow{\pi-\text{Carrier}} |\uparrow, n_X, n_Y\rangle \xrightarrow{\pi-\text{BlueX}} |\downarrow, n_X - 1, n_Y\rangle \ldots \longrightarrow \ldots |\downarrow, 0, n_Y\rangle
$$

$$
\xrightarrow{\pi-\text{Carrier}} |\uparrow, 0, n_Y\rangle \xrightarrow{\pi-\text{BlueY}} |\downarrow, 0, n_Y - 1\rangle \ldots \longrightarrow \ldots |\downarrow, 0, 0\rangle \quad (6\text{-}18)
$$

The second step is to obtain the population in $|\downarrow, 0, 0\rangle$ by using the sequence as shown in Figure 6.9 (b-f). The important technique used in this process is called uniform red sideband transition, which is a full population transfer independent of the initial motion state[101], it exchanges the state population between $|\downarrow, n_X + 1, n_Y\rangle$ and $|\uparrow, n_X, n_Y\rangle$ when it is uniform red sideband on mode X, or $|\downarrow, n_X, n_Y + 1\rangle$ and $|\uparrow, n_X, n_Y\rangle$ when it is uniform red sideband on mode Y. In the real experiment setting, the maximum phonon number are restricted to $n_{X(Y)} < 10$.

b: Apply the fluorescence detection and record the event M_1 of detecting photons or no photons.

c: Apply a uniform red sideband transition on mode X, which transfers all the states of $|\downarrow, n_X > 0, n_Y\rangle$ to $|\uparrow\rangle$ state.

d: Apply the fluorescence detection and record the event M_2 of detecting photons or no photons.

e: Apply a uniform red sideband transition on Y mode, which transfers all the states of $|\downarrow, n_X, n_Y > 0\rangle$ to $|\uparrow\rangle$ state.

f: Apply the fluorescence detection and record the event M_3 of detecting photons or no photons.

In the above multiple-detection stages, there are four situations for the recorded data
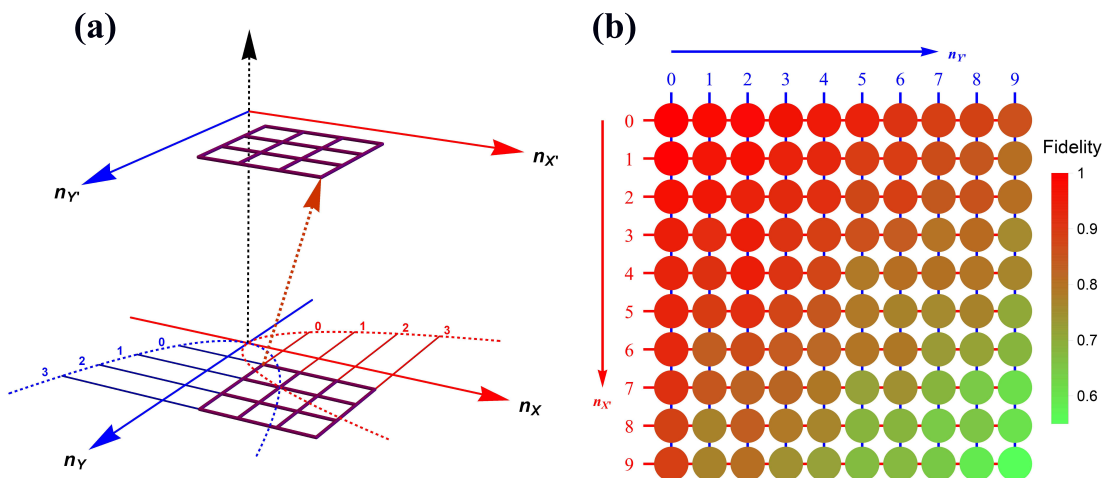
图 6.8　Construction scheme for the vibronic spectroscopy with two modes and measurement fidelity analysis. (a) The transition process of a molecule in the two-dimensional Fock space. The process begins with the lower plane and ends at the upper plane. The points in the grid represent the phonon number states. The transition probability is obtained by the collective projection measurements of two phonon modes (see section 6.4.1). (b) The fidelity analysis of the collective projection measurements. The fidelity of measuring the transition probability to the state $|n_{X'}, n_{Y'}\rangle$ is experimentally examined from $|0,0\rangle$ to $|9,9\rangle$. The fidelity is measured by applying the measurement sequence twice, as starting from $|0,0\rangle$ to $|n_{X'}, n_{Y'}\rangle$, and then bringing back to $|0,0\rangle$. The square root of the remained population represents the fidelity.
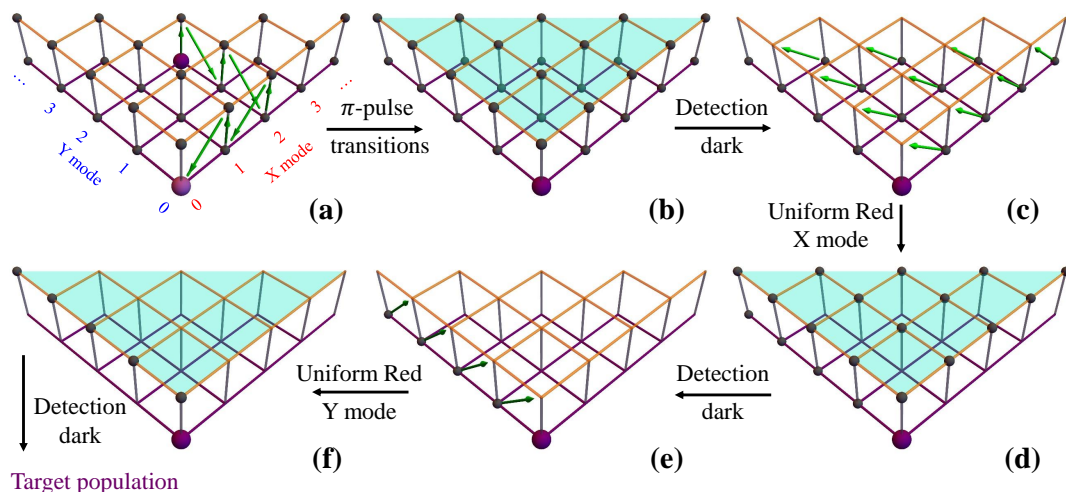
图 6.9　Detection method for the example of state $|\downarrow, n_X = 2, n_Y = 2\rangle$. The lower (purple grid) and the upper (orange grid) layers represent the internal states of $|\downarrow\rangle$ and $|\uparrow\rangle$. The internal states have no fluorescence and fluorescence, respectively, during the internal state detection.

95

$M_1 M_2 M_3$

$$\{B\forall\forall, DB\forall, DDB, DDD\} \rightarrow \{P_1, P_2, P_3, P_4\}. \tag{6-19}$$

Here, D means detecting no photons, B means detecting photons, $\forall$ stands for both situations. Typically, we repeat the experiments for 2000 times to get the probability for each case noted as P_1, P_2, P_3, P_4. The population of the target state is the probability of case P_4.

Within the above collective projection measurements, Figure 6.8 (b) shows the experimentally measured result for the fidelity of the detection sequence of an arbitrary state $|n_X, n_Y\rangle$, noted as $F_{D.M}$. The infidelity mainly comes from the imperfection of π-pulse and uniform red-transition on X and Y mode.

6.4.2　Measurement-error corrections for the experimental raw data
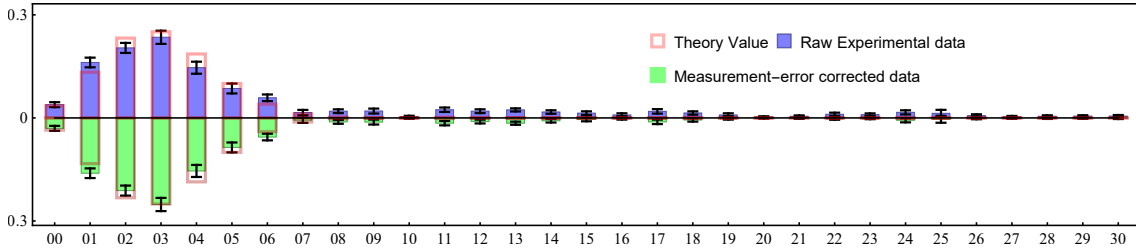
图 6.10　Comparison between the raw and the corrected experimental data for the spectroscopy of $SO_2 \rightarrow SO_2^+$. The horizontal axis is the Fock state $|n_{X'}, n_{Y'}\rangle$ and the vertical axis is the transition intensity to the state from the $|0, 0\rangle$ state.

We mainly consider two error sources to correct the experimental raw data: i) the inefficiency of fluorescence detection of internal states; ii) the infidelity of the collective projection measurement discussed in section 6.4.1.

Our fluorescence detection can distinguish the internal states $|\uparrow\rangle$ and $|\downarrow\rangle$ with the corresponding detection fidelities are $\eta_{\uparrow\rightarrow\uparrow}$ (97.2%) state and $\eta_{\downarrow\rightarrow\downarrow}$ (99.3%) for state, respectively. To correct this inefficiency, we use the value of P_4, which is obtained by $1-(P_1 + P_2 + P_3)$. The real population (P_R) of detecting photons scattered from the $|\uparrow\rangle$ state is not exactly same to the measured population (P_M). The relation between them is given as $P_M = P_R \eta_{\uparrow\rightarrow\uparrow} + (1 - P_R)(1 - \eta_{\downarrow\rightarrow\downarrow})$, thus

$$P_R \equiv \text{Corr}(P_M) = \frac{P_M - (1 - \eta_{\downarrow\rightarrow\downarrow})}{\eta_{\downarrow\rightarrow\downarrow} + \eta_{\uparrow\rightarrow\uparrow} - 1} \tag{6-20}$$

For the correction of the second part, as discussed in the section 6.4.1, we have to include the fidelity $F_{D,M}$.

In order to correct the raw experimental data, we consider these two imperfections. For the experiment raw data, our corrected data is written accordingly as,

$$P'_4 = \frac{1 - \text{Corr}(P_1 + P_2 + P_3)}{F_{D.M}} \tag{6-21}$$

Figure. 6.10 compares the raw experimental data and corrected data for the photoelectron spectroscopy of SO_2.

6.5   Experimental results

Finally, we simulate the photoelectron spectroscopies of SO_2 and SO_2^-, in which a single electron is removed from the molecule during the photon absorption process, with our trapped-ion quantum simulator. Owing to the symmetry of the molecules, we use only two vibrational modes of sulfur dioxide, which show mixing of the vibration modes with respect to the final vibrational coordinates[95], in our quantum simulation for the molecular spectroscopy; the remaining vibrational mode does not contribute to the overall spectral shape because SO_2 does not deform along the remaining (non-totally-symmetric) vibrational mode during the vibronic transition.

Figure 6.11 presents the photoelectron spectra, $SO_2 \rightarrow SO_2^+$ and $SO_2^- \rightarrow SO_2$ obtained from our trapped-ion quantum simulation; theses are compared with the theoretical classical calculations. Figure 6.11 shows good agreement between the theory calculations and the trapped-ion simulations of the two photoelectron processes of sulfur dioxide, the required molecular parameters are described in the figure caption. In Figure 6.11 (a), the photoelectron spectroscopy of SO_2 is dominated by ω'_2 transitions due to the significant large displacement along the second mode: $\alpha = (-0.026, 1.716)$. The photoelectron spectroscopy of SO_2^- in Figure 6.11 (b) shows tiny combination bands of the first and second modes regardless of the dominant contribution of the first mode ($\alpha = (1.360, -0.264)$). We note that the observation of the tiny band combinations indicates the reliable performance of the trapped-ion simulation.
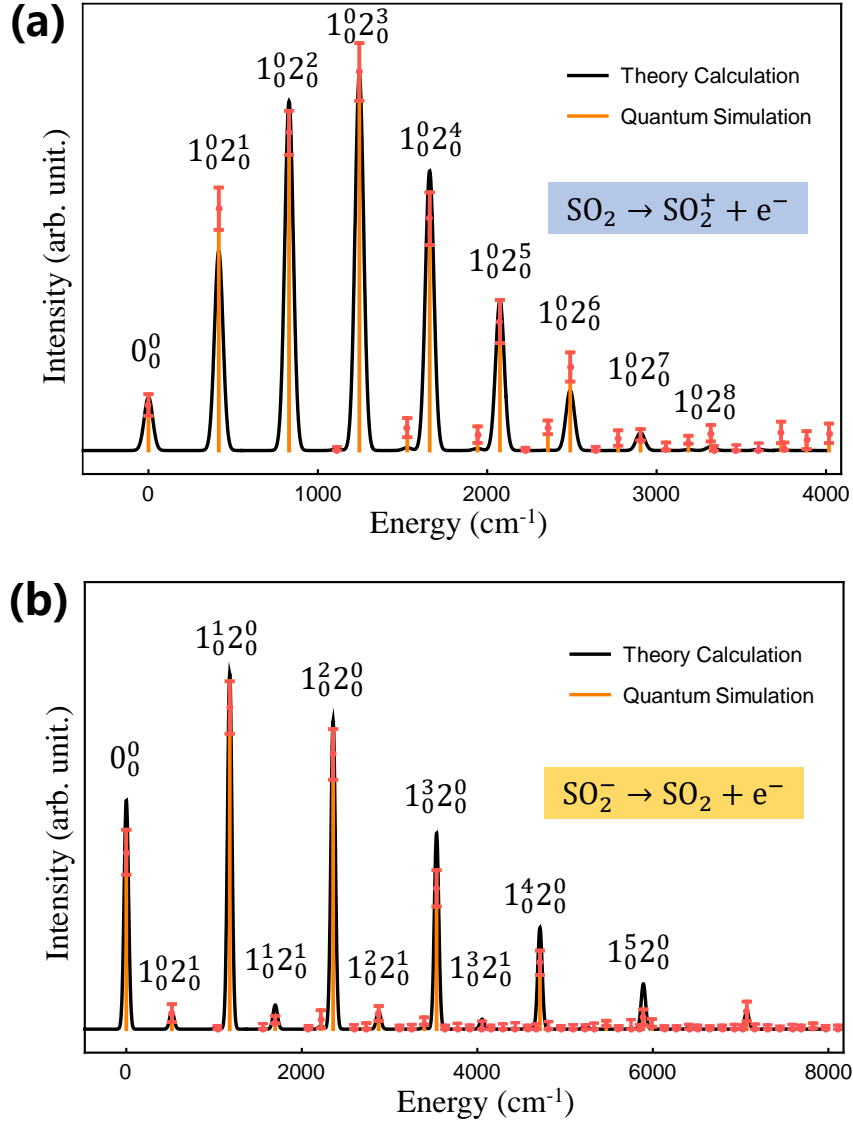
图 6.11　Trapped-ion simulation of photoelectron spectra of SO_2 and SO_2^- with measurement-error correction. The two vibrational frequencies of harmonic potential for SO_2^+, SO_2 and SO_2^- are (1112.7, 415.0), (1178.4, 518.9) and (989.5, 451.4) cm^{-1}, respectively. (a) The displacement vector α is (-0.026, 1.716); rotation angle θ is 0.189 and (b) The displacement vector α is (1.360, -0.264); rotation angle θ is 0.065. The theoretical lines are intentionally broadened by convoluting with a Gaussian function with the width of 50 cm^{-1} [95] for the comparison. Here N_0^i denotes the i-phonon excitation on N-th mode from the vibrational ground state $|0\rangle$, and accordingly, 0_0^0 located at the off-set energy $\omega_{0-0} = 0$.

6.6 Discussion and conclusions

As the first demonstration of quantum simulation for the molecular vibronic spectroscopy, our trapped-ion device shows excellent performance at a small-scale after the error-correction scheme in section 6.4.2. In the near future, we expect the many modes implementation for a large-scale molecular simulation, where the multi-modes can be mapped to the local vibrational modes or collective normal modes of many ions in a single trap. The demonstrated quantum optical operations through a single ion will be directly applied to the large-scale simulation. This would be useful in concluding the quantum supremacy of boson sampling with the Gaussian states. The molecular simulations in trapped-ion devices and the real molecular spectroscopic signals can be compared as a certification protocol for large-scale Gaussian boson sampling, which cannot be verified classically because of the #P-hardness[74–76] (cf. Neville et al.[103] and Clifford[104] for the classical effort to reach the classical limit of the original boson sampling problem). In closing, we would like to comment on the possible extension of the quantum simulation of molecular vibronic spectra, which are currently in preparation: (i) One could possibly go beyond the Condon approximation, i.e., the coordinate dependence of the transition dipole moment, by introducing additional phase to the input Gaussian states; (ii) The anharmonic problem, which is more challenging, can be incorporated in the molecular process for example with Morse-oscillators [105,106]. Moreover, we may adopt the quantum simulation of spin-boson model[107] or many-body bosonic-fermionic systems[108] for further vibronic simulation beyond the Born-Oppenheimer approximation.

第7章　Conclusion and outlook

During my Ph.D. career, joined with my team members, we have built a trapped ion system that can completely control a single ion, where the operation Hilbert space includes the four-level system and the two motional modes. We can initialize the state of the ion to hyperfine ground state and motional ground state, and manipulate the ion through the microwave and pulsed laser. As a preparation work for the multi-ions system, I developed the detection scheme with an EMCCD and trying to improve the number of electrodes in the segmented blade trap. Besides that, I contribute to the stabilization of lasers and enhance the coherence time of internal state and motional state.

For the molecular electronic structure simulation, I implemented the variational algorithm for the molecular ground state energy problem in our trapped ion system and shown excellent performance. For the molecular vibronic spectroscopy emulation experiment, I explored the implementation of quantum optical operations with spin-dependent and spin-independent schemes, and realize the collective projection measurement for two bosonic modes in a single ion.

There are a lot of technical issues that need to be addressed for a more robust trapped ion system. We need to carefully study and enhance the coherence time of the qubit, especially the motional modes, which is an information transfer bus for the multi-ion system. The detection system with EMCCD should be further improved to reach a higher readout fidelity. The next generation of our blade trap will include more electrodes, which is a benefit for the uniform spacing of an ion chain.

A long-lived, large number ion crystal, which prevents from ion crystal melting or ion escaping, is indispensable for the realization of future trapped ion quantum computer. One promising direction is putting our vacuum chamber in a cryogenic system, which significantly reduces the background collision. And the short term alternative is using the ion protection sequence, which requires the monitoring of Doppler cooling count and feedback to a conditional experimental sequence control system.

Limited by the number of ions in our system for the past years, we are establishing the multi-ion system at present, and I am looking forward to the demonstration of quantum chemistry algorithms in the next multi-ions system, which may show the strong power of a quantum computer.

插图索引

表格索引

公式索引

公式索引

参考文献

[1] Feynman R P. Simulating physics with computers[J]. International Journal of Theoretical Physics, 1982, 21: 467–488.

[2] Lloyd S. Universal quantum simulators[J/OL]. Science, 1996, 273: 1073–1077. http://research. physics.illinois.edu/demarco/lloyd96paper.pdf.

[3] Georgescu I, Ashhab S, Nori F. Quantum simulation[J]. Reviews of Modern Physics, 2014, 86 (1): 153.

[4] Greiner M, Mandel O, Esslinger T, et al. Quantum phase transition from a superfluid to a mott insulator in a gas of ultracold atoms[J]. Nature, 2002, 415(6867): 39–44.

[5] Kim K, Chang M, Korenblit S, et al. Quantum simulation of frustrated ising spins with trapped ions[J]. Nature, 2010, 465(7298): 590–593.

[6] Kandala A, Mezzacapo A, Temme K, et al. Hardware-efficient variational quantum eigensolver for small molecules and quantum magnets[J]. Nature, 2017, 549(7671): 242.

[7] Zhang J, Pagano G, Hess P W, et al. Observation of a many-body dynamical phase transition with a 53-qubit quantum simulator[J]. Nature, 2017, 551(7682): 601.

[8] Bernien H, Schwartz S, Keesling A, et al. Probing many-body dynamics on a 51-atom quantum simulator[J]. Nature, 2017, 551(7682): 579.

[9] Helgaker T, Jorgensen P, Olsen J. Molecular electronic-structure theory[M]. [S.l.]: John Wiley & Sons, 2014

[10] Kassal I, Whitfield J D, Perdomoortiz A, et al. Simulating chemistry using quantum computers - annual review of physical chemistry, 62(1):185[J]. Annual Review of Physical Chemistry, 2011, 62: 185–185.

[11] Lu D, Xu B, Xu N, et al. Quantum chemistry simulation on quantum computers: theories and experiments[J]. Physical Chemistry Chemical Physics, 2012, 14(26): 9411–9420.

[12] Aspuru-Guzik A, Dutoi A D, Love P J, et al. Simulated quantum computation of molecular energies[J]. Science, 2005, 309: 1704–1707.

[13] Wecker D, Bauer B, Clark B K, et al. Gate-count estimates for performing quantum chemistry on small quantum computers[J]. Physical Review A, 2014, 90(2): 022305.

[14] McClean J R, Babbush R, Love P J, et al. Exploiting locality in quantum computation for quantum chemistry[J/OL]. Journal of Physical Chemistry Letters, 2014, 5(24): 4368–4380. http://dx.doi.org/10.1021/jz501649m.

[15] DiVincenzo D P, et al. The physical implementation of quantum computation[J]. arXiv preprint quant-ph/0002077, 2000.

[16] Paul W. Electromagnetic traps for charged and neutral particles[J]. Reviews of Modern Physics, 1990, 62(3): 531–540.

[17] Monroe C. Quantum information processing with atoms and photons.[J]. Nature, 2002, 416 (6877): 238–246.

[18] Olmschenk S M. Quantum teleportation between distant matter qubits[D]. [S.l.]: University of Michigan, 2009.

[19] Liebfried D, Blatt R, Monroe C, et al. Quantum dynamics of single trapped ions[J]. Review of Modern Physics, 2003, 75: 281–324.

[20] Macalpine W, Schildknecht R. Coaxial resonators with helical inner conductor[J]. Proceedings of the IRE, 1959, 47(12): 2099–2105.

[21] Wang Y, Um M, Zhang J, et al. Single-qubit quantum memory exceeding ten-minute coherence time[J]. Nature Photonics, 2017, 11(10): 646.

[22] Balzer C, Braun A, Hannemann T, et al. Electrodynamically trapped yb$^+$ ions for quantum information processing[J]. Physical Review A, 2006, 73(4): 041407.

[23] Roberts M, Taylor P, Gateva-Kostova S, et al. Measurement of the 2 s 1/2- 2 d 5/2 clock transition in a single 171 yb+ ion[J]. Physical Review A, 1999, 60(4): 2867.

[24] Stick D L. Fabrication and characterization of semiconductor ion traps for quantum information processing[D]. [S.l.]: University of Michigan, 2007.

[25] Wineland D J, Monroe C, Itano W M, et al. Experimental issues in coherent quantum-state manipulation of trapped atomic ions[J]. Journal of Research of the National Institute of Standards and Technology, 1998, 103(3): 259–328.

[26] Nagourney W, Sandberg J, Dehmelt H. Shelved optical electron amplifier: Observation of quantum jumps[J]. Physical Review Letters, 1986, 56(26): 2797.

[27] Bergquist J, Hulet R G, Itano W M, et al. Observation of quantum jumps in a single atom[J]. Physical Review Letters, 1986, 57(14): 1699.

[28] Blatt R, Zoller P. Quantum jumps in atomic systems[J]. European Journal of Physics, 1988, 9 (4): 250.

[29] King B E. Quantum state engineering and information processing with trapped ions[D]. [S.l.]: University of Colorado, 1999.

[30] Acton M. Detection and control of individual trapped ions and neutral atoms[D]. [S.l.]: University of Michigan, 2008.

[31] Basden A, Haniff C A, Mackay C D. Photon counting strategies with low-light-level ccds[J]. Monthly Notices of the Royal Astronomical Society, 2003, 345(3): 985–991.

[32] Myerson A H, Szwer D J, Webster S C, et al. High-fidelity readout of trapped-ion qubits[J]. Physical Review Letters, 2008, 100(20): 200502.

[33] Noek R, Vrijsen G, Gaultney D, et al. High speed, high fidelity detection of an atomic hyperfine qubit[J]. Optics Letters, 2013, 38(22): 4735–4738.

[34] Shen C, Duan L. Correcting detection errors in quantum state engineering through data processing[J]. New Journal of Physics, 2012, 14(5): 053053.

[35] Drever R W P, Hall J L, Kowalski F V, et al. Laser phase and frequency stabilization using an optical resonator[J]. Applied Physics B, 1983, 31(2): 97–105.

[36] Mueck L. Quantum reform[J]. Nature Chemistry, 2015, 7: 361–363.

[37] Yung M H, Whitfield J D, Boixo S, et al. Introduction to Quantum Algorithms for Physics and Chemistry[J]. Advances in Chemical Physics, 2012, 154: 67.

[38] Aspuru-Guzik A, Walther P. Photonic quantum simulators[J]. Nature Physics, 2012, 8: 285–291.

[39] Yung M H, Casanova J, Mezzacapo A, et al. From transistor to trapped-ion computers for quantum chemistry.[J]. Scientific Reports, 2014, 4: 3589.

[40] Lanyon B P, Whitfield J D, Gillett G G, et al. Towards quantum chemistry on a quantum computer[J]. Nature chemistry, 2010, 2(2): 106.

[41] Du J, Xu N, Peng X, et al. Nmr implementation of a molecular hydrogen quantum simulation with adiabatic state preparation[J]. Physical Review Letters, 2010, 104(3): 030502.

[42] Peruzzo A, McClean J, Shadbolt P, et al. A variational eigenvalue solver on a quantum processor [J]. Nature Communications, 2014, 5: 4213.

[43] Wang Y, Dolde F, Biamonte J, et al. Quantum simulation of helium hydride cation in a solid-state spin register[J]. ACS nano, 2015, 9(8): 7769–7774.

[44] O'Malley P, Babbush R, Kivlichan I, et al. Scalable quantum simulation of molecular energies [J]. Physical Review X, 2016, 6(3): 031007.

[45] Paesani S, Gentile A A, Santagati R, et al. Experimental bayesian quantum phase estimation on a silicon photonic chip[J]. Physical Review Letters, 2017, 118(10): 100503.

[46] Shen Y, Zhang X, Zhang S, et al. Quantum implementation of the unitary coupled cluster for simulating molecular electronic structure[J/OL]. Physical Review A, 2017, 95: 020501. https://link.aps.org/doi/10.1103/PhysRevA.95.020501.

[47] Hastings M B, Wecker D, Bauer B, et al. Improving quantum algorithms for quantum chemistry [J/OL]. Quantum Information & Computation, 2015, 15(1-2): 1–21. http://dl.acm.org/citation. cfm?id=2685188.2685189.

[48] Poulin D, Hastings M B, Wecker D, et al. The trotter step size required for accurate quantum simulation of quantum chemistry[J/OL]. Quantum Information & Computation, 2015, 15(5-6): 361–384. http://dl.acm.org/citation.cfm?id=2871401.2871402.

[49] Babbush R, Mcclean J, Wecker D, et al. Chemical basis of trotter-suzuki errors in quantum chemistry simulation[J]. Physical Review A, 2015, 91(2): 022311.

[50] Aaronson S. Computational complexity: Why quantum chemistry is hard[J]. Nature Physics, 2009, 5(10): 707–708.

[51] Whitfield J D, Love P J, Aspuru-Guzik A. Computational complexity in electronic structure. [J]. Physical Chemistry Chemical Physics, 2013, 15(2): 397–411.

[52] Farhi E, Goldstone J, Gutmann S, et al. A quantum adiabatic evolution algorithm applied to random instances of an np-complete problem[J]. Science, 2001, 292: 472.

[53] Johnson M W, Amin M H S, Gildert S, et al. Quantum annealing with manufactured spins[J]. Nature, 2011, 473: 194–198.

[54] Baugh J, Moussa O, Ryan C A, et al. Experimental implementation of heat-bath algorithmic cooling using solid-state nuclear magnetic resonance[J]. Nature, 2005, 438: 470–473.

[55] Barreiro J T, Müller M, Schindler P, et al. An open-system quantum simulator with trapped ions [J]. Nature, 2011, 470: 486–491.

[56] Lin Y, Gaebler J P, Reiter F, et al. Dissipative production of a maximally entangled steady state of two quantum bits[J]. Nature, 2013, 504: 415–420.

[57] Xu J S, Yung M H, Xu X Y, et al. Demon-like algorithmic quantum cooling and its realization with quantum optics[J]. Nature Photonics, 2014, 8: 113–118.

[58] Kitaev A Y. Quantum measurements and the abelian stabilizer problem[J]. arXiv preprint quant-ph/9511026, 1995.

[59] Bartlett R J, Musiał M. Coupled-cluster theory in quantum chemistry[J]. Reviews of Modern Physics, 2007, 79: 291–352.

[60] Shavitt I, Bartlett R. Cambridge molecular science: Many-body methods in chemistry and physics: Mbpt and coupled-cluster theory[M]. [S.l.]: Cambridge University Press, 2009

[61] Čársky P, Paldus J, Pittner J. Recent progress in coupled cluster methods[M]. [S.l.]: Springer, Netherlands, 2010

[62] Atkins P W, Friedman R. Molecular quantum mechanics[M]. [S.l.]: Oxford University Press, 2011

[63] Chan G K L, Kállay M, Gauss J. State-of-the-art density matrix renormalization group and coupled cluster theory studies of the nitrogen binding curve.[J]. Journal of Chemical Physics, 2004, 121(13): 6110–6116.

[64] Taube A G, Bartlett R J. New perspectives on unitary coupled-cluster theory[J]. International Journal of Quantum Chemistry, 2006, 106(15): 3393–3401.

[65] Szabo A, Ostlund N S. Modern quantum chemistry: introduction to advanced electronic structure theory[M]. [S.l.]: Courier Corporation, 2012

[66] Zhang X, Um M, Zhang J, et al. State-independent experimental tests of quantum contextuality in a three dimensional system[J]. Physical Review Letters, 2013, 110: 070401.

[67] Zhang X, Shen Y, Zhang J, et al. Time reversal and charge conjugation in an embedding quantum simulator[J]. Nature Communications, 2014, 6: 7917.

[68] Thompson J R. Simulation: a modeler's approach: volume 522[M]. [S.l.]: John Wiley & Sons, 2009

[69] Sheehy B, DiMauro L F. Atomic and molecular dynamics in intense optical fields[J]. Annual Review of Physical Chemistry, 1996, 47(1): 463–494.

[70] Casanova J, Mezzacapo A, Lamata L, et al. Quantum simulation of interacting fermion lattice models in trapped ions[J/OL]. Physical Review Letters, 2012, 108: 190502. http://link.aps.org/doi/10.1103/PhysRevLett.108.190502.

[71] Lanyon B P, Hempel C, Nigg D, et al. Universal digital quantum simulation with trapped ions [J/OL]. Science, 2011, 334(6052): 57–61. http://science.sciencemag.org/content/334/6052/57.

[72] Houck A A, Türeci H E, Koch J. On-chip quantum simulation with superconducting circuits[J]. Nature Physics, 2012, 8(4): 292–299.

[73] Lund A P, Laing A, Rahimi-Keshari S, et al. Boson Sampling from a Gaussian state[J]. Physical Review Letters, 2014, 113(10): 100502.

[74] Rahimi-Keshari S, Lund A P, Ralph T C. What can quantum optics say about complexity theory? [J]. Physical Review Letters, 2015, 114: 060501.

[75] Huh J, Guerreschi G G, Peropadre B, et al. Boson sampling for molecular vibronic spectra[J]. Nature Photonics, 2015, 9: 615–620.

[76] Huh J, Yung M H. Hierarchy in sampling gaussian-correlated bosons[J]. Scientific Reports, 2016, 7(1).

[77] Shen Y, Lu Y, Zhang K, et al. Quantum optical emulation of molecular vibronic spectroscopy using a trapped-ion device[J/OL]. Chemical Science, 2018, 9: 836–840. http://dx.doi.org/10.1039/C7SC04602B.

[78] Aaronson S, Arkhipov A. The computational complexity of linear optics[J]. Proceedings of the 43rd annual ACM symposium on Theory of computing - STOC '11, 2011: 333.

[79] Spring J B, Metcalf B J, Humphreys P C, et al. Boson sampling on a photonic chip[J]. Science, 2013, 339: 798–801.

[80] Broome M A, Fedrizzi A, Rahimi-Keshari S, et al. Photonic boson sampling in a tunable circuit [J]. Science, 2013, 339: 794–798.

[81] Crespi A, Osellame R, Ramponi R, et al. Integrated multimode interferometers with arbitrary designs for photonic boson sampling[J]. Nature Photonics, 2013, 7(July): 545–549.

[82] Tillmann M, Dakic B, Heilmann R, et al. Experimental boson sampling[J]. Nature Photonics, 2013, 7: 540–544.

[83] Spagnolo N, Vitelli C, Bentivegna M, et al. Experimental validation of photonic boson sampling [J]. Nature Photonics, 2014, 8(8): 615–620.

[84] Carolan J, Meinecke J D a, Shadbolt P J, et al. On the experimental verification of quantum complexity in linear optics[J]. Nature Photonics, 2014, 8(8): 621–626.

[85] Wikipedia. Boson sampling[EB/OL]. https://en.wikipedia.org/wiki/Boson_sampling.

[86] Wikipedia. Franck–condon principle[EB/OL]. https://en.wikipedia.org/wiki/Franck-Condon_principle.

[87] Jankowiak H C, Stuber J L, Berger R. Vibronic transitions in large molecular systems: Rigorous prescreening conditions for Franck-Condon factors[J]. Journal of Chemical Physics, 2007, 127: 234101.

[88] Braunstein S L. Squeezing as an irreducible resource[J]. Physical Review A, 2005, 71: 1–4.

[89] Doktorov E V, Malkin I A, Man'ko V I. Dynamical symmetry of vibronic transitions in polyatomic molecules and the Franck-Condon principle[J]. Journal of Molecular Spectroscopy, 1977, 64: 302–326.

[90] Ma X, Rhodes W. Multimode squeeze operators and squeezed states.[J]. Physical Review A, 1990, 41(9): 4625–4631.

[91] Lau H K, James D F V. A proposal for a scalable universal bosonic simulator using individually trapped ions[J]. Physical Review A, 2012, 85(6): 059905.

[92] Shen C, Zhang Z, Duan L M. Scalable implementation of boson sampling with trapped ions[J]. Physical Review Letters, 2014, 112(5): 050504.

[93] Peropadre B, Guerreschi G G, Huh J, et al. Microwave Boson Sampling[J]. Physical Review Letters, 2016, 117: 140505.

[94] Nimlos M R, Ellison G B. Photoelectron spectroscopy of sulfur-containing anions (so2-, s3-, and s2o-)[J/OL]. The Journal of Physical Chemistry, 1986, 90(12): 2574–2580. https://doi.org/10.1021/j100403a007.

[95] Lee C L, Yang S H, Kuo S Y, et al. A general formula of two-dimensional Franck–Condon integral and the photoelectron spectroscopy of sulfur dioxide[J]. Journal of Molecular Spectroscopy, 2009, 256: 279–286.

[96] Monroe C, Meekhof D M, King B E, et al. Demonstration of a fundamental quantum logic gate [J]. Physical Review Letters, 1995, 75: 4714–4717.

[97] Roos C, Zeiger T, Rohde H, et al. Quantum state engineering on an optical transition and decoherence in a paul trap[J]. Physical Review Letters, 1999, 83: 4713–4716.

[98] Frisch M J, Trucks G W, Schlegel H B, et al. Gaussian~16 Revision A.03[M]. [S.l.: s.n.], 2016.

[99] Meekhof D M, Monroe C, King B E, et al. Generation of nonclassical motional states of a trapped atom[J]. Physical Review Letters, 1996, 76: 1796–1799.

[100] Toyoda K, Hiji R, Noguchi A, et al. Hong-ou-mandel interference of two phonons in trapped ions.[J]. Nature, 2015, 527(7576): 74–77.

[101] Um M, Zhang J, Lv D, et al. Phonon arithmetic in a trapped ion system[J]. Nature Communications, 2016, 7: 11410.

[102] Zhang J, Um M, Lv D, et al. Experimental preparation of high noon states for phonons[J]. arXiv:1611.08700, 2016.

[103] Neville A, Sparrow C, Clifford R, et al. Classical boson sampling algorithms with superior performance to near-term experiments[J]. Nature Physics, 2017: 4270.

[104] Clifford P, Clifford R. The classical complexity of boson sampling[J]. arXiv:1706.01260v1, 2017.

[105] Iachello F, Ibrahim M. Analytic and algebraic evaluation of franck-condon overlap integrals[J]. Journal of Physical Chemistry A, 1998, 102: 9427.

[106] Olivares D G, Peropadre B, Huh J, et al. Quantum emulation of molecular force fields: A blueprint for a superconducting architecture[J/OL]. Physical Review Applied, 2017, 8: 064008. https://link.aps.org/doi/10.1103/PhysRevApplied.8.064008.

[107] Lemmer A, Cormick C, Tamascelli D, et al. Simulating spin-boson models with trapped ions [J]. arXiv: 1704.00629, 2017.

[108] Mezzacapo A, Casanova J, Lamata L, et al. Digital Quantum Simulation of the Holstein Model in Trapped Ions[J]. Physical Review Letters, 2012, 109: 200501.

致　谢

Foremost, I would like to express my sincere gratitude to my advisor Prof. Kihwan Kim for the continuous support of my Ph.D. study and related research, for his patience, motivation, and immense knowledge. Under your guidance, I grow from a fresh student to an independent researcher in the trapped ion laboratory. The encouragement you give to me when I face difficulties, and the ability of logic thinking you taught to me, will be a precious asset for my life, and never fade away.

Besides my advisor, I would like to thank Prof. Man-Hong Yung and Prof. Joonsuk Huh for their theoretical collaborations and the patient guidance, especially the enjoyable discussions, which offers me a fantastic journey in the quantum chemistry field.

I am especially grateful for my lab-mates who accompany my past six years: Dahyun Yum, Zhang Xiang, Um Mark, Wang Ye, Zhang Junhua, Lv Dingshun, An Shuoming, Zhang Kuan, Lu Yao, Zhang Shuaining, Wang Pengfei, Cheng Wentao and Qiao Mu. The time we were struggling together and the moments we made great achievement add so much positive gain to my research life. I would also like to thank all the members in CQI, for the pleasant times and forever friendship.

Last but not the least, I would like to thank my parents, for raising me up and supporting me spiritually throughout my life. A special thanks to my wife, Jin Xinyi, I can not imagine how can I accomplish my Ph.D. carrier without your full support.

声 明

本人郑重声明：所呈交的学位论文，是本人在导师指导下，独立进行研究工作所取得的成果。尽我所知，除文中已经注明引用的内容外，本学位论文的研究成果不包含任何他人享有著作权的内容。对本论文所涉及的研究工作做出贡献的其他个人和集体，均已在文中以明确方式标明。
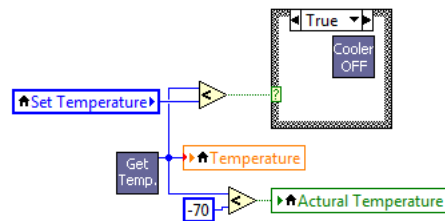
签　名：_____ 日　期：_____

附录 A　Labview code for acquiring data by Andor EMCCD

System initialization

Temperature stabilization

Setting parameters
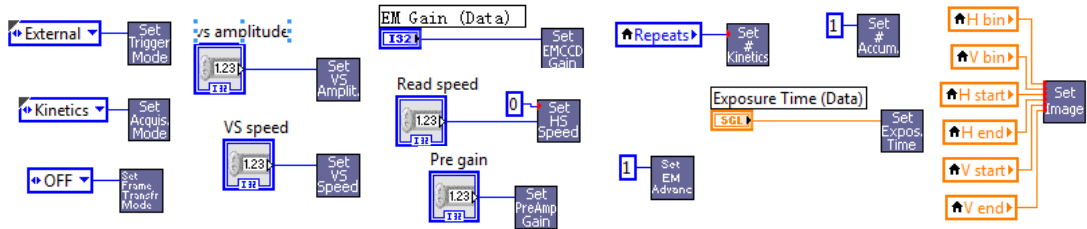
Data acquiring
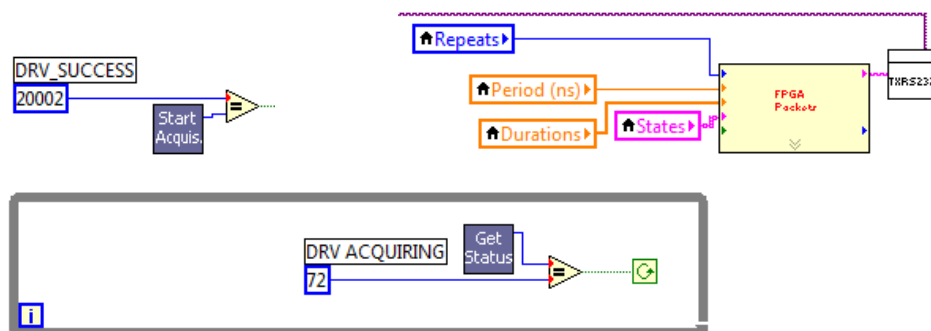
Fitting experimental data
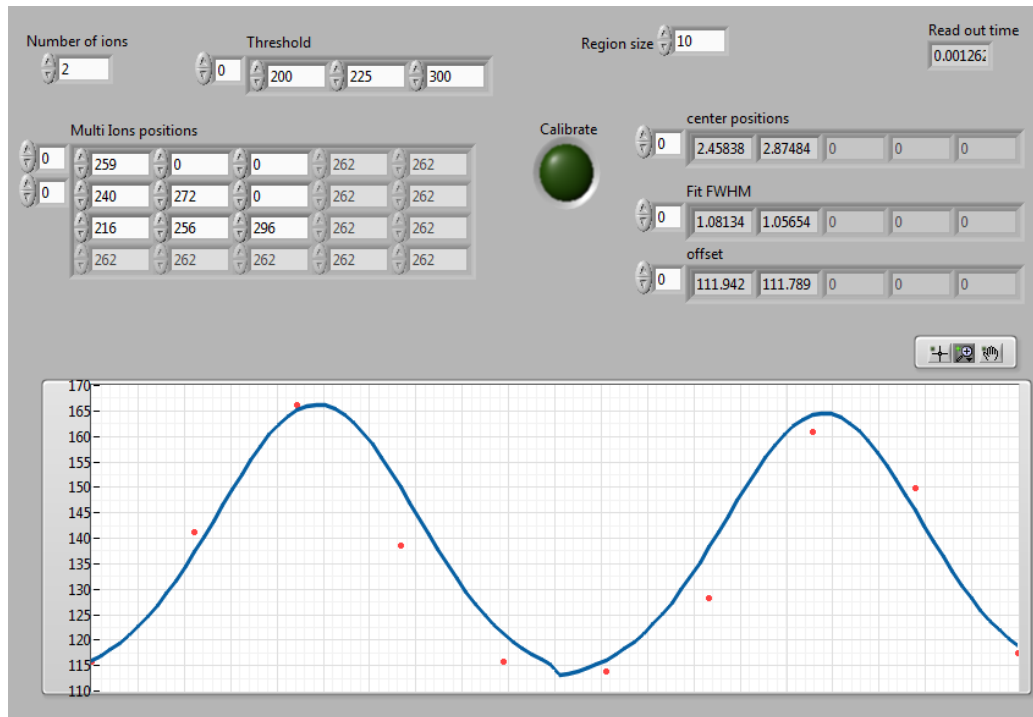
Data processing
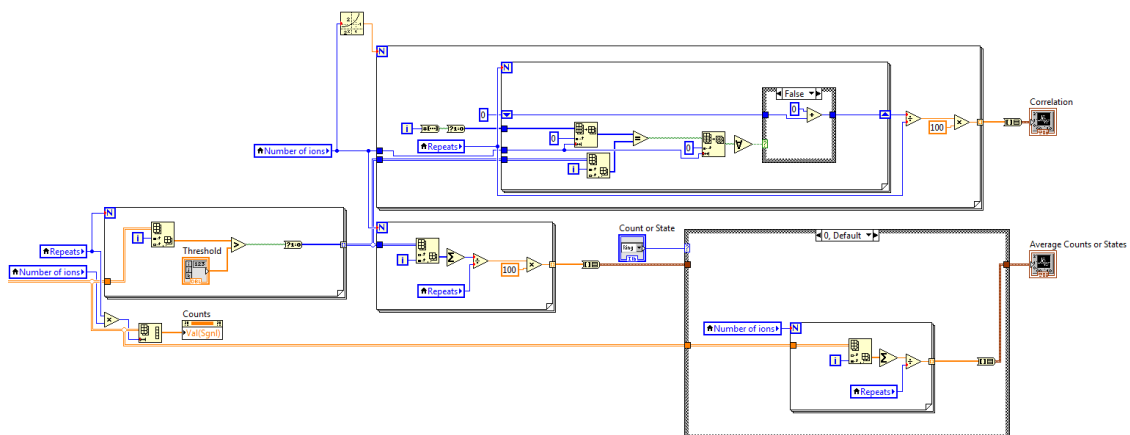
附录 B　Mathematica code for the control of DDS

Needs["NETLink"]

Declaration

ClearAll[DDSCards, DDSHandle, IsConnected, DDSGetPortValue, DDSSetPortValue,

FormatWData, FormatRData, GetRegLen, GetEvbdInfo, DDSGetRegValue,

DDSSetRegValue, MasterReset, TriggerIOUpdate, TriggerIOReset,

SetCurrentProfile, DDSInit, AlignPhase, DriveLetter];

DriveLetter[] = If[$Input(*FileName*)==="",

If[DirectoryQ[# <> "\\"]&&DirectoryQ[# <> "\\Mathematica"]&&

DirectoryQ[# <> "\\Data"], #, "E:"]

&@If[$UserName==="lab2", "F:", "G:"],

FileNameSplit[$Input(*FileName*)][[1]]

];

DDSHandles = {};

RegLength = {4, 4, 4, 4, 4, 6, 6, 4, 2, 4, 4, 8, 8, 4, 8, 8, 8, 8, 8, 8, 8, 8, 4};

SYSCLK = 1000;

dUpdate = MakeNETObject[{255, 5, 0}, "System.Byte[]"];

Protected

AdiClockLib =

FileNameJoin@{"G:", "LabVIEW", "Lib", "ad9910", "adiclockeval.dll"};

FindHardware = DefineDLLFunction["FindHardware", AdiClockLib, "int",

{"int*", "int*", "int"}];

GetHardwareHandles = DefineDLLFunction["GetHardwareHandles", AdiClockLib,

"void", {"unsigned int[]"}];

IsConnected = DefineDLLFunction["IsConnected", AdiClockLib, "int", {"int"}];

GetPortValue = DefineDLLFunction["GetPortValue", AdiClockLib, "int",

{"int", "int", "unsigned int[]"}];

SetPortValue = DefineDLLFunction["SetPortValue", AdiClockLib, "int",

```
{"int", "int", "char"}];
SpiRead = DefineDLLFunction["SpiRead", AdiClockLib, "int",
{"int", "System.Byte[]", "int", "System.Byte[]", "int", "int"}];
SpiWrite = DefineDLLFunction["SpiWrite", AdiClockLib, "int",
{"int", "System.Byte[]", "int"}];
GetEvbdInfo = DefineDLLFunction["GetEvbdInfo", AdiClockLib, "void",
{"int", "System.Byte[]", "ref System.UInt32"}];
```

Function

```
DDSCards[]:=Module[{vid, pid, num, handles},
vid = 1110;
pid = 60965;
num = FindHardware[vid, pid, 1];
DDSHandles = Range[0, num − 1];
handles = MakeNETObject@ConstantArray[0, num];
GetHardwareHandles[handles];
DDSHandles = NETObjectToExpression@handles];
DDSCards[];


DDSHandle[id_Integer]:=DDSHandles[[id]];
DDSGetPortValue[id_Integer, port_Integer]:=Module[{val, ret},
val = MakeNETObject@{0};
GetPortValue[DDSHandle[id], port, val];
(NETObjectToExpression@val)[[1]]];


DDSSetPortValue[id_Integer, port_Integer, val_Integer]:=
SetPortValue[DDSHandle[id], port, val];


FormatWData[dat_Integer]:=
{Mod[#, 256], Quotient[#, 256]}&[
2FromDigits[Riffle[IntegerDigits[dat, 2, 8], 0], 2]];


FormatWData[dat_List]:=Flatten[Reverse[FormatWData/@dat]];
```

119

FormatRData[dat_List]:=

FromDigits[#, 2]&/@

Partition[Flatten[Reverse[Drop[IntegerDigits[#, 2, 8], {2, 8, 2}]&/@dat]],

8];

GetRegLen[reg_Integer]:=RegLength[[reg + 1]];

DDSGetRegValue[id_Integer, reg_Integer]:=Module[{wdat, len, rdat, ret},

wdat = MakeNETObject[FormatWData[128 + reg], "System.Byte[]"];

len = GetRegLen[reg];

rdat = MakeNETObject[ConstantArray[0, 2len], "System.Byte[]"];

SpiRead[DDSHandle[id], wdat, 2, rdat, 2len, 0];

FormatRData[NETObjectToExpression@rdat]];

DDSSetRegValue[id_Integer, reg_Integer, val_List]:=Module[{buf},

buf = MakeNETObject[FormatWData[Prepend[val, reg]], "System.Byte[]"];

SpiWrite[DDSHandle[id], buf, 2Length[val] + 2];];

DDSGetEvbdInfo[id_Integer]:=Module[{info, len, rtl, rti},

info = MakeNETObject[ConstantArray[0, 32], "System.Byte[]"];

len = MakeNETObject[32, "System.UInt32"];

GetEvbdInfo[DDSHandle[id], info, len];

rtl = NETObjectToExpression@len;

rti = (NETObjectToExpression@info)[[1;;rtl]];

rti];

Definition - Utilities

MasterReset[id_Integer]:=Module[{val},

val = BitAnd[DDSGetPortValue[id, 0], 2^^11110111];

DDSSetPortValue[id, 0, val];

DDSSetPortValue[id, 0, val + 8];

DDSSetPortValue[id, 0, val];];

```
TriggerIOUpdate[id_Integer]:=Module[{val},
val = BitAnd[DDSGetPortValue[id, 4], 2^^11101111];
DDSSetPortValue[id, 4, val];
DDSSetPortValue[id, 4, val + 16];
DDSSetPortValue[id, 4, val]; ];


TriggerIOReset[id_Integer]:=Module[{val},
val = BitAnd[DDSGetPortValue[id, 0], 2^^11111011];
DDSSetPortValue[id, 0, val];
DDSSetPortValue[id, 0, val + 4];
DDSSetPortValue[id, 0, val]; ];


SetCurrentProfile[id_Integer, prof_Integer]:=Module[{val},
val = BitAnd[DDSGetPortValue[id, 4], 2^^11111000];
DDSSetPortValue[id, 4, val + prof]; ];


DDSInit[id_Integer]:=Module[{},
MasterReset[id];
DDSSetRegValue[id, 0, {16^^00, 16^^40, 16^^00, 16^^00}];
DDSSetRegValue[id, 1, {16^^01, 16^^40, 16^^08, 16^^A0}];
DDSSetRegValue[id, 2, {16^^1F, 16^^3F, 16^^C0, 16^^00}];
DDSSetRegValue[id, 3, {16^^00, 16^^00, 16^^7F, 16^^FF}];
DDSSetRegValue[id, 16^^0A, {16^^7C, 16^^00, 16^^40, 16^^00}];
DDSSetRegValue[id, 16^^0E,
{16^^3F, 16^^FF, 16^^00, 16^^00, 16^^33, 16^^33, 16^^33, 16^^33}];
TriggerIOUpdate[id]; ];


ReadProfile[id_Integer, prof_Integer]:=Module[{tmp, buf, f, p, a},
tmp = DDSGetPortValue[id, 4];
SetCurrentProfile[id, prof];
buf = FromDigits[DDSGetRegValue[id, 16^^0E + prof], 256];
DDSSetPortValue[id, 4, tmp];
```

f = Mod $\left[\text{buf}, 2^{32}\right]$ SYSCLK $/2^{32}$;

p = Mod $\left[\text{BitShiftRight[buf, 32]}, 2^{16}\right] 2\pi /2^{16}$;

a = Mod $\left[\text{BitShiftRight[buf, 48]}, 2^{14}\right] /2^{14}$;

{f, p, a}];

WriteProfile[id_Integer, prof_Integer, {f_, p_, a_}]:=

Module[{tmp, ftw, pow, asf},

ftw = Round $\left[2^{32}\text{f/SYSCLK}\right]$;

pow = BitShiftLeft $\left[\text{Round}\left[2^{16}\text{Mod[p, }2\pi\text{]}/(2\pi)\right], 32\right]$;

asf = BitShiftLeft $\left[\text{Round}\left[2^{14}\text{Min}\left[\text{a}, 1 - 2^{-14}\right]\right], 48\right]$;

tmp = DDSGetPortValue[id, 4];

SetCurrentProfile[id, prof];

DDSSetRegValue[id, 16^^0E + prof, IntegerDigits[asf + pow + ftw, 256, 8]];

DDSSetPortValue[id, 4, tmp];

TriggerIOUpdate[id];];

AlignPhase[]:=Module[{},

DDSInit/@Range[4];

Pause[0.1];

WriteProfile[1, 0, {200, 355°, 1}];

WriteProfile[#, 1, {200, 0, 1}]&/@Range[4];

DDSSetRegValue[#, 0, {16^^00, 16^^40, 16^^08, 16^^00}]&/@Range[4];

Pause[0.1];

TriggerIOUpdate/@Range[4];

DDSSetRegValue[#, 0, {16^^00, 16^^40, 16^^20, 16^^00}]&/@Range[4];];

附录 C　The classical calculation of HeH$^+$

Basic Functions

$\zeta 1 = 2.0925; \zeta 2 = 1.24; \zeta 1p = 2.0925/1.24;$

$c1 = 0.444635; e11 = 0.109818\zeta 1^2; e12 = 0.109818\zeta 2^2;$

$e11p = 0.3136497915; e12p = 0.16885540;$

$c2 = 0.535328; e21 = 0.405771\zeta 1^2; e22 = 0.405771\zeta 2^2;$

$e21p = 1.158922999; e22p = 0.623913;$

$c3 = 0.154329; e31 = 2.22766\zeta 1^2; e32 = 2.22766\zeta 2^2;$

$e31p = 6.362421394; e32p = 3.425250914;$

$SF[\zeta\_][r\_] := \sqrt{\frac{\zeta^3}{\pi}} e^{-\zeta r};$

$GF[a\_][r\_] := \left(\frac{2a}{\pi}\right)^{3/4} e^{-ar^2};$

$CGF[c1\_][e1\_][c2\_][e2\_][c3\_][e3\_][r\_] := c1\,GF[e1][r] + c2\,GF[e2][r] + c3\,GF[e3][r];$

$ccoeff[i\_] := \{c1, c2, c3\}[[i]];$

$expcoeff[i\_][j\_] := \{\{e11p, e21p, e31p\}, \{e12p, e22p, e32p\}\}[[i, j]];$

$IS[i\_][j\_][RA\_][RB\_] := \left(\frac{4i*j}{\pi^2}\right)^{3/4} \left(\frac{\pi}{i+j}\right)^{3/2} Exp\left[\frac{-ij}{i+j}(RA - RB)^2\right];$

$Ir[i\_][j\_][RA\_][RB\_] := \left(\frac{4i*j}{\pi^2}\right)^{3/4} \left(\frac{\pi}{i+j}\right)^{3/2} \frac{iRA+jRB}{i+j} Exp\left[\frac{-ij}{i+j}(RA - RB)^2\right];$

$IK[i\_][j\_][RA\_][RB\_] := \left(\frac{4i*j}{\pi^2}\right)^{3/4} \frac{ij}{i+j} \left(3 - \frac{2ij}{i+j}(RA - RB)^2\right) \left(\frac{\pi}{i+j}\right)^{3/2} Exp\left[\frac{-ij}{i+j}(RA - RB)^2\right];$

$F[x\_] := \frac{1}{\sqrt{x}} Integrate\left[e^{-y^2}, \{y, 0, \sqrt{x}\}\right] /; x > 0;$

$F[x\_] := 1 /; x <= 0;$

$INE[ZN\_][RN\_][i\_][j\_][RA\_][RB\_] := \left(\frac{4i*j}{\pi^2}\right)^{3/4} \frac{-2\pi}{i+j} ZN Exp\left[\frac{-ij}{i+j}(RA - RB)^2\right]$

$F\left[(i + j)\left(\frac{iRA+jRB}{i+j} - RN\right)^2\right];$

$IEE[i\_][j\_][k\_][l\_][RA\_][RB\_][RC\_][RD\_] := \left(\frac{4i*j}{\pi^2}\right)^{3/4} \left(\frac{4k*l}{\pi^2}\right)^{3/4} \frac{2\pi^{5/2}}{(i+j)(k+l)\sqrt{i+j+k+l}}$

$Exp\left[\frac{-ij}{i+j}(RA - RB)^2 - \frac{kl}{k+l}(RC - RD)^2\right] F\left[\frac{(i+j)(k+l)}{i+j+k+l}\left(\frac{iRA+jRB}{i+j} - \frac{kRC+lRD}{k+l}\right)^2\right];$

Integration

$R = N@INPUTR; EAmp = Electric;$

$ClearAll[F0, Fp, HCore, X0, HS, HT, HVHe, HVH, HElectricr, Hr12, EEn, CC, P, G, MC, S]$

$S[u\_][v\_] := Sum[ccoeff[i]\,ccoeff[j]\ IS[expcoeff[u][i]][expcoeff[v][j]]$

$\left[(-1)^u \frac{R}{2}\right]\left[(-1)^v \frac{R}{2}\right], \{i, 1, 3\}, \{j, 1, 3\}]$

123

$$HS = \begin{pmatrix} S[1][1] & S[1][2] \\ S[2][1] & S[2][2] \end{pmatrix};$$

ClearAll[T]

T[u_][v_]:=Sum[ccoeff[i]ccoeff[j] IK[expcoeff[u][i]][expcoeff[v][j]]

$\left[(-1)^u \frac{R}{2}\right]\left[(-1)^v \frac{R}{2}\right]$, {i, 1, 3}, {j, 1, 3}]

$$HT = \begin{pmatrix} T[1][1] & T[1][2] \\ T[2][1] & T[2][2] \end{pmatrix};$$

ClearAll[VHe]

VHe[u_][v_]:=Sum $\left[$ccoeff[i]ccoeff[j] INE[2] $\left[-\frac{R}{2}\right]$ [expcoeff[u][i]][expcoeff[v][j]]

$\left[(-1)^u \frac{R}{2}\right]\left[(-1)^v \frac{R}{2}\right]$, {i, 1, 3}, {j, 1, 3}]

$$HVHe = \begin{pmatrix} VHe[1][1] & VHe[1][2] \\ VHe[2][1] & VHe[2][2] \end{pmatrix};$$

ClearAll[VH]

VH[u_][v_]:=Sum $\left[$ccoeff[i]ccoeff[j] INE[1] $\left[\frac{R}{2}\right]$ [expcoeff[u][i]][expcoeff[v][j]]

$\left[(-1)^u \frac{R}{2}\right]\left[(-1)^v \frac{R}{2}\right]$, {i, 1, 3}, {j, 1, 3}]

$$HVH = \begin{pmatrix} VH[1][1] & VH[1][2] \\ VH[2][1] & VH[2][2] \end{pmatrix};$$

ClearAll[Electricr]

Electricr[u_][v_]:=EAmpSum[ccoeff[i]ccoeff[j] Ir[expcoeff[u][i]][expcoeff[v][j]]

$\left[(-1)^u \frac{R}{2}\right]\left[(-1)^v \frac{R}{2}\right]$, {i, 1, 3}, {j, 1, 3}]

$$HElectricr = \begin{pmatrix} Electricr[1][1] & Electricr[1][2] \\ Electricr[2][1] & Electricr[2][2] \end{pmatrix};$$

HCore = HT + HVHe + HVH + HElectricr;

ClearAll[r12]

r12[a_][b_][c_][d_]:=Sum[ccoeff[i]ccoeff[j]ccoeff[k]ccoeff[l]

IEE[expcoeff[a][i]][expcoeff[b][j]][expcoeff[c][k]][expcoeff[d][l]]

$\left[(-1)^a \frac{R}{2}\right]\left[(-1)^b \frac{R}{2}\right]\left[(-1)^c \frac{R}{2}\right]\left[(-1)^d \frac{R}{2}\right]$, {i, 1, 3}, {j, 1, 3}, {k, 1, 3}, {l, 1, 3}]

Hr12 = Table[r12[a][b][c][d], {a, 2}, {b, 2}, {c, 2}, {d, 2}];

Interations

F0 = HCore;

$$U = \begin{pmatrix} 2^{-1/2} & 2^{-1/2} \\ 2^{-1/2} & -2^{-1/2} \end{pmatrix};$$

$$X0 = U.\begin{pmatrix} (1 + HS[[1, 2]])^{-1/2} & 0 \\ 0 & (1 - HS[[1, 2]])^{-1/2} \end{pmatrix};$$

124

databuffFF = Table[F0, {i, 100}];

databuffEEn = Table[0, {i, 100}];

function[n_]:=Module[{}, Fp = X0 † .databuffFF[[n]].X0;

$$CC = \begin{pmatrix} \text{Eigensystem[Fp][[2, 1, 1]]} & \text{Eigensystem[Fp][[2, 2, 1]]} \\ \text{Eigensystem[Fp][[2, 1, 2]]} & \text{Eigensystem[Fp][[2, 2, 2]]} \end{pmatrix};$$

MC = X0.CC;

$$P = \begin{pmatrix} 2MC[[1, 1]]^2 & 2MC[[1, 1]]MC[[2, 1]] \\ 2MC[[2, 1]]MC[[1, 1]] & 2MC[[2, 1]]^2 \end{pmatrix};$$

G = {{Sum[P[[i, j]](Hr12[[1, 1, j, i]] − 0.5Hr12[[1, i, j, 1]]), {i, 1, 2}, {j, 1, 2}],

Sum[P[[i, j]](Hr12[[1, 2, j, i]] − 0.5Hr12[[1, i, j, 2]]), {i, 1, 2}, {j, 1, 2}]},

{Sum[P[[i, j]](Hr12[[2, 1, j, i]] − 0.5Hr12[[2, i, j, 1]]), {i, 1, 2}, {j, 1, 2}],

Sum[P[[i, j]](Hr12[[2, 2, j, i]] − 0.5Hr12[[2, i, j, 2]]), {i, 1, 2}, {j, 1, 2}]}};

FF = HCore + G;

EEn = ½Sum[P[[j, i]](HCore[[i, j]] + FF[[i, j]]), {i, 1, 2}, {j, 1, 2}];

databuffFF[[n + 1]] = FF;

databuffEEn[[n]] = EEn]

n = 1;

While[True, If[Abs[function[n] − function[n + 1]] < 0.00001, Break[]];

n++]

Hartree - Fock & CI & UCC Algebra Curve

SignList = {−1, −1, −1, 1, 1, 1};

ORTHONORMEXPC = {e11p, e21p, e31p, e12p, e22p, e32p};

SQHmatrix[dp_]:=Module[{},

M11 = OUTPUT[[dp, 16]] † [[1, 1]]; M12 = OUTPUT[[dp, 16]] † [[1, 2]];

M21 = OUTPUT[[dp, 16]] † [[2, 1]]; M22 = OUTPUT[[dp, 16]] † [[2, 2]];

ORTHONORMC = {{M11c1, M11c2, M11c3, M12c1, M12c2, M12c3},

{M21c1, M21c2, M21c3, M22c1, M22c2, M22c3}};

R = $\frac{dp}{10}$;

IKList = Table[IK[ORTHONORMEXPC[[i]]][ORTHONORMEXPC[[j]]]

[SignList[[i]]$\frac{R}{2}$] [SignList[[j]]$\frac{R}{2}$], {i, 6}, {j, 6}] ;

INEList1 = Table [INE[2] [$−\frac{R}{2}$] [ORTHONORMEXPC[[i]]][ORTHONORMEXPC[[j]]]

[SignList[[i]]$\frac{R}{2}$] [SignList[[j]]$\frac{R}{2}$], {i, 6}, {j, 6}] ;

INEList2 = Table [INE[1] [$\frac{R}{2}$] [ORTHONORMEXPC[[i]]][ORTHONORMEXPC[[j]]]

```
[SignList[[i]]R/2] [SignList[[j]]R/2], {i, 6}, {j, 6}];
IEEList = Table[IEE[ORTHONORMEXPC[[i]]][ORTHONORMEXPC[[j]]]
[ORTHONORMEXPC[[k]]][ORTHONORMEXPC[[l]]]
[SignList[[i]]R/2] [SignList[[j]]R/2] [SignList[[k]]R/2] [SignList[[l]]R/2],
{i, 6}, {j, 6}, {k, 6}, {l, 6}];
hpq = Table[Sum[ORTHONORMC[[u, i]]ORTHONORMC[[v, j]](IKList[[i, j]]
+INEList1[[i, j]] + INEList2[[i, j]]), {i, 1, 6}, {j, 1, 6}], {u, 2}, {v, 2}];
hpqrs = Table[Sum[ORTHONORMC[[u, i]]ORTHONORMC[[v, j]]
ORTHONORMC[[m, k]]ORTHONORMC[[n, l]]IEEList[[i, j, k, l]],
{i, 1, 6}, {j, 1, 6}, {k, 1, 6}, {l, 1, 6}], {u, 2}, {v, 2}, {m, 2}, {n, 2}];
SQH = Table[0, {4}, {4}];
SQH[[1, 1]] = 2hpq[[1, 1]] + hpqrs[[1, 1, 1, 1]];
SQH[[1, 2]] = −hpq[[1, 2]] − 1/2(hpqrs[[1, 2, 1, 1]] + hpqrs[[1, 1, 1, 2]]);
SQH[[1, 3]] = hpq[[1, 2]] + 1/2(hpqrs[[1, 2, 1, 1]] + hpqrs[[1, 1, 1, 2]]);
SQH[[1, 4]] = hpqrs[[1, 2, 1, 2]];
SQH[[2, 1]] = SQH[[1, 2]];
SQH[[2, 2]] = hpq[[1, 1]] + hpq[[2, 2]] + 1/2(hpqrs[[1, 1, 2, 2]] + hpqrs[[2, 2, 1, 1]]);
SQH[[2, 3]] = −1/2(hpqrs[[1, 2, 2, 1]] + hpqrs[[2, 1, 1, 2]]);
SQH[[2, 4]] = −hpq[[1, 2]] − 1/2(hpqrs[[1, 2, 2, 2]] + hpqrs[[2, 2, 1, 2]]);
SQH[[3, 1]] = SQH[[1, 3]];
SQH[[3, 2]] = SQH[[2, 3]];
SQH[[3, 3]] = hpq[[1, 1]] + hpq[[2, 2]] + 1/2(hpqrs[[1, 1, 2, 2]] + hpqrs[[2, 2, 1, 1]]);
SQH[[3, 4]] = hpq[[1, 2]] + 1/2(hpqrs[[1, 2, 2, 2]] + hpqrs[[2, 2, 1, 2]]);
SQH[[4, 1]] = SQH[[1, 4]];
SQH[[4, 2]] = SQH[[2, 4]];
SQH[[4, 3]] = SQH[[3, 4]];
SQH[[4, 4]] = 2hpq[[2, 2]] + hpqrs[[2, 2, 2, 2]];
SQH
];
```

个人简历、在学期间发表的学术论文与研究成果

个人简历

1990 年 02 月 21 日出生于安徽省安庆市。

2008 年 9 月考入武汉理工大学大学理学院电子信息科学与技术专业，2012 年 7 月本科毕业并获得理学学士学位。

2012 年 9 月免试进入清华大学交叉信息研究院攻读物理学学位至今。

发表的学术论文

[1] **Shen Y**, Lu Y, Zhang K, et al. Quantum optical emulation of molecular vibronic spectroscopy using a trapped-ion device[J]. Chemical Science, 2018, 9: 836–840.

[2] **Shen Y**, Zhang X, Zhang S, et al. Quantum implementation of the unitary coupled cluster for simulating molecular electronic structure[J]. Physical Review A, 2017, 95(2): 020501.

[3] Zhang X, Zhang K, Shen Y, et al. Experimental quantum simulation of fermion-antifermion scattering via boson exchange in a trapped ion[J]. Nature communications, 2018, 9(1): 195.

[4] Park J, Lu Y, Lee J, et al. Revealing nonclassicality beyond Gaussian states via a single marginal distribution[J]. Proceedings of the National Academy of Sciences, 2017, 114(5): 891-896.

[5] Zhang X, Shen Y, Zhang J, et al. Time reversal and charge conjugation in an embedding quantum simulator[J]. Nature communications, 2015, 6: 7917. MLA

[6] Um M, Zhang X, Zhang J, et al. Experimental certification of random numbers via quantum contextuality[J]. Scientific reports, 2013, 3: 1627.